Institut für Wasserbau · Universität Stuttgart

Mitteilungen

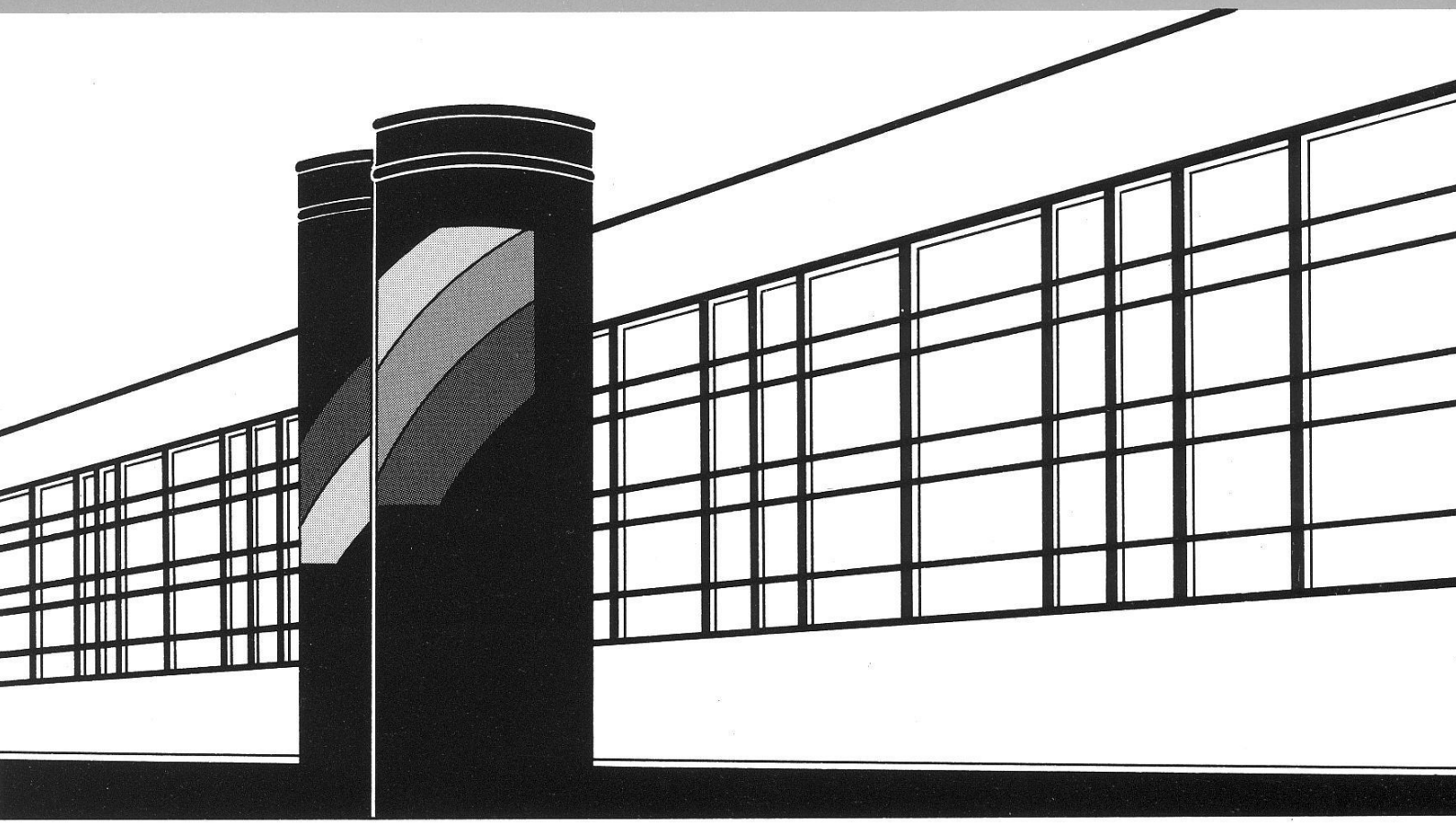

Heft 186 Miloš Vasin

Influence of the soil structure and property contrast on flow and transport in the unsaturated zone

Influence of the soil structure and property contrast on flow and transport in the unsaturated zone

Von der Fakultät Bau- und Umweltingenieurwissenschaften der Universität Stuttgart zur Erlangung der Würde eines Doktor-Ingenieurs (Dr.-Ing.) genehmigte Abhandlung

Vorgelegt von

Miloš Vasin

aus Novi Sad (Serbien)

Hauptberichter:	Prof. Dr. rer. nat. Insa Neuweiler
Mitberichter:	Prof. Dr.-Ing. Rainer Helmig
	Prof. Dr. sc. nat. Kurt Roth

Tag der mündlichen Prüfung: 11. Dezember 2009

Institut für Wasserbau der Universität Stuttgart

2010

Heft 186

Influence of the soil structure and property contrast on flow and transport in the unsaturated zone

von
Dr.-Ing.
Miloš Vasin

Eigenverlag des Instituts für Wasserbau der Universität Stuttgart

D93 Influence of the soil structure and property contrast on flow and transport in the unsaturated zone

Bibliografische Information der Deutschen Nationalbibliothek
Die Deutsche Nationalbibliothek verzeichnet diese Publikation in der Deutschen Nationalbibliografie; detaillierte bibliografische Daten sind im Internet über http://www.d-nb.de abrufbar.

Vasin, Milos:
Influence of the soil structure and property contrast on flow and transport in the unsaturated zone / von Milos Vasin. Institut für Wasserbau, Universität Stuttgart. - Stuttgart: Inst. für Wasserbau, 2010

(Mitteilungen / Institut für Wasserbau, Universität Stuttgart: H. 186)
Zugl.: Stuttgart, Univ., Diss., 2010
ISBN 978-3-933761-90-3
NE: Institut für Wasserbau <Stuttgart>: Mitteilungen

Herausgegeben 2010 vom Eigenverlag des Instituts für Wasserbau
Druck: Document Center S. Kästl, Ostfildern

… mom Stevanu i mojoj Sandri

Acknowledgements

I would like to thank my supervisor Prof. Dr. rer. nat. Insa Neuweiler, whose expertise, guidance, and patience contributed considerably to my academic experience. She provided me with great exposure to the field of upscaling of flow and transport in the subsurface and related problems, always providing direction and technical support. Our numerous discussions resulted in valuable advice that was essential for my work. In addition, I sincerely thank Prof. Dr.-Ing. Rainer Helmig for his helpful and encouraging suggestions during my whole work. Also, I would like to thank Prof. Dr. sc. nat. Kurt Roth. Our few, but substantial, discussions regarding experiments and experimental data analysis, were invaluable for the parameter fitting of materials used in performed experiments.

I would like to thank my colleagues from the Institute of Hydraulic Engineering, Stuttgart for a wonderful working environment. In particular, I am grateful to "Verfuegungsgebaeude" Team: Li Yang, Veronica Heiss, Anna Kuhlmann and Wolfgang Nowak for a great time spent there. However, I would also like to thank all other members of LH2, of whom especially: Melanie and Onur Dogan for their help with MUFTE-UG as well as Frau Lawday for her kindness and assistance with many administrative issues. I would also like to mention Peter Lehmann as a great support during experiments performed at PSI.

I am also grateful to my friends in Stuttgart for making my time here pleasurable: Zoća, Drale, Čiča, Tihi, Cjestmir, Jeff and family Trifković. Appreciation also goes to my friends from Novi Sad: kum Nidzus, kuma Sofija, Zjala, Mime, Jankela, Cudni, Dovla, Rada, but also to my best man Loni and his wife Mira. Also, I would like to mention Isak and Todor as the youngest members of our team. Many thanks also go to my Belgrade friends: Ivan, Puta, Zile, Mirko, Škoro, Bogi and Far for their long-distance support.

Finally, I would like to express my gratitude to my family, who gave me tremendous support: my sister Vukica for everlasting understanding, encouragement and great source of laugh and good mood in our family and also to my cousin Brane. I am extraordinary thankful to my parents (Julka and Stevan) for their everlasting devotion and generous support during my carrier. Especially, I would like to thank my wife Sandra and son Stevan for their love and encouragement during this endeavor. Their encouragement gave me the strength to persist and motivation to never give up.

This work was done within the International Doctoral Program Environment Water (ENWAT). Financial support was provided by scholarship IPSWaT funded by BMBF. They are all greatly acknowledged.

Contents

List of Figures

List of Tables

Notation

Symbol	Definition	Dimension
A	cross sectional area	$[\mathrm{L}^2]$
c	solute concentration	$[\mathrm{M\,L}^{-3}]$
C	typical value of the inverse capacity	$[\mathrm{L}]$
d	length that the neutron beam passes through	$[\mathrm{L}]$
d_{water}	total thicknesses of water in the column at partly saturated conditions	$[\mathrm{L}]$
$d_{\mathrm{water\,sat}}$	total thicknesses of water in the column at saturated conditions	$[\mathrm{L}]$
D	dispersion tensor	$[\mathrm{L}^2\,\mathrm{T}^{-1}]$
D_{eff}	effective dispersion tensor	$[\mathrm{L}^2\,\mathrm{T}^{-1}]$
$EMAX_{\mathrm{h}}$	morphological operator	[-]
$\vec{e_z}$	unit vector in z direction	[-]
g	gravitational acceleration	$[\mathrm{L\,T}^{-2}]$
H	characteristic capillary pressure head	$[\mathrm{L}]$
h_{c}	capillary head	$[\mathrm{L}]$
h_{d}	air entry pressure head	$[\mathrm{L}]$
$h_{\mathrm{e,\,fine}}$	apparent entry pressure of fine sand	$[\mathrm{L}]$
$\tilde{H}_{\mathrm{k}}$	matrix of derivatives	$[\mathrm{M}$ or $\mathrm{M\,T\,L}^{-1}]$
h_{tot}	total potential express in terms of water height	$[\mathrm{L}]$
I	intensity of the neutron beam after passing through the matter	[-]
I_{dry}	neutron intensities after passing through the dry column	[-]
I_{sat}	neutron intensities after passing through the saturated column	[-]
I_0	intensity of the neutron beam before passing through the matter	[-]
I_1	neutron intensities after passing through partly saturated column	[-]
K	hydraulic conductivity	$[\mathrm{L\,T}^{-1}]$
K_{eff}	upscaled effective conductivity	$[\mathrm{L\,T}^{-1}]$

Symbol	Definition	Dimension
K_{g}	geometric mean of saturated hydraulic conductivity	$[\mathrm{L\,T^{-1}}]$
k_{r}	relative permeability	[-]
K_{rw}	relative conductivity	$[\mathrm{L\,T^{-1}}]$
K_{u}	unsaturated hydraulic conductivity tensor	$[\mathrm{L\,T^{-1}}]$
ℓ	typical microscopic length scale	[L]
L	typical macroscopic length scale	[L]
n	degree of freedom	[-]
n_{g}	unknown vector of parameters	[-]
O_{mod}	simulated outflow	[L]
O_{meas}	measured outflow	[L]
p	pressure	$[\mathrm{M\,T^{-2}\,L^{-1}}]$
P	probability	[%]
p_{a}	air pressure	$[\mathrm{M\,T^{-2}\,L^{-1}}]$
p_{c}	capillary pressure	$[\mathrm{M\,T^{-2}\,L^{-1}}]$
p_{h}	hydrostatic pressure	$[\mathrm{M\,T^{-2}\,L^{-1}}]$
p_{o}	osmotic pressure	$[\mathrm{M\,T^{-2}\,L^{-1}}]$
r	mass source/sink rate	$[\mathrm{M\,L^{-3}\,T}]$
S	saturation	[-]
S_{e}	effective saturation	[-]
S_{rw}	residual saturation	[-]
t	time	[T]
T	characteristic time scale	[T]
U	characteristic velocity	$[\mathrm{L\,T^{-1}}]$
q	specific discharge or Darcy's velocity	$[\mathrm{L\,T^{-1}}]$
Q	discharge	$[\mathrm{L^3\,T^{-1}}]$
v	seepage velocity	$[\mathrm{L\,T^{-1}}]$
v_{eff}	effective velocity	$[\mathrm{L\,T^{-1}}]$
W	weighting matrix	[-]
y	vector of measurements	[M]
z	geodetic hight	[L]
α	material-specific attenuation coefficient	$[\mathrm{L^{-1}}]$
α_{water}	calibrated attenuation coefficient of heavy water	$[\mathrm{L^{-1}}]$
ε	ration between typical microscopic and macroscopical length scale	[-]
χ^2	objective function	[-]
λ	Brooks-Corey parameter	[-]
λ_1	Brooks-Corey parameter for the $h_{\mathrm{c}} - S$ relationship	[-]

Symbol	Definition	Dimension
λ_2	Brooks-Corey parameter for the $K_\mathrm{u} - S$ relationship	[-]
ϕ	porosity of the medium	[-]
Φ	volume percentages of the material	[%]
σ_bc	standard deviation due to uncertainties in fixing the pressure boundary condition	[L]
σ_dev	standard deviation of mass measured with the balance	[M]
σ_h	measurement error for the head of the boundary condition	[L]
σ_s	error of tomography saturation measurements	[-]
σ_obs	standard deviation due to uncertainties in the time of measurement	[T]
τ	typical time scale on small length scale	[T]
$\bar{\Theta}$	characteristic water content	[-]
$\bar{\Theta}_\mathrm{back}$	characteristic water content in background	[-]
Θ_eff	upscaled effective water content	[-]
$\bar{\Theta}_\mathrm{incl}$	characteristic water content in inclusions	[-]
Θ_w	volumetric water content	[-]
ρ	density	$[\mathrm{M\,L^{-3}}]$

Abstract

The unsaturated zone represents a transition zone for contaminants spilled on the ground surface, which by reaching an underlying aquifer cause groundwater pollution. The complexity of processes occurring in the unsaturated zone as well as highly heterogeneous structures, which are never known in detail are the main reasons why it is very challenging to make predictions of processes under unsaturated conditions. Instead of resolving the exact distribution of heterogeneities, which would cause enormous computational and field effort, flow and transport in the unsaturated zone are very often modeled in an average sense, where the input parameters of the model are spatially averaged (effective parameters). Derivation of those simplified models is called upscaling.

In this study, modeling of flow and transport in the unsaturated zone, when upscaled models are used has been investigated. Particularly, this study focuses on upscaled models for flow and transport in the unsaturated zone derived by means of homogenization theory.

Those two derived models can not be used in general since they are derived under certain assumptions, which are necessary when homogenization is used. Therefore, many questions rise, when those models are used considering their limitations and constrains. One of the major assumption of upscaled models derived by means of homogenization is domain periodicity. In this case the effective parameters could be derived explicitly as the structure is known in detail. However, in nature the structure of domain is usually unknown and effective parameters have to be estimated. The derived upscaled models could be only considered as reliable and efficient when the effective parameters are estimated in an adequate and effective way, capturing the influence of heterogeneities on the smaller scale. Additional to the periodicity and difficulty with estimation of effective parameters, mentioned models could be derived either for equilibrium or non-equilibrium conditions, dependent from the parameter contrasts (small or large) between materials. However, in order to distinguish if equilibrium or non-equilibrium model is more suitable for modeling of flow and transport processes, typical time scales have to be estimated.

In order to investigate above mentioned challenges with regard to effective parameter estimation, assumption of upscaled models and time scale analysis, three lab experiments have been performed. The experimental data have been

compared with numerical simulations or analytical solutions. The experiments done here have been performed under well controlled conditions with artificial heterogeneous structures. As a result, the conclusions of the experiments are specific for these typical conditions.

The first part of this study has been focused on flow in the unsaturated zone under equilibrium conditions, meaning that the upscaled model has been derived using a small soil parameter contrast. Different structures, with significantly different connectivity (periodic and random structure) have been investigated in order to gain a better knowledge of the structural influence on the estimation of effective parameters. Additionally, the applicability of the mentioned upscaled flow model under ideal and non-ideal conditions has been assessed such that the domain does not fulfil the assumption of periodicity, but also of small parameter contrasts needed in the case of equilibrium model. It has been shown that the estimated parameters used in the upscaled 1D model performed well. Estimated parameters based on only rather limited information were sufficient to predict the drainage process very well.

The flow in the unsaturated zone under non-equilibrium has been investigated in the second part of the study. This implies that the parameter contrast between soil materials used in the experimental study was large. Different options for estimation of typical time scales have been presented and discusses as they are decisive in order to chose, which upscaled model (equilibrium or non-equilibrium) is more appropriate to be used. The obtained time estimates have been further compared with the experimental and numerical findings. It has been shown that the water capacity was the crucial parameter in order to make good drainage time predictions in this experiment. The system in this example has reacted with the fastest predicted time scale.

During the third part of this research, solute transport under equilibrium and non-equilibrium has been investigated. The goal was to observe if equilibrium or non-equilibrium of solute transport could be predicted by using time scale analysis. The estimated time scales have been compared with experimental results. The equilibrium and non-equilibrium have been obtained during the experiments leading to tailing and retardation of tracer. Both equilibrium and non-equilibrium conditions could be predicted by the time analysis. Model assuming equilibrium would give bad predictions of solute transport in case of experiment, where non-equilibrium occurred.

Zusammenfassung

Die vorliegende Arbeit liefert einen Beitrag zur Erforschung von Strömungs- und Transportprozessen in der ungesättigten Zone unter Einsatz von hochskalierten Modellen (engl. "upscaled model"). Aufgrund der Komplexität der vorherrschenden Prozesse und der Heterogenität des Bodens, die praktisch nie vollständig bekannt ist, ist es äußerst anspruchsvoll, für diesen Bereich des Bodens Voraussagen zu treffen. Die exakte Lösung unter Berücksichtigung der Heterogenität zu berechnen, würde einen enormen Aufwand an Rechnerleistung und eine große Anzahl empirischer Messungen erfordern. Hochskalierte Modelle stellen im Gegensatz dazu einen eleganten Ansatz dar, um gute Vorhersagen für Strömungs- und Transportprozesse zu erhalten.

Die vorliegende Untersuchung legt den Schwerpunkt auf hochskalierte Modelle für Strömungs- und Transportprozesse in der ungesättigten Zone, die mit Hilfe der Homogenisierungstheorie abgeleitet wurden. Da bei der Herleitung bestimmte Annahmen getroffen werden, können diese Modelle nicht generell auf alle realen Konstellationen und Anwendungen bezogen werden. So basieren die beiden hochskalierten Modelle, die in dieser Untersuchung verwendet wurden, insbesondere auf der Annahme der Periodizität des Gebietes, welche eine Kernannahme der Homogenisierungstheorie ist. Die benötigten Parameter können hierbei nur bestimmt werden, wenn die Struktur im Detail bekannt ist. Dies ist in der Realität normalerweise nicht der Fall, weshalb die Parameterwerte geschätzt werden müssen. Die abgeleiteten hochskalierten Modelle können nur dann als verlässlich und effizient gelten, wenn die enthaltenen Parameter adäquat bestimmt werden und insbesondere auch den Einfluss von kleinerskaligen Heterogenitäten erfassen. Die Bestimmung der Parameterwerte ist keineswegs eine triviale Aufgabe. Vielmehr müssen alle verfügbaren Informationen über die Bodenstruktur miteinbezogen werden. Abgesehen von der Schwierigkeit, die effektiven Parameter zu schätzen, und zusätzlich zur Problematik der Periodizitätsannahme, muss man sich außerdem für einen Gleichgewichts- oder Nicht-Gleichgewichtsansatz bei der Modellherleitung entscheiden. Dabei ist zu berücksichtigen, wie sehr sich die Materialparameter unterscheiden. Bei kleinen Differenzen ist ein Gleichgewichts-Modell zu wählen, bei großen Differenzen ein Nicht-Gleichgewichts-Modell. Um diese Entscheidung treffen zu können, ist es notwendig, die typischen Zeitskalen bestimmter Prozesse abzuschätzen.

Um die hochskalierten Strömungs- und Transportmodelle unter Verwendung verschiedener Messtechniken zu analysieren, wurden für diese Arbeit drei Laborexperimente durchgeführt. Die Experimente sind als Beitrag zur Analyse der oben erwähnten Probleme (Parameterschätzung, Annahmen bei der Herleitung hochskalierter Modelle und Bestimmung der Zeitskalen) konzipiert worden. Die Messergebnisse wurden außerdem mit analytischen Lösungen oder numerischen Simulationen verglichen. Die im Folgenden dargelegten experimentellen Ergebnisse dürfen indessen nicht vorschnell verallgemeinert werden, da die Experimente in einer kontrollierten Laborumgebung durchgeführt wurden und auf künstlich hergestellter Heterogenität beruhten. Des Weiteren muss auch auf die immer noch große Lücke zwischen Theorie und Experiment im Bereich des "upscaling" verwiesen werden. Die vorliegende Arbeit möge dazu beitragen, diese Lücke ein Stück zu schließen.

In dieser Arbeit werden drei grundlegende Fragen bearbeitet, welche folgendermaßen zusammengefasst werden können:

- **Frage 1:** Wie kann der Einfluss der Bodenstruktur auf die effektiven Parameter, welche für die hochskalierten Modelle für Strömungsprozesse in der ungesättigten Zone verwendet werden, charakterisiert und quantifiziert werden?

- **Frage 2:** Inwiefern sind solche Modelle in der Lage Voraussagen über Strömungs- und Transportprozesse in der ungesättigten Zone zu treffen, wenn die Annahmen zur Herleitung der hochskalierten Modelle nicht vollständig erfüllt sind?

- **Frage 3:** Inwiefern können aus der Zeitskalenanalyse verlässliche Kriterien für die Wahl zwischen Gleichgewichts- und Nicht-Gleichgewichts-Modellen hergeleitet werden?

Der erste Teil dieser Studie geht auf die Strömungsprozesse in der ungesättigten Zone unter Gleichgewichtsbedingungen ein. Das hochskalierte Strömungsmodell wurde unter der Annahme kleiner Parameterunterschiede hergeleitet, was dazu führt, dass die Gleichgewichtsbedingungen im Gebiet erfüllt sind. Verschiedene Strukturen, die sich deutlich in ihrer Konnektivität unterscheiden (periodisch und zufällig) wurden auf die Frage hin untersucht, welchen Einfluss Struktur auf die effektiven Parameter hat, wenn diese nur aus der Kenntnis der Volumenanteile der verwendeten Materialien abgeschätzt wurden. Weiterhin wurde die Anwendbarkeit des Modells unter idealen und nicht-idealen Bedingungen untersucht, d.h. es wurde untersucht, welche Auswirkungen es hat, wenn von der Annahme der Periodizität und der kleinen Parameterdifferenz abgewichen wird. Der zweite Teil der Studie befasst sich mit der Strömung in der ungesättigten Zone unter Nicht-Gleichgewichtsbedingungen. In diesem Fall sind die Parameterunterschiede der

Bodenmaterialien groß. Um entscheiden zu können, welche Modellvariante (Gleichgewicht vs. Nicht-Gleichgewicht) geeigneter ist, müssen typische Zeitskalen bestimmt werden. In diesem Teil der Arbeit werden verschiedene Optionen zur Schätzung der Zeitskalen zu illustriert. Die Ergebnisse der Schätzung werden mit experimentellen und numerischen Resultaten verglichen.

Der dritte Teil untersucht den Partikeltransport im Gleichgewicht und im Nicht-Gleichgewicht. Ziel war es, zu untersuchen, ob aufgrund des Vergleichs beobachteter typischer Zeitskalen, Voraussagen für Gleichgewichts - bzw. Nicht-Gleichgewichtszustände möglich sind.

0.1 Einfluss von Struktur auf die Schätzung effektiver Parameter und Bewertung der Annahmen bei der Modellierung von Strömungsprozessen unter Gleichgewichtsbedingungen (Frage 1 und 2)

In dieser Forschungsarbeit werden Vorhersagen über die Strömungsvorgänge in der ungesättigten Zone, welche mit Hilfe von hochskalierten Modellen gemacht wurden, verglichen. Dazu wurden Experimente an künstlich aufgebauten, heterogenen, Sandsäulen durchgeführt. Die beiden bei diesen Experimenten benutzten Sandsäulen hatten dieselben räumlichen Dimensionen und wurden mit den gleichen Volumenanteilen der beiden verwendeten Sandmaterialen befüllt. Der entscheidende Unterschied war, dass die eine Sandsäule eine reguläre periodische Struktur und damit ein wohldefiniertes makroskopisches Elementarvolumen aufwies. Da hierbei das Hintergrundmaterial klar von den Einschlüssen getrennt war, wurde der Maxwell-Ansatz für die Schätzung der hydraulischen Leitfähigkeit herangezogen. Die andere Säule kann als das Gegenteil betrachtet werden. Es gab kein makroskopisch repräsentatives Elementarvolumen und sowohl für den feinen als auch für den groben Sand existierten verbundene Pfade durch die gesamte Säule. Für diesen Fall wurde ein selbstkonsistenter Ansatz herangezogen, um die hydraulische Leitfähikeit zu schätzen.

Während des Drainageprozesses wurde in der periodischen Säule Wasser im Inklusionsmaterial eingeschlossen. Die geltenden effektiven Parameterwerte wurden mit Hilfe der kalibrierten Parameter gemäß Tabelle 3.3 geschätzt. Das hochskalierte 1D-Modell unter Verwendung der geschätzten Parameter lieferte gute Prädiktionen für die periodisch struktuierte Säule, und zwar sowohl für das stationäre Verhalten in der Säule, als auch für die Zeitabhängigkeit des Ausflusses (vgl. Abbildung 3.22). Der Vergleich des zeitlichen Verlaufs der gemittelten Sättigungen der vier waagrechten Schichten von Einheitszellen zeigte eine

gute Übereinstimmung (vgl. Abbildung 3.25). Links in Abbildung 3.25 sieht man die vierte Druckstufe (auf -40 cm). In diesem Fall wird die Zeitabhängigkeit der Wassergehaltsabnahme vom hochskalierten 1D-Modell überschätzt. Dies war zu erwarten, da eine horizontale Tangente an die effektive Retentionskurve (Abbildung 3.15) eingeführt wurde, um das Einschliessen von Wasser zu erfassen. Diese Konstruktion einer effektiven Retentionsfunktion kann lediglich auf die stationäre Lösung für die gesamte Wassermasse in der Säule bezogen werden, nicht jedoch auf die Zeitabhängigkeit des Ausflusses.

Obwohl die periodische Struktur so gestaltet war, dass die Annahmen des hochskalierten Modells soweit wie möglich erfüllt werden, wird das Kriterium der Separation der Längenskalen durch die Säule kaum erfüllt. Das Verhältnis der beiden Längenskalen beträgt $\varepsilon = \ell/L = 0.25$ und ist damit nicht wesentlich kleiner als eins. Trotz dieser Diskrepanz zu den Anforderungen wich das hochskalierte 1D-Modell unter Verwendung der homogenisierten Parameter nicht sehr von den Messungen ab. Auch gab es keine signifikanten Unterschiede in den Ausflusskurven. Dies deutet darauf hin, dass die wenigen Angaben, welche in den Maxwell-Ansatz eingingen, ausreichten, um den in den Experimenten untersuchten Drainageprozess zu beschreiben.

Auch für die zufällig strukturierte Säule wurden - wie für die periodische angeordnete Säule - die Prädiktionen des hochskalierten Modells mit der experimentell ermittelten Retentionsfunktion und der experimentell ermittelten Ausflusskurve verglichen. Es wurde das gleiche Modell verwendet wie für den periodischen Fall. Die Modellvoraussagen erwiesen sich als sehr gut (vgl. Abbildung 3.21). Dies gilt auch für den in der Säule lokal gemittelten Wassergehalt (vgl. 3.26). Da die zufällige Säule keine natürlich definierten Elementarzellen aufweist, wurde für den Vergleich des gemittelten Wassergehalts das gleiche Teilvolumen wie für die periodische Struktur herangezogen. Obwohl im Falle der zufällig angeordneten Struktur die Annahme separierter Skalen, auf der die Herleitung des hochskalierten Modells basiert, offensichtlich verletzt ist, ergaben sich mit diesem 1D-Modell gute Vorhersagen. Offensichtlich gilt für die hier dargestellten Experimente, dass die Verletzung der Annahmen die Struktur betreffend, keine Einschränkung für die Anwendbarkeit des hochskalierten Modells darstellt.

Das **Retentionsverhalten** der Säulen wird aufgrund des Einschlusses von Wasser von der Struktur beeinflusst (im Fall der periodischen Struktur). Wasser wurde von den groben Zellen zurückgehalten, weil die Luft diese Zellen nicht durch das vollständig durchnässte feine Material erreichen konnte. Wenn der Fluss durch die Säulen mit Hilfe der Richards-Gleichung modelliert wird, kann dieser Einschlusseffekt für die periodisch strukturierte Säule nicht direkt erfasst werden. Dadurch, dass dem groben Material ein Eindringdruck zugewiesen wurde, konnte das Einschließen von Wasser in der vorliegenden Arbeit für die periodische Säule berücksichtigt werden (vgl. Sektion 3 und Abbildung 3.15). Dabei wird in diesem Modell der Lufteintritt mit einer waagrechten Linie in der $h_c - S$-Kurve

vereinfacht erfasst. Um bei praktischen Anwendungen derartige Auswirkungen des Eindringdrucks vorhersagen zu können, muss bekannt sein, dass grober Sand in feinen Sand eingebettet ist. Ohne diese Information und die daraus resultierenden Änderungen, wäre die Annahme, man könne das hochskalierte 1D-Modell für die periodische Struktur nutzen, verfehlt. Ein Modell, das auf diese Modifikation nicht einginge, würde zu schlechten Voraussagen führen (in vorliegenden periodischen Fall etwa zur Prädiktion von fünf Ausfluss-Ereignissen anstelle von drei).

Aus der beschriebenen Arbeit an den beiden Säulen mit periodischer und zufälliger Struktur lässt sich zusammengefasst Folgendes schließen:

- Obwohl einige Voraussetzungen des upscaling-Verfahrens klar verletzt waren (wie in der zufällig angeordneten Säule), erwiesen sich die von dem hochskalierten Modell gemachten Voraussagen für den gemittelten Wassergehalt als gut. Die Empirie erwies sich hier als "nachsichtiger" als man hätte erwarten können.

- Einschlüsse von gröberem Material beeinflussen das Retentionsverhalten der Säulen deutlich. Wenn die Existenz solcher Inklusionen bekannt ist, wird man dieses Wissen nutzen können, um die Parameter des hochskalierten Modells genauer zu bestimmen.

- Sowohl die geschätzten als auch die homogenisierten Parameter des hochskalierten Modells führten zu guten Ergebnissen unter den in der vorliegenden Untersuchung geschaffenen Rahmenbedingungen. Die Parameter, für deren Schätzung nur begrenzte Information zur Verfügung stand, erwiesen sich offensichtlich als ausreichend. Der Drainageprozess konnte überraschend gut erfasst werden. Diese Schlussfolgerung sollte jedoch nicht verallgemeinert werden.

- Für trockenere Bereiche, wo größere Parameterunterschiede auftreten, erhielt man nur dürftige Voraussagen.

0.2 Analyse der Zeitskalen für Strömungsprozesse unter Nicht-Gleichgewichtsbedingungen und Untersuchung der Bedeutung von Grenzflächen während der Drainage

Im zweiten Teil der Studie wurden Strömungsprozesse in der ungesättigten Zone unter Nicht-Gleichgewichtsbedingungen untersucht, welche durch hohe Parameterunterschiede hervorgerufen wurden. Mittels eines Drainageexperiments wird hierbei eine Anordnung untersucht, die sich aufgrund eines makroskopischen

Einschlusseffektes nicht im Gleichgewicht befindet (Experiment II). Dieser Einschlusseffekt entsteht infolge der verringerten Durchlässigkeit des Umgebungsmaterials. Gemessen wurden der Ausfluss und die 3-dimensionale Verteilung des Wassers in der Sandsäule während des Durchflussprozesses. Letzteres erfolgte unter Nutzung der Neutronen-Tomografie. In den Säulen wurden die gleichen Sande eingesetzt wie im obigen, unter 1.1. geschilderten Experiment (Experiment I). Vor der Durchführung des Experiments, das die oben genannten Effekte aufzeigen sollte, wurde versucht, mit Hilfe einer Zeitskalenanalyse, die Zeitdauer für die Drainage zweier Sandinklusionen zu schätzen. Dies spielt bei der Modellierung des Wasserflusses in der ungesättigten Zone auf größeren Skalen, wo Nicht-Gleichgewichtsmodelle geeigneter sein dürften als Gleichgewichts-Modelle, eine grosse Rolle. Ob die Voraussetzung für die Anwendung von Nicht-Gleichgewichtsmodellen gegeben ist, kann mithilfe typischer Zeitskalen für die auftretenden Strömungsprozesse abgeschätzt werden.

In dieser Arbeit wurden die typischen Zeitskalen für den Einschluss von Wasser mithilfe unterschiedlicher Näherungensverfahren geschätzt, wobei für die Eigenschaften der Sande vorher bestimmte Parameter (siehe Tabelle 3.4) verwendet wurden. In diesem Fall wurde aus den geschätzten Zeitskalen gefolgert, dass das Wasser in den Inklusionenen aufgrund der verringerten Durchlässigkeit des Umgebungsmaterials verzögert abfließt.

Die Drainage der Säule erfolgte in zwei Schritten. Zuerst wurde ein Druck von -12 cm auf -32.5 cm angelegt, in einem zweiten Schritt wurde der Unterdruck von -32.5 cm auf -45 cm erhöht, jeweils bezogen auf den Säulenboden. Am Ende der ersten Drainagestufe wurde das umgebende grobe Material fast bis zur Restsättigung entleert. So verhinderte es die Drainage der feinen, nassen Einschlüsse während der zweiten Stufe, obwohl der Eindringdruck des feinen Materials überschritten wurde.

In den Drainageexperimenten wurde beobachtet, dass die Einschlüsse während der ganzen Beobachtungszeit nass blieben. Dies stimmt mit den Vorhersagen der Zeitskalen, die basierend auf den vorher bestimmten Parameter gemacht worden waren, überein. Allerdings wiesen die Würfel aus feinem Sand während der zweiten Druckstufe eindeutig Grenzflächenphänomene auf. Die Grenzflächen der Sandeinschlüsse entleerten sich in einer zeitlichen Größenordnung von einer Stunde. Im Gegensatz dazu, konnte das Leerlaufen im Innern des Sandeinschlusses aufgrund der begrenzten Zeit am PSI nicht über einen ausreichend langen Zeitraum beobachtet werden, um auf die typischen Zeitskalen zu schließen. Die Experimente zeigten deutlich, dass Sandeinschlüsse und Grenzflächen bei der Schätzung der typischen Zeitskalen für den Einschluss von Wasser als separate Materialien betrachtet werden müssen.

Die für die oberen und unteren Einschlüsse erwarteten Drainagezeiten wurden aufgrund der langen Beobachtungszeit mit numerischen Simulationen verglichen. Der Vergleich der erwarteten und simulierten Drainagezeiten, die mittels vorher

bestimmter Parameter ermittelt wurden, ergab eine vernünftige Übereinstimmung (Tabelle 3.4). Es war allerdings notwendig, die Grenzflächen als eigenständiges Material zu behandeln, um die Drainage der Säule erfassen zu können. Am Schluss dieses Teils der Studie wurde weiterhin gezeigt, dass die Grenzflächen in der zeitlichen Analyse berücksichtigt werden müssen, wenn man die Drainagezeiten korrekt berechnen möchte. Die Grenzflächen verlangsamen die Drainage der oberen Inklusion, da die reduzierte Durchlässigkeit dort eine Barriere schafft.

Die Zeitskalenanalyse wies darauf hin, dass die Kapazität der entscheidende Parameter für eine präzise Vorhersage der Drainagezeitskalen bei diesem System ist. Die Leitfähigkeit des Umgebungsmaterials variierte wenig zwischen dem Ende der ersten und der zweiten Druckstufe, da vor dem zweiten Druckabfall die Sättigung bereits nahe ihrem Residualwert lag. Wenn man für die Kapazität am Ende der zweiten Druckstufe Piezometerhöhen wählt, kann man zu guten Vorhersagen der Drainagezeitskalen für das Gesamtsystem (sowohl für untere und obere Inklusionen als auch für die Grenzflächen) gelangen. Das System reagierte immer gemäß der kleinsten der geschätzten Zeitskalen.

Grundsätzlich lässt sich Folgendes festhalten:

- Wie von der zeitlichen Analyse vorhergesagt, haben große Unterschiede in der Leitfähigkeit von grobem und feinem Material zu Nicht-Gleichgewichtsbedingungen geführt. Bestätigt wurde dies durch das Drainage-Experiment II, bei dem Wasser in Inklusionen aus feinem Sand eingeschlossen wurde. Verantwortlich war hierfür die geringere Durchlässigkeit des umgebenden groben Sandes.

- Bei diesem Beispiel stellte sich die Kapazität als der für gute Vorhersagen entscheidende Parameter heraus. Die Leitfähigkeit des umgebenden Sandes zeigte keine signifikanten Änderungen, nachdem die zweite Drainage-Stufe angelegt wurde.

- Das betrachtete System reagierte gemäß der kleinsten vorhergesagten Zeitskala.

- Grenzflächen müssen als eigenständiges Material behandelt werden und in der zeitlichen Analyse berücksichtigt werden. Da trockene Barrieren entstehen, verlangsamen die Grenzflächen die Drainage der Einschlüsse.

0.3 Vorhersage von Gleichgewichts- und Nicht-Gleichgewichtsbedingungen für den Transport gelöster Stoffe (Question 3)

In dieser Arbeit wurde ebenso der Transport von gelösten Stoffen in der ungesättigten Zone unter Nicht-Gleichgewichtsbedingungen analysiert. Denn Nicht-Gleichgewichtsbedingungen werden von großen Parameterunterschieden hervorgerufen und sind bei der Modellierung von Strömungsprozessen in der ungesättigten Zone zu berücksichtigen. Als Kriterium für das Vorliegen von Nicht-Gleichgewichtsbedinungen wurde die Zeitskala T für Prozesse auf der großen Längenskala (Hintergrundmaterial) mit der Zeitskala τ für Prozesse auf der kleinen Längenskala, welche von den Inklusionen dominiert werden (siehe Kapitel 2.5.1), verglichen. Wenn diese beiden Zeitskalen von vergleichbarer Größenordnung sind, muss von Nicht-Gleichgewichtsbedinungen ausgegangen werden.

2D-Experimente wurden in einem Flume durchgeführt, wobei die Sättigung und die Partikelkonzentrationen im Flume mittels Lichttransmissionsmessungen (LTM) beobachtet wurden. Die heterogene Struktur wurde künstlich aus feinen, sehr feinen und groben Glaskugeln hergestellt, da diese transparenter als Sand sind. Das Flume wurde am Boden (-26 cm) abgesaugt, während oben ein konstanter Zufluss ($q = 3.0$ ml/min) angelegt war. Sobald sich ein quasi-stationärer Zustand eingestellt hatte, wurde am oberen Ende des Flumes Tracerflüssigkeit zugegeben. Es wurden hierbei zwei Versuchsanordnungen ("Experiment A" und "Experiment B") untersucht. Um die Durchbruchskurven vergleichen zu können, wurde in beiden Experimenten dieselbe heterogene Struktur geschaffen und die gleiche Menge an Einschlussmaterial verwendet. Weiter wurde bei beiden Experimenten dieselbe Tracerkonzentration von $c = 0.04$ g/l benutzt. Bei Experiment A waren die Einschlüsse aus grobem Material gefertigt, während bei Experiment B sehr feine Glaskugeln verwendet wurden. In beiden Fällen waren die Einschlüsse weniger durchlässig als das Hintergrundmaterial. In Experiment A, bei dem die Einschlüsse aus groben Glaskugeln bestanden, waren die Inklusionen jedoch weniger durchlässig als in Experiment B, da sie nahe an die Residualsättigung hin drainiert wurden. Die aus sehr feinen Glaskugeln bestehenden Inklusionen blieben während des ganzen Experimentes B gesättigt, und somit durchlässiger.

Die dem Experiment vorhergegangene Zeitskalenanalyse hatte ergeben, dass im Laufe von Experiment A Zonen auftreten sollten, in denen der Fluss stagniert, was zu Nicht-Gleichgewichtsbedingungen im untersuchten Gebiet führen würde. Diese Nicht-Gleichgewichtsbedinungen wurden tatsächlich beobachtet. Während des Experiments A wurden die Prozesse in den Einschlüssen von Diffusion bestimmt. Bei Experiment B hingegen blieben die Einschlüsse weiter gesättigt und Advektionsprozesse dominierten, was, wie von der Zeitskalenanalyse vorherge-

sagt, zum Systemgleichgewicht führte (siehe Kapitel 2.5.1).

Die beiden Experimente wurden anhand der Durchbruchskurven verglichen. Zunächst wurde der Infiltrationsprozess von Tracer analysiert. Beim Vergleich der Fronten zeigte sich deutlich, dass in Experiment A eine Verzögerung der Tracerfront auftrat. Die Steigung der Durchbruchskurve war geringer im Vergleich zu Experiment B. Weiter wurden die Durchbruchskurven bei der Infiltration von klarem Wasser verglichen. Hierbei wurde in Experiment A ein starkes Tailing beobachtet, was daran liegt, dass der Tracer in der Inklusion eingeschlossen war.

Beide Fälle wurden mit einer analytischen Lösung verglichen. Dieser Vergleich zeigte, dass die Lösung für den Gleichgewichtsfall bei der Infiltration von Tracer sehr gut mit der analytischen Lösung übereinstimmt. Für den Fall, dass klares Wasser infiltriert wurde, war die Übereinstimmung nicht vollkommen, was offensichtlich an der Verzögerung und dem Tailing der Front im Experiment A begründet liegt.

Zusätzlich wurde festgestellt, dass die Prozesse im Falle der Tracer- und Wasserinjektion nicht äquivalent verliefen. Am Ende der Tracerinjektion waren die Einschlüsse an ihren Rändern stärker gefärbt als in ihrem Inneren (sowohl bei hohen als auch bei niedrigen Konzentrationen). Bei der Wasserinjektion wurde hingegen beobachtet, dass der Tracer umverteilt wurde, das heißt, dass die Farbe in den Inklusionen in diesem Fall gleichmäßig verteilt war. Somit hatte der Konzentrationsgradient zwischen Hintergrund und Einschlüssen im Vergleich zum Fall der Tracerinjektion abgenommen, was zu einer langsameren Entfärbung der Einschlüsse führte.

Im Wesentlichen lassen sich aus diesem Teil der Studie folgende Schlüsse ziehen:

- Der Transport von gelöstem Material unter Gleichgewichts- und Nicht-Gleichgewichtsbedingungen konnte für die durchgeführten Experimente aus der zeitlichen Analyse vorhergesagt werden.

- Das Experiment, welches unter Gleichgewichtsbedingungen durchgeführt wurde (Experiment B), stimmte gut mit der analytischen Lösung überein, während die Ergebnisse des Experiments unter Nicht-Gleichgewichtsbedingungen (Experiment A) starke Abweichungen zeigten.

- Die Infiltration von Tracerflüssigkeit und Wasser in den Flume sind keine äquivalenten Prozesse. Die Umverteilung des Tracers innerhalb der Inklusionen beeinflusste den Konzentrationsgradienten, was zu einer Änderung der Anfangsbedingungen zwischen zwei Injektionen führte.

- Im Falle eines größeren Modellgebiets könnte es, wenn die Inklusionen größer wären und sich die Front noch langsamer bewegte im Untergrund zu sehr starken Verzögerungs- und Tailingeffekten in der Durchbruchskurve

kommen. Dies bedeutet, dass in einem solchen Fall die bestehenden hochskalierten Modelle, die auf Gleichgewichtbedingungen im Kontrollvolumen (REV) basieren, zu sehr schlechten Vorhersagen für den Transport von gelöstem Material führen würden. Dies war bei Experiment A unter Nicht-Gleichgewichtsbedinungen der Fall.

Chapter 1

Introduction and Motivation

1.1 Motivation

In many countries the main source of drinking water is groundwater. For example, in Germany, more then 95% of all drinking water comes from groundwater sources. Those sources represent a large storages of fresh and clean water as groundwater has self-purifying capabilities by filtering itself during the flow through the porous media. Therefore, very often groundwater from sandy aquifers does not have to be treated in order to obtain drinking water quality, since it is purified by filtering in the subsurface. After the industrial revolution in the XIXth century sources of fresh groundwater have been polluted by many industrial sites (e.g. by NAPL). The contaminants have been usually deposited in the subsurface. Therefore, a leakage of contaminant in such sites usually caused a long term contamination of fresh groundwater. Nevertheless, the contaminants were very often spilled at the ground surface, infiltrating towards an aquifer through the unsaturated zone (see Figure 1.1). Moreover, the transport of contaminants into aquifers becomes a problem especially in agricultural areas, where large amounts of fertilizers and pesticides are used. When the levels of contaminants (e.g. nitrate) in the drinking water becomes too high, protection areas have to be assigned where no fertilizers or only reduced amounts are allowed.

In order to prevent pollution of underlying aquifer with infiltrating polluted water several remediation techniques could be used to avoid and remove the contamination. Therefore, it is very important to predict the typical infiltration times, so the right remediation technique could be used (financially and environmentally). For example, if the polluted water is trapped in fine soil lenses and cannot be easily mobilized, no remediation measures might be needed since natural biodegradation usually could take place. Nevertheless, water could infiltrate towards an aquifer through preferential flow paths or it could be blocked with structures of low permeability. In order to predict such a variety of different situations in the unsaturated zone, we need to develop good, efficient and reliable

numerical models, which could describe and predict the processes occurring in the subsurface.

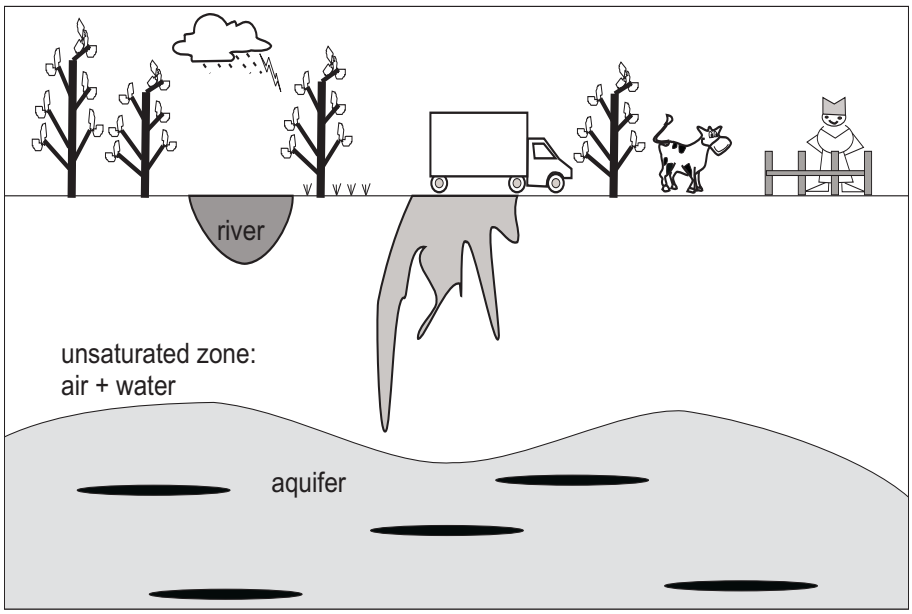

Figure 1.1 Infiltration of contaminant towards an aquifer.

The modeling of flow and transport in the unsaturated zone is a very challenging task. As mentioned, the unsaturated zone represents a transition zone for contaminants spilled on the ground surface and by reaching an underlying aquifer causes groundwater pollution. In contrary to the saturated zone, pores in the unsaturated zone between the soil grains are partly filled with water (liquid phase) and partly with air (gas phase), where the presence of one phase has an influence on the flow of the other phase. Therefore, it is very important to have a good knowledge about complex interactive processes in the subsurface in order to be able to predict them correctly. Main problems when modeling flow in the unsaturated zone are the heterogeneous structures of the soil as well as various processes occurring in this zone. Also, available models, which describe the fluxes and transport in the unsaturated zone are well established for porous media on a meter scale and tested mainly under equilibrium conditions in the laboratory. Their applicability for water balance models on a much larger scale, which can stretch over kilometers, is discussed controversially in the literature (e.g. Harter and Hopmans [24]).

1.1.1 Challenges in modeling of flow and transport in the unsaturated zone: Heterogeneous structure

Since soil is very often highly heterogeneous, soil parameters often vary over orders of magnitude. When flow and transport in the unsaturated zone are modeled, the heterogeneities of the soil can not be generally resolved in details. In practice, the heterogeneities are never known in detail and even if they are, the computational demand would be enormous in order to handle that amount of data (Figure 1.2-left). For example, data are obtained from boreholes, where soil parameters are measured (e.g. hydraulic conductivity or grain size distribution). In between usually interpolation measures are taken using different techniques (e.g. geostatistical methods) in order to describe heterogeneous fields. Recently, there are new, more advanced measurement techniques like electric resistance tomography (ERT) [83], where the information about the soil on the field scale could be obtained as a 2D cross section between two boreholes. Nevertheless, none of the advanced methods give a complete overview of the structure in the subsurface. Complete knowledge of the structure demands very high costs, which would also lead to huge data processing and long computational times. Therefore, we usually aim to have a model with a simpler characterization of heterogeneities still being able to give good predictions of the complex processes occurring in unsaturated zone. Flow in the unsaturated zone is very often modeled in an average sense, where the input parameters of the model are spatially averaged (Figure 1.2-right). Derivation of those simplified models is called upscaling.

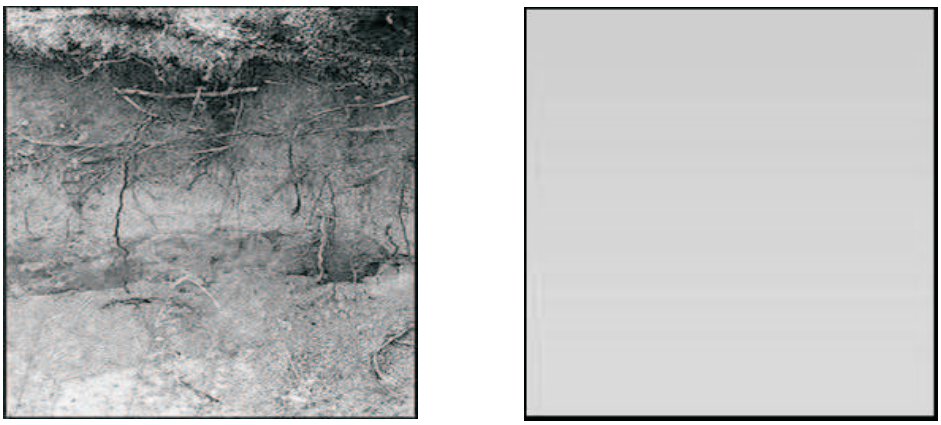

Figure 1.2 Left: Heterogeneous structure. Right: Simplified homogeneous structure.

1.1.2 Upscaled models for flow and transport in the unsaturated zone

Upscaling of flow and transport in the unsaturated zone is a big and active field of research. In upscaled models, as they are sort of averaged models, the effect of the small scale heterogeneities is captured by means of effective parameters. Using upscaled models the computational time is reduced, but the output results are also influenced by such simplifications. Sometimes, certain processes can be neglected in the averaged model. It can, however, also be the case that processes not present in the heterogeneous model are required to model the averaged quantities correctly. Still, good upscaled models have to give efficient and reliable predictions of the flow and transport in the unsaturated zone and to reduce the computational time for the complex models. Two major problems could be recognized, when upscaled models are used:

1) Estimation of effective parameters: The effective parameters have to capture the influence of small scale heterogeneities (such as e.g. preferential flow paths or layers with low permeability). In Figure 1.3, two heterogeneous fields with the same second order statistical properties (mean and covariance function) are presented. Nevertheless, it is obvious that the field in Figure 1.3-up has a connected path of material with high conductivity, whereas in the Figure 1.3-down highly permeable areas are isolated. The flow and transport processes occurring in the presented fields would differ in a big manner due to different connectivity between regions of high permeability. Therefore it is very important that derived effective parameters capture these structural properties in order to have good predictions with upscaled models.

If the structure of the medium is known in detail, the effective parameters for the upscaled model could be derived exactly. Since in practice this is very often not the case as it needs a huge amount of effort, measurements and financing, the effective parameters have to be estimated based on the little information available about the subsurface. Therefore, the heterogeneous structure of the soil has to be characterized in an efficient way in order to capture the main structural properties of the soil. It is necessary to investigate how the soil structure (e.g. connectivity or different arrangement of heterogeneities) influences the estimation of the effective parameters in the unsaturated zone, when upscaled models are used. This topic is still an open question, although some work has already been done.

2) Assessment of assumptions made in upscaled models: There are several upscaling techniques, which are often used in order to upscale flow and transport in the unsaturated zone. All upscaled models, which are derived using those techniques, have several assumptions, which have to be considered. Generally,

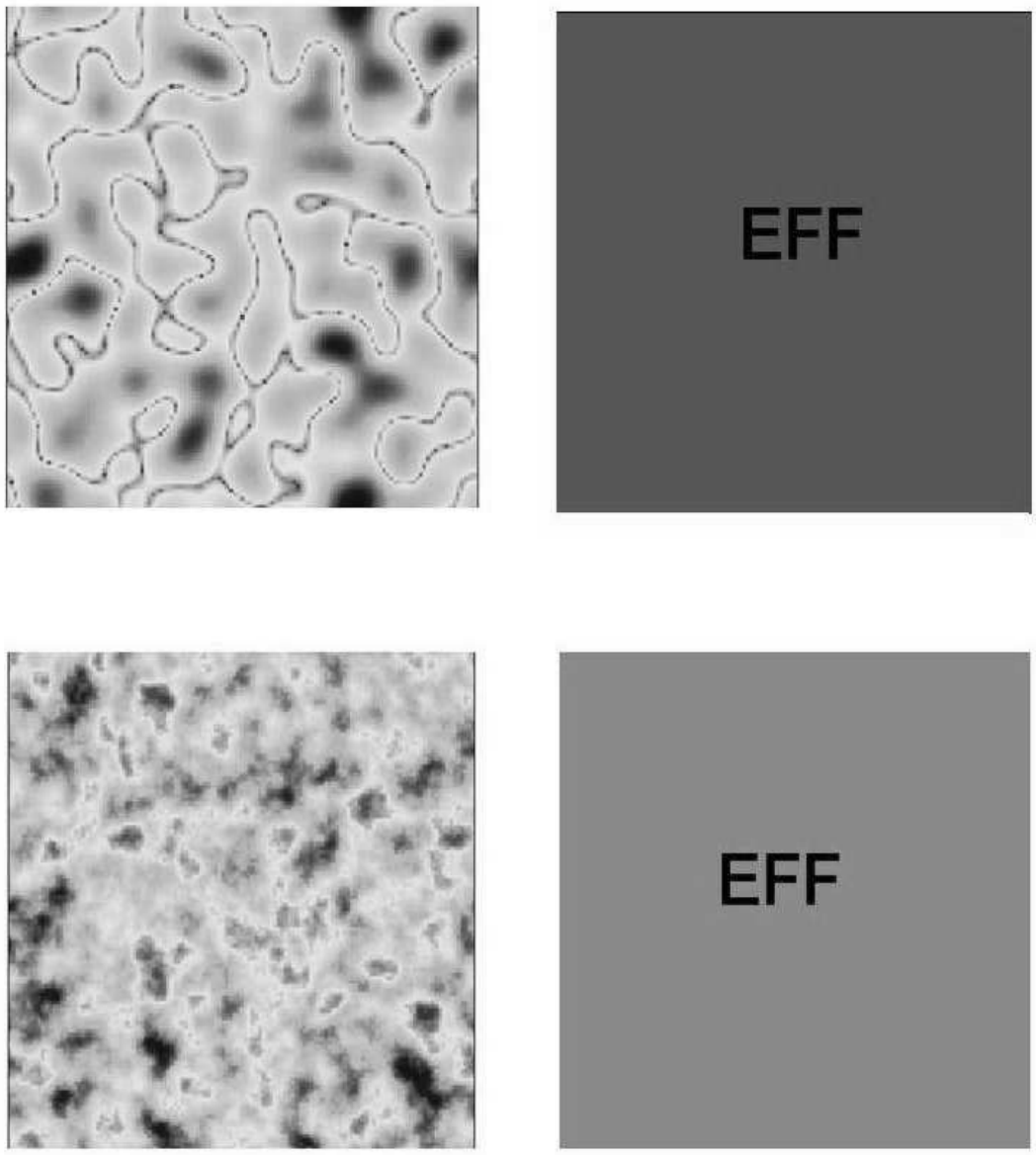

Figure 1.3 Two Gaussian fields with the same statistical properties, but with different structural properties, which need to be captured by effective parameters. Up: High permeable material is connected. Down: High permeable material is isolated.

upscaled flow and transport models are derived for equilibrium conditions in the laboratory, meaning that the water content inside of a representative elementary volume (REV) is at steady state. This is one of the major and typical assumption. Furthermore, some models assume a periodicity of the modeled field whereas some models are valid only for certain parameter contrasts between soil parameters. Applicability of those models could be questionable for water balance models on a much larger scale as some assumptions would not be valid. Thus, all assumptions need to be evaluated and assessed in order to determine if the used upscaled model gives good predictions of processes occurring in the unsaturated zone.

To summarize, one could see that modeling in the unsaturated zone is not an easy task. Highly heterogeneous structures, lack of field data and very complex processes are the main causes of difficulties. Simplified models (upscaled) are used in order to resolve heterogenous structures in a more efficient way. They have to be simple, but still to capture a variety of processes occurring in the subsurface by means of appropriate estimation of effective parameters. Their estimation highly depends on the structure of the subsurface. How the structure really influences the predictions in the unsaturated zone is still an open question. Last, but not least, upscaled models are derived under certain assumptions. A necessary and challenging task is to assess those assumptions, before upscaled models are used.

Still, many open questions in the field of upscaling exist. In order to be able to answer some of them related to the mentioned problems above, in this study existing upscaled models for flow and transport in the unsaturated zone are used and tested by means of comparison to experiments.

1.2 Flow and transport in the unsaturated zone

1.2.1 Upscaling methods

If the detailed processes inside a heterogeneous porous medium are not the main goals of interest, it is unnecessary to model the processes in detail. Instead, equivalent models are used, which describe the processes in average. The heterogeneous model is thus replaced by an equivalent homogeneous model (see Figure 1.2-right). The upscaled model has to be derived from the knowledge we have about the detailed processes in the heterogeneous model. This upscaled model incorporates certain processes and has parameters which are no longer heterogeneously distributed. These homogeneous parameters are called equivalent parameters or effective parameters. The effective parameters are generally independent on the large-scale boundary conditions (see Renard and de Marsily [64]).

Different approaches are used to derive upscaled models. Some of those methods are listed here:

- Deterministic approaches:

  - Volume averaging
  - Homogenization

- Non-deterministic approaches:
  - Effective medium theory
  - Stochastic theory
  - Coarse graining
  - Renormalization.

Deterministic approaches: Volume averaging and homogenization are deterministic approaches since they are used explicitly to derive the equations for the spatially averaged variables for a given specific parameter field (parameter fields are explicitly known). The effective parameters for the upscaled models can, also be derived using a stochastic description of the parameter field.

Volume averaging (e.g. Whitaker [85]) is applied to a composite of materials separated by sharp interfaces. The flow equation is averaged over a certain averaging volume, where the volume average has to be considered a moving average. Usually, the averaged problems can not be derived in a closed form. Therefore, closure problems have to be formulated and solved. Explicit results for the upscaled models are mostly obtained for periodic media and for the condition that the averaging volume covers a REV. Volume averaging method does not make many "a priori" assumptions.

In *homogenization theory* (e.g. Hornung [31], Sanchez-Palencia and Zaoui [67], Bensoussan et al. [47] and Cioranescu and Donato [8]), contrary to volume averaging, there are some (quite strong) assumptions made about the relation of the scales. Periodicity of the field have to be assumed. Upscaled model for flow and transport derived by homogenization may use either stochastically or deterministically periodic fields. An upscaled form of the flow equation in the unsaturated zone (Richards equation) for a periodic field based on homogenization theory was derived by Lewandowska and Laurient [45] and Neuweiler and Cirpka [53]. This equation allows to account for a variety of different properties of the parameter field, including connectivity of highly permeable and poorly conductive regions.

Non-deterministic approaches: In practice, however, parameter fields are not explicitly known. Instead, heterogeneity is quantified by certain stochastic measures, which have to be derived from few and sparse data, often supported by rather point-like small measurement volumes only. Therefore, methods are required which allow to estimate the upscaled parameters without deterministic knowledge of the structure.

The effective medium theory (e.g., Pozdniakov and Tsang [60]) has often been used to derive effective conductivity for flow in soil with known background material and inclusions of unknown spatial distribution and unknown material properties. This theory often works quite well in practice. Effective medium theory methods (e.g., Torquato [77]) such as the self-consistent approach (e.g., Fokker [17] or Pozdniakov and Tsang [60]) or the Maxwell method (e.g., Zimmerman et al. [93],[92]) are based on knowledge of the volume percentage of inclusion materials and their individual conductivities only. The Maxwell approach additionally uses information about background material and inclusions. For example, Fokker [17] used the self-consistent approach in order to derive the effective conductivity for single phase flow in the case of a general 2D anisotropic medium, while Podzniakov and Tsang [60] applied the self-consistent approach to obtain the 2D and 3D effective conductivity of fractured porous media. Zimmerman et al. [93] used the Maxwell approach to determine the effective conductivity for fractured media. Afterwards, Zimmerman et al. [92] used two effective medium theories, the Maxwell method and the differential method to estimate the effective conductivity of a 2D medium consisting of a random distribution of elliptical inclusions in an otherwise homogeneous matrix.

The stochastic theory allows a more comprehensive description of soil structure (e.g. Gelhar [20], Dagan [10], Zhang [91], Rubin [66]). Due to the lack of deterministic knowledge on the soil structure, it is reasonable to use stochastic approaches, where spatially heterogeneous parameter fields are represented by correlated random space variables. Nevertheless, in case of the stochastic theory, in order to keep the model simple, the parameters are often assumed to be second-order stationary random fields, characterized by their mean, variance and correlation length (e.g., Kitanidis [39]). The permeability field is mostly assumed to be log normally distributed and variances are supposed to be small (less than 1) in order to apply linear techniques, which is not common in natural soils. Furthermore, the characteristics of channeling flow are poorly captured by second-order statistic models.

In *coarse graining*, the upscaled model is not homogeneous, but the heterogeneities are averaged out only in part. The parameters of the upscaled model are still heterogeneous, but the characteristics of the heterogeneity have changed (see Hristopulos [32], King and Neuweiler [38] and Attinger [2]). Generally, coarse graining is often applied in the context of grid coarsening in numerical models (e.g. Durlofsky [12] and Durlofsky [13]).

Renormalization uses such successive steps to derive a relation between scaled and averaged properties. Renormalization has also been used to average flow and transport problems in the subsurface (King [37], Hristopulos [32], Attinger [2], Jaekel et al. [33]).

All upscaled models and their effective parameters are derived under certain assumptions. Some of them are already mentioned above (e.g. periodicity of the

field or a small contrast between parameters in case of homogenization theory). One very important assumptions is that upscaled flow and transport models in porous media on larger scales usually imply inherently also an equilibrium assumption for the REV of the model, meaning that the water content inside of a REV is at steady state. However, the heterogeneous substructure of a REV may cause flow behavior inside a control volume with typical time scales, which are comparable to typical time scales for water flux over the whole medium. Such effects cause tailing and retardation of water content or tracers, leading to **non-equilibrium** conditions for flow and transport in the unsaturated zone.

1.2.2 Non-equilibrium models derived using upscaling

Modeling of flow: In the unsaturated zone heterogeneous substructures could influence the flow regime and lead to non-equilibrium conditions. This often occurs due to high parameter contrast between materials. Non-equilibrium in a domain could either result in bad model predictions or could have negligible effects. Therefore, it is necessary to asses how strong this effect influence model predictions made by equilibrium models and how to cope with it.

It is purposed by Lewandowska et al. [46] to use a double-continuum approach in case of large scale non-equilibrium due to high parameter contrast. To estimate if such phenomena may have to be accounted for in a model concept, the typical time scales for the equilibrium need to be estimated. The estimation of time scales is, however, for two phase flow phenomena not straightforward, as the parameters are not fixed numbers but depend on the variables in the medium (see Hilfer and Øren [29]). Since the parameters usually vary much in time and space, the corresponding time scales or dimensionless numbers can vary over many orders of magnitude, depending on the choice of the reference variables. The double-continuum approach can be successfully used if typical time scales are reliably estimated.

The approach of Lewandowska et al. [46] is comparable to the double continuum approach of Gerke and Van Genuchten [21]. Beside Gerke and Van Genuchten [21], non-equilibrium models for flow in the unsaturated zone were also proposed by Jarvis [34], Zimmerman et al. [94] and Ross and Smettem [65]. Zimmerman et al. [94] proposed an approach to simulate unsaturated flow processes in dual-porosity media such as fractured rocks or aggregate soil. They described fluid flow between the fracture network and matrix blocks by a non-linear equation that relates the imbibition to the local difference in the liquid-phase pressure between the fractures and the matrix block. Ross and Smettem [65] proposed to combine the Richards equation with a dynamic description of the approach to equilibrium by a first order time constant equilibration model of infiltration, because water in soil (e.g. large aggregates or pore-class heterogeneity) may exhibit non-equilibrium between the actual water content and that given by

the retention curve (the water could penetrate deeper than predicted with the classical infiltration theory). Simunek et al. [72] provided an extensive review about the non-equilibrium models.

Similar non-equilibrium conditions may, however, also occur in the unsaturated zone for smaller saturated parameter contrasts if the materials are well sorted with distinct air entry pressures. The surrounding material drains before the inclusions, leading again to a high parameter contrast. The typical time scale for such a drainage may be small. The reduced conductivity of the surrounding material keeps the water for a long time in the fine material, leading to a large time scale for the drainage of the inclusion. This leads also to conditions far away from local equilibrium.

Modeling of transport: As in the case of flow, a large parameter contrast between materials within the domain could lead to non-equilibrium. That could cause a retardation or tailing of the contamination (tracer) front. Therefore, this causes an earlier or later front arrival, when upscaled models are used. How strong the deviations from our upscaled model derived under equilibrium are and whether we need to include those effects into our upscaled model are also environmentally very significant questions.

In the framework of solute transport, a non equilibrium behavior due to large parameter contrasts in the unsaturated zone could be observed at larger scales as an early breakthrough or long tailing (e.g. Brusseau et al. [7], or Fesch et al. [16]). This phenomenon can not be represented by a classical advection-dispersion equation. Therefore, some classes of such highly heterogeneous structures may again be, as in the case of flow, represented by a simplified system consisting of two homogeneous porous media. If solute transport characteristic times between those two regions are relatively different, a significant difference between two concentrations is observed. This phenomenon must be taken into account in large scale models (see Quintard and Whitaker [62]). Quintard and Whitaker [62]) have considered the transport of an adsorbing solute in a double continuum model. The extension of the analysis to multi continuum models is straight forward but tedious. Even for complex structures (natural formations), this approach proved to be very useful in many practical applications (e.g. Goltz and Roberts [22], Bajracharya and Barry [3]), Larsson and Jarvis [42], Feehley et al. [14]). Goltz and Roberts [22] injected two inorganic tracers and five organic solutes in an unconfined aquifer. They showed that the mass non-equilibrium models simulate the sharp breakthrough and extended tailing exhibited by the experimental responses better than the model assuming equilibrium sorption. Feehley et al. [14] simulated a large-scale natural-gradient tracer test in a highly heterogeneous aquifer using 3D hydraulic conductivity distributions derived from borehole flowmeter test data. The double continuum mass transfer model is able to represent the rapid, anomalous spreading significantly better while retaining

high concentrations near the injection point. This study demonstrates that the double continuum mass transfer approach may offer a practical solution to modeling solute transport in highly heterogeneous aquifers, where small-scale preferential flow pathways cannot be fully and explicitly represented by the spatial discretization of the numerical model. A recent overview of the double continuum approaches and data requirements is provided by Griffion et al. [23].

It is clear that there are various models, which could deal with non-equilibrium for flow and transport. However, they are used in certain situations based on estimated time scales. It is still not clear how those time scales should be estimated using dimensional analysis in order to derive criteria for the applicability of non-equilibrium models. For example, the macroscopic dimensional analysis from Hilfer and Øren [29] differs fundamentally from the traditional analysis (Leverett et al. [44], Rapaport [63], Geertsma et al. [19] and Perkins and Collins [58], where instead of using the microscopic entry pressure to normalize the pressure field Hilfer and Øren [29] used a representative (typical) pressure from the capillary pressure curve. Thus, estimation is not straight forward. Therefore, difficulties about how time scales could be estimated have to be illustrated on simpler examples, where estimation of time scales could be compared with experimental results.

1.2.3 Experiments performed in the unsaturated zone

Many experiments have been performed in the unsaturated zone from pore to field scale. In this study existing upscaled models for flow and transport are compared to experiments by focusing on well controlled experiments with a known artificially created structure.

Ursino and Gimmi [79] packed a thin tank with three different sands (fine, medium and coarse) using cubes of $5\times5\times5$ cm^3. The layers were 0.5 cm thick and their sequence was random. The cubes were saturated, frozen and assembled in the tank ($55\times40\times5$ cm^3) at the inclination of 45 °. They performed tracer experiments in this tank in order to investigate the influence of heterogeneity, anisotropy and saturation on steady state flow and transport. They found that low saturation led to very large heterogeneity and to strong preferential flow. Thus the description of the flow paths and the prediction of the solute arrival times require, in this case, more accurate knowledge about the topological structure. Saturation-dependent macroscopic anisotropy is an essential element of transport in unsaturated media. For this reason, small structural soil features should be properly upscaled to give appropriate effective soil parameters as input in transport models.

Wildenschild et al. [87] conducted a study that consisted of a series of infiltration experiments in a laboratory tank of $100\times110\times8$ cm^3, packed with sand in known heterogeneous configurations. A statistically uniform distribution of

the different sands in the tank was assured by using a random number generator to assign soil types to a predesigned 2D grid. The sizes of the individual heterogeneities in the 2D grid were cells of $5\times10\times8$ cm^3. Solute breakthrough curves measured at discrete points as well as dye tracer paths, showed that flow and transport took place in a very tortuous pattern where several grid cells were completely bypassed. The degree of tortuosity appeared to be dependent on the degree of saturation. Despite the tortuous flow patterns, they found that the effective unsaturated hydraulic conductivity as well as the retention curves for the three realizations of the heterogeneous sand were quite similar, thus suggesting that this type of heterogeneous flow system can be treated as an equivalent homogeneous medium characterized by effective parameters.

In both experiments presented above (Ursino and Gimmi [79] and Wildenschild et al. [87]), in order to observe saturations and concentrations in the tank non-invasive measurement methods for water content and concentration are needed. Therefore, several techniques have been developed in the past in order to monitor spatial water distribution as well as concentrations within the sample and to obtain information in porous media under unsaturated conditions. For example, magnetic resonance imaging (Johns et al. [35]) provides 3D information of the water content. Ferrand et al. [15] and Oostrom et al. [57] measured pointwise fluid content in the column by means of dual-energy gamma radiation. McBride and Miller [49] used X-ray attenuation for the measurement of fluid content. Tidwell et al. [75] measured the 2D water distribution in a thin slab chamber using the combination of X-ray absorbtion and visible light transmission. The method using the visible light transmission (light transmission methods - LTM [75]) is limited as the porous media have to be non opaque. Therefore, instead of sands, glass beads are used as they are more light transparent. The LTM are very often used in laboratory experiments to make observation of unsaturated zone processes including water and solute distribution, colloid transport, NAPL phase flow (e.g. Niemet and Selker [54], Weisbrod et al. [84], Schroth et al. [71], Yarwood et al. [88]). Heiss et al. [27] investigated the DNAPL front movement in an initially water saturated flume using the same technique. A 3D measurement of water content in soil samples with X-ray absorption is also possible, but a high spatial resolution requires a large time span for one scan. Bayer et al. [5] used slices through the samples in order to reduce the scanning time and to monitor rapid transient changes in the sample. DiCarlo et al. [11] used high-speed measurements with synchrotron X-rays and were able to monitor the transient flow behavior in a 2D flume. However, their method was limited to a small section of the flow field due to the size of the beam. Recent developments in microscale visualization techniques gave a possibility for imaging pore scale flow processes in 3D. Wildenschild et al. [86] used synchrotron based X-ray microtomography to visualize 3D samples. The sample was limited to a few centimeters. Recently neutron rays have been used in order to monitor spatial water distribution (Has-

sanein et al. [25] or Vasin et al. [82]). For larger samples (up to 10 cm thickness and 20 cm height) a slow neutron tomography has been used (e.g. Schaap et al. [70]) in order to obtain a 3D spatial water distribution. Beside slow neutron tomography mentioned above, where 3D spatial water distribution was measured only when the samples were the equilibrium, fast neutron tomography (see Hassanein et al. [25], Masschaele et al. [48], Schaap et al. [70]) could be used to monitor a transient water distribution in the samples. This method allows a 3D observation of water content with a very good resolution in time and space if the samples are small enough.

All mentioned monitoring techniques have mostly been used for drainage experiments in order to observe spatial water distribution as well as concentrations. Drainage experiments performed in unsaturated porous media could be carried out with one or more drainage steps (single and multi-step drainage experiments), where controlled unsaturated conditions within the samples could be reproduced. Multi-step drainage experiments are carried out in porous media with one or more open boundaries and a fixed pressure head at the bottom. Those experiments are often used to determine the hydraulic properties of soil materials such as for example hydraulic conductivity and entry pressure. Parameters are estimated from the measured mass of outflowing water after changing the boundary pressure by means of the inverse modeling. This kind of experiment is first time introduced by Gardner [18]. Some authors, who have used multi-step outflow experiments in order to define the soil parameters are Bayer et al. [4], Kool et al. [40], Sang et al. [68], Toorman et al. [76] or Zachmann [89], [90].

1.3 Open questions

There is a large amount of experimental effort in order to preform experiments in the unsaturated media as well as a large theoretical effort to derive upscaled models and estimate effective parameters. Nevertheless, there is still a huge gap between experimental work and upscaled models. There are many open questions how to capture structural influence when estimating effective parameters as well as which assumptions made during derivation of a certain model are important to be assessed for a defined problem. Therefore, one purpose of this study was to bridge the gap between theoretical and experimental work in the field of upscaling.

The first open question **(Question 1)** that rises is how to characterize and quantify the **influence of the soil structure on effective parameters** used for upscaled models for flow in the unsaturated zone. As mentioned, the detailed heterogeneity distribution in the unsaturated zone is rarely known, but still influence of small scale heterogeneities has to be captured. Any useful information of the soil structure (e.g. volume percentage) have to be included in the estimation process. One important goal of this study is to discuss how those estimations

would be influenced by different soil structures (see Figure 1.3).

Secondly **(Question 2)**, upscaled models can not be used in general for all field cases and applications since they are derived under certain assumptions (e.g. periodicity of the field, small parameter contrast etc.). Therefore, the second question is how applicable are the upscaled models to predict flow and transport processes in the unsaturated zone, when those **assumptions are not strictly met**.

The third question **(Question 3)** is focused to the assumption that usually equilibrium conditions are implied, when deriving upscaled models. However, dependent from the parameter contrasts between materials, upscaled models could be derived either for **equilibrium (small parameter contrast) or non-equilibrium (high parameter contrast)** conditions. In order to be able to decide, which model (equilibrium or non-equilibrium) is more suitable for modeling a certain process, typical time scales have to be estimated. However, this is not an easy task. Therefore, time analysis is discussed in more detail during this study.

The three questions mentioned above are illustrated and tried to be answered on several specific cases by performing different experiments. The answers to the mentioned questions can not be considered as general ones since results are obtained from well controlled experiments and simple examples (e.g. drainage experiments). The experiments were designed to match as close as possible the theoretical models and the samples were created with artificial porous media. MUFTE-UG [28] has additionally been used in order to simulate experiments in this study.

1.4 Methodology and overview of the performed experiments

In this study upscaled models for flow and transport in the unsaturated zone derived by means of homogenization theory were used. They were tested by means of comparison to experiments. An upscaled model for flow in the unsaturated zone under equilibrium used in this study was derived by Lewandowska and Laurient [45] and Neuweiler and Cirpka [53]. This equation allows to account for a variety of different properties of the parameter field, including connectivity of highly permeable regions and of poorly conductive regions. In case of flow under non-equilibrium the upscaled model has been derived by Lewandowska et al. [46]. The same upscaling technique has been used here to derive an upscaled form of transport equation for a conservative tracer under equilibrium and non-equilibrium conditions.

In order to illustrate the influence of different soil structures on the estimation of effective parameters (Question 1), multi-step drainage experiments with

two columns having substantially different structures, were performed. Two artificial structures were created using two different sand types (fine and coarse sand). Here, structure subsumes two properties: connected vs. isolated structures and periodic (regular) patterns vs. random patterns without the finite correlation length. The two columns with significantly different structures had the same percentage of coarse sand in order to be comparable with respect to measured outflow and spatial water distribution during the multi-step drainage experiments. Beside the outflow from the columns the 2D/3D spatial water distribution was measured by means of slow thermal neutron radiography/tomography (Hassanein et al. [25]). The slow thermal neutron tomography (3D images) was used for the equilibrium states after each pressure step, and the neutron radiography (2D images) for the transient flow between two pressure steps. In order to estimate the effective parameters the Maxwell and self-consistent approach [77] were used, which use only information about the volume percentage of both sands. Those estimation could be compared to the performed experiment as well as to parameters derived directly from homogenization theory as the structures of the columns were known in details.

The upscaled model for flow under equilibrium conditions in the unsaturated zone derived by Cirpka and Neuweiler [53] using homogenization was obtained under periodicity as well as small parameter contrast assumptions. By using a randomly packed column as a test case, this study also addresses the applicability of upscaled models in cases where the underlying periodic assumption is not met (Question 2). This has been done by a comparison between experimental results and results from 3D heterogeneous and 1D upscaled numerical simulations with respect to outflow curves and spatial water distributions in porous media during multi-step drainage experiments. Also, both columns were numerically tested, when they were in very dry regimes, meaning that parameter contrast between soil materials was significantly increased, not fulfilling the assumption of equilibrium (small parameter contrast) anymore (Question 2).

In case of large parameter contrast between soil materials non-equilibrium might occur. As mentioned, in order to distinguish, which model is more suitable (equilibrium or non-equilibrium) for modeling of flow and transport processes, typical time scales have to be estimated (Question 3). In case of flow, a non-equilibrium situation for flow may occur if water is retarded in inclusions, which are of fine material compared to the surrounding coarse material. Non-equilibrium occurs due to reduced permeability of the surrounding coarser material during the drainage process causing high parameter contrast. When the surrounding (coarser) material drains close to residual saturation at pressures, which are below the entry pressure of the finer material (inclusions), the relative permeability of the coarser material becomes very low. After the pressure in the medium exceeds the entry pressure of the finer material, the water in inclusions cannot drain due to the almost impermeable surrounding coarse material.

The column drainage experiment has been performed in order to observe the non-equilibrium condition mentioned above for flow due to the large parameter contrasts, where beside the outflow, 3D transient spatial water distribution has been monitored by means of fast neutron tomography. The column was packed with the same fine and coarse sand as in the previous experiments. The whole structure consisted of two inclusions made of cubes of fine sand surrounded by coarse sand. Different concepts to estimate the equilibrium time were compared and illustrated in this simplified example.

The same question (Question 3) rises in case of solute transport as well. In order to distinguish, which upscaled model (equilibrium and non-equilibrium) is more suitable, the time analysis has to be performed. To illustrate and further investigate time analysis in case of equilibrium and non-equilibrium solute transport, 2D transport experiment in a thin flume have been performed, where the concentration and water distribution have been observed by LTM [75]. Glass beads were used since they are more light transparent. The heterogeneous structures in the flume were created with three different sizes of glass beads (very fine, fine and coarse). At the top of the flume, a tracer has been infiltrated. Afterwards, infiltration has been again switched to clear water. Prior to the experiments typical time scales were estimated in order to assess if non-equilibrium in the system could be predicted.

1.5 Structure of the thesis

At the beginning of the thesis (Chapter 2) models for flow and transport in the unsaturated zone with heterogeneous parameters will be explained. Later on, in the same chapter, upscaled models (1D) for flow and transport under equilibrium and non-equilibrium conditions derived by homogenization theory will be presented.

After the theoretical part, in the first part of Chapter 3, multi-step drainage experiments on two sand columns with different structures will be shown. Discussion on the estimation of effective parameters for different structures will be presented. Also, the applicability of an upscaled flow model derived under equilibrium condition, when assumptions of periodicity and small parameter contrast are not fulfilled will be addressed in the first part of this chapter. The second part of Chapter 3 presents the multi-step experiment, where trapping (non-equilibrium) of water has been observed due to the high parameter contrast. Predicted time scales of drainage in the sample estimated prior to the experiment will be shown and compared to the experimental and numerical results.

In Chapter 4, solute transport experiments under equilibrium and non-equilibrium in 2D flume will be shown. Estimated time scales will be compared to experimental data and further discussed with respect to influence of non-equilibrium

on solute transport modeling, when upscaled models are used.

Finally, in Chapter 5, the conclusions will be presented.

Chapter 2

Flow and transport processes in the subsurface for a single phase

2.1 Flow of a single fluid in the saturated zone

Henry Darcy (1856) has done the first experiments with the flow in saturated porous media (Figure 2.1). He defined specific discharge (Darcy's velocity) q as discharge Q per cross sectional area A (equation 2.1) and observed that specific discharge through the sample is proportional to the hydraulic gradient $\Delta h/\Delta l$ (equation 2.2).

$$q = \frac{Q}{A}, \tag{2.1}$$

$$q = -K\frac{\Delta h}{\Delta l}, \tag{2.2}$$

where the proportionality constant is known as the hydraulic conductivity K [$\mathrm{L\,T^{-1}}$] and h is used as the hydraulic head [L]. The negative sign expresses that water flows from high to low piezometric head. The hydraulic head is defined as:

$$h = \frac{p}{\rho g} + z, \tag{2.3}$$

where: p [$\mathrm{M\,L^{-1}\,T^{-2}}$] is pressure, g [$\mathrm{L\,T^{-2}}$] gravity acceleration, z [L] elevation and ρ [$\mathrm{M\,L^{-3}}$] density.

As the pore space of the medium during the Darcy's experiment is not resolved, the Darcy's velocity is related to the flow velocity $\vec{v}$ as

$$\vec{q} = \phi\vec{v}, \tag{2.4}$$

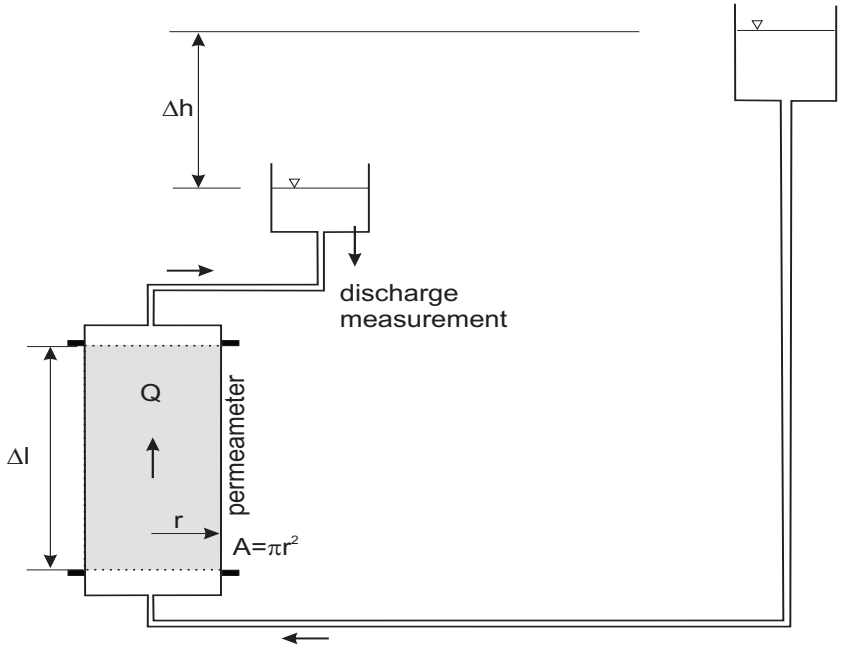

Figure 2.1 Setup of Darcy's experiment.

where ϕ [-] is the porosity of the medium.
The Darcy's equation could be written as follows:

$$\vec{q} = -K\vec{\nabla}\left(h + z\right), \tag{2.5}$$

and the mass continuity of water in the porous medium:

$$S_{\mathrm{f}}\frac{\partial h}{\partial t} + \vec{\nabla}\cdot\vec{q} = s, \tag{2.6}$$

where S_{f} $[L^{-1}]$ is the storage coefficient, which accounts for storage of water due to compression of the water or of the porous material, and s stands here for external sources and sinks.

2.2 Flow in the unsaturated zone: Richards equation

In the unsaturated zone the porous media is occupied by two fluids (air and water). It is usually assumed that the air is always connected to the surface. It is also usually assumed, that as the viscosity of air is two orders of magnitude smaller than that of water ($\mu_{\mathrm{air}} = 1.710^{-5}$ kg/(ms), $\mu_{\mathrm{water}} = 1.010^{-3}$ kg/(ms)), air can compared to water always be assumed to be in equilibrium. The air

pressure is thus considered to be constant. In principle the air is then at atmospheric pressure, however, atmospheric pressure is often set to zero for simplicity. This assumption simplifies the system of two-phase flow equations. As the air is considered as stagnant in the background, the flow of air does not have to be considered, and the only relevant fluid is water. As the air pressure is set to zero, the water pressure head is identical to the negative capillary pressure head (h_c),

$$\frac{p_\mathrm{water}}{\rho_\mathrm{water} g} = \frac{p_\mathrm{air} - p_\mathrm{c}}{\rho_\mathrm{water} g} = -\frac{p_\mathrm{c}}{\rho_\mathrm{water} g} = -h_\mathrm{c}. \tag{2.7}$$

The conductivity for any of two fluids is affected by the presence of the other fluid. The smaller the saturation of the fluid, the smaller also the conductivity. Therefore, we define the relative permeability as the ratio of the effective permeability for a fluid at the given saturation to the permeability at full saturation. Therefore, Darcy's law for unsaturated zone read as follows and it is called Buckingham-Darcy's law:

$$\vec{q} = -K_\mathrm{u}\left(h_\mathrm{c}\right)\left(\vec{\nabla} h_\mathrm{c} + \vec{e_\mathrm{z}}\right), \tag{2.8}$$

$$K_\mathrm{u}\left(h_\mathrm{c}\right) = k_\mathrm{r}\left(h_\mathrm{c}\right) K, \tag{2.9}$$

where K_u the unsaturated hydraulic conductivity tensor [$\mathrm{L\,T^{-1}}$] and k_r the relative permeability [-]. The continuity equation for the unsaturated zone is called Richards equation:

$$\frac{\partial \Theta_\mathrm{w}\left(h_\mathrm{c}\right)}{\partial t} - \vec{\nabla} \cdot \left(K_\mathrm{u}\left(h_\mathrm{c}\right)\vec{\nabla} h_\mathrm{c} + K_\mathrm{u}\left(h_\mathrm{c}\right)\vec{e_\mathrm{z}}\right) = s, \tag{2.10}$$

where Θ_w [-] is the water content. In principle, the parameter functions $\Theta_\mathrm{w}(h_\mathrm{c})$ and $K_\mathrm{u}(h_\mathrm{c})$ are subject to hysteresis. As only primary drainage is analyzed in this thesis, hysteretic behavior is neglected in the following.

As mentioned, the Richards equation (equation 2.10) is derived under the assumption that the air is always connected to the atmosphere. Therefore, Richards equation describes only the flow of one phase (water) as air phase is always connected to the atmosphere. However, for small to medium saturations, this assumption is feasible. Sometimes soil gas may be trapped within the wet soil. This situation is not captured by Richards equation, therefore, one has to be careful with using it. Situation, when the air in entrapped could be described by multi phase flow, but on the other hand it is much more computation demanding compared to one phase flow.

2.3 Solute transport in the unsaturated zone

If substances are soluble in a fluid (usually water), they are transported with the flowing fluid through the porous medium. Such a scenario is important if a contaminant is released into groundwater. An example is the use of nitrate for agricultural purposes. The nitrate on the field is washed out with precipitation and infiltrates the underlying aquifer through the soil (see Vasin [81]). In order to keep the nitrate concentration of drinking water at an acceptable level, the transport of the nitrate with the groundwater flow has to be understood. It is often reasonable to assume that the solute does not change the properties of the water in which it is dissolved. Should the water properties remain unchanged, the concentration of solute is modeled by a mass conservation equation:

$$\frac{\partial c}{\partial t} + \vec{\nabla} \cdot \vec{J} = s, \tag{2.11}$$

where c [$\mathrm{M\,L^3}$] is the solute concentration, J [$\mathrm{M\,L^{-2}\,T^{-1}}$] is the mass flux, and s again stands for sinks and sources. The mass flux is caused by two mechanisms. Solute is transported advectively (1) with the flow field of the water $\vec{q}$. As we are in the unsaturated zone, the Darcy's velocity $\vec{q}$ has to be expressed as presented in equations 2.8 and 2.9, where relative permeability (k_r) is also included. In addition to that, the solute diffuses (2) in the water. The diffusive flux is proportional to the concentration gradient. The mass flux is thus:

$$\vec{J} = \vec{v}c - D\vec{\nabla}c, \tag{2.12}$$

where D [$\mathrm{L^2\,T^{-1}}$] is the diffusion coefficient. In water, D is typically of the order of $10^{-9}\,\mathrm{m^2/s}$. Combining the equations 2.4, 2.11 and 2.12, the transport equation for the solute reads:

$$\frac{\partial c}{\partial t} + \frac{\vec{q}}{\phi} \cdot \vec{\nabla}c - \vec{\nabla} \cdot D\vec{\nabla}c = s. \tag{2.13}$$

2.4 Heterogeneous materials and soil structure

Flow and transport in the subsurface is scale dependent, as different forces are predominant on different length scales. The scale dependence is also strongly related to the length scales of heterogeneities of the material properties (see Neuweiler [51]).

The soil, which is important for the infiltration of water into the subsurface, can have small vertical extensions, such as several meters. An oil reservoir

which is exploited can extend over kilometers. A gravel aquifer has a structure which is mainly determined by the gravels and the filling material in between. Such a structure can be isotropic. A reservoir in a very deep formation typically has a layered structure which is not necessarily horizontally oriented. Such a medium is highly anisotropic. The structures in an aquifer may be represented as a background material including loamy lenses. The lenses can be represented as ellipsoidal. A fractured rock can be represented as impermeable rock with highly permeable inclusions, which represent the fractures. The inclusions are then better represented as needles or disks.

A heterogeneous porous medium can be considered a composite of different materials. The medium consists of different composites which have clear interfaces, and the properties in one phase are constant. However, the properties of the medium may change continuously, so that no interfaces can be defined. Thus, the heterogeneous distribution of the material properties is characterized by typical length scales. If, for example, a medium is composed of two different materials, one of them being the background while the other one forms an isolated inclusion, a length scale for the heterogeneity would be the typical length scale of an inclusion. In a layered medium, the typical length scale of the heterogeneity is a typical layer thickness. A medium can be considered macroscopically homogeneous if there is one typical length scale of heterogeneities which is much smaller than the typical length scale of the medium itself. It is, however, often also the case that there is not one typical length scale of heterogeneities. Structures exist on a large variety of length scales, often up to that of the medium itself.

2.5 Upscaling and basic ideas of the homogenization theory

By performing upscaling, the homogeneous description of an equivalent macroscopic phenomenon is derived. Therefore, upscaling could be considered as transition between scales, where scale could be e.g. length or time scale. In order to address the questions of connected parameter fields, the homogenization theory [31] is used in this study as it allows to characterize the heterogeneities on different ways.

The homogenization theory is based on an expansion in terms of the typical spatial length scales in the porous medium. The following assumptions have to be made:

- The medium is periodic. Hence, there is a typical microscopic length scale ℓ for the heterogeneous structure, which is the length scale of the unit cell of the periodic field. It is set in relation to the typical macroscopic length scale L of the medium or domain itself (see Figure 2.2).

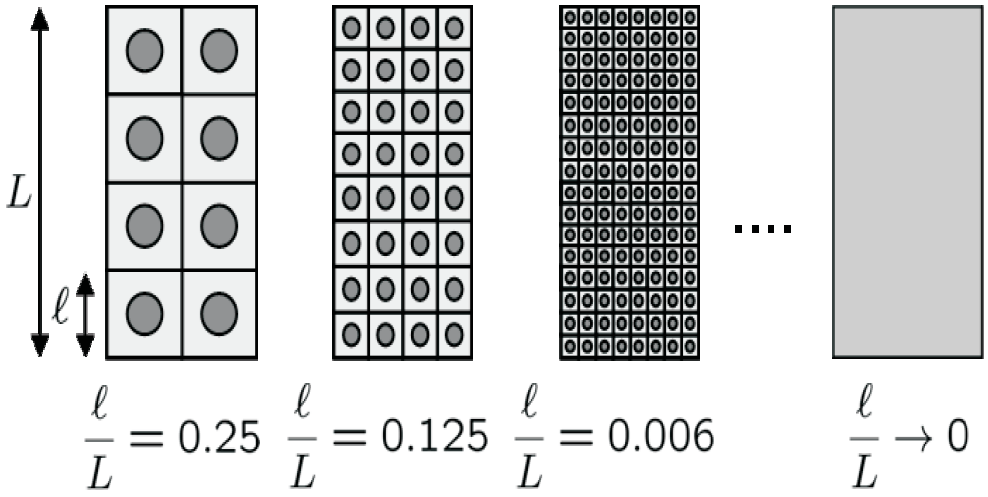

Figure 2.2 Basic idea of homogenization theory.

- The length scales ℓ and L of the medium are clearly separated ($\ell \ll L$) and there are no typical length scales of the parameter field between ℓ and L. The ratio of the microscopic and the macroscopic scale is noted as $\varepsilon = l/L$.

- The scale separation (micro and macro scale) is valid also for a solution and not only for the parameter field.

The basic idea of homogenization theory is described by looking at the limit when the ratio between two length scales ϵ tends to zero. Then the periodic heterogeneous medium appears more and more homogeneous (see Figure 2.2).

2.6 Upscaled form of Richards equation derived by homogenization theory

Here, for notational convenience, a non-dimensional form of Richard's equation [53] was used:

$$\frac{\partial \Theta_{\mathrm{w}}}{\partial t} + T\frac{K_{\mathrm{g}}}{L}\vec{\nabla}\left[\kappa\, k_{\mathrm{r}}\left(h_{\mathrm{c}}\right)\left(\frac{H}{L}\vec{\nabla}h_{\mathrm{c}} + \vec{e}_{\mathrm{z}}\right)\right] = 0, \tag{2.14}$$

where T is a characteristic time scale chosen as $T = L^2\left(K_{\mathrm{g}}H\right)^{-1}$, L is the characteristic length scale, K_{g} is the geometric mean of saturated hydraulic conductivity, H is the characteristic pressure head and $\kappa = KK_{\mathrm{g}}^{-1}$ is the dimensionless saturated conductivity. Typical values have to be chosen dependent from the system. All variables are from now considered as dimensionless.

The assumption of scale separation allows the space variable to be treated as two independent dimensionless variables (x and y). The first is obtained by normalizing the space variable X with the length scale L, the second one by normalizing it with the length scale ℓ:

$$x = \frac{X}{L}, \quad y = \frac{X}{\ell}. \tag{2.15}$$

Note that due to scale separation the relation between two scales is $x = \varepsilon y$. However, as the variables x and y are treated independently, the gradient has to be split into a derivative with respect to x and into a derivative with respect to y. As the base variable would here be x, the derivative with respect to y has to be scaled accordingly

$$\frac{1}{L}\nabla_{\mathrm{X}} = \nabla_{\mathrm{x}} + \frac{1}{\varepsilon}\nabla_{\mathrm{y}}. \tag{2.16}$$

On the basis of the assumptions mentioned above, an upscaled model of Richards equation is derived by expanding the capillary head in terms of the scale parameter ε:

$$h_{\mathrm{c}} = h_{\mathrm{c}}^{(0)} + \varepsilon h_{\mathrm{c}}^{(1)} + \varepsilon^2 h_{\mathrm{c}}^{(2)} + \dots. \tag{2.17}$$

According to this expansion, the Richards equation (equation 2.10) contains terms of different orders ε^n (see equation 2.18). As mentioned, in the limit when the scale parameter ε goes to zero, $\varepsilon \to 0$, the medium appears homogeneous (see Figure 2.2). The upscaled model is derived by considering the Richards equations at this limit. Due to the assumption of scale separation, the remaining terms of different orders ε^n (in this case $n = -2, -1, 0$) are solved independently of each other. That is, the Richards equation is split into a coupled system of equations for different orders ε^n. The final upscaled model is the equation collecting all terms of order ε^0, spatially averaged over the unit cell.

$$\begin{aligned}
&\tfrac{\partial}{\partial t}\left(\Theta^{(0)} + \varepsilon\Theta^{(1)} + \varepsilon^2\Theta^{(2)} + ...\right) + \\
&\left(\vec{\nabla}_x + \tfrac{1}{\varepsilon}\vec{\nabla}_y\right) \cdot \left[\kappa\left(k_{\mathrm{r}}^{(0)} + \varepsilon k_{\mathrm{r}}^{(1)} + \varepsilon^2 k_{\mathrm{r}}^{(2)} + ...\right) \cdot \right. \\
&\left.\left(\left(\vec{\nabla}_x + \tfrac{1}{\varepsilon}\vec{\nabla}_y\right)\left(h_{\mathrm{c}}^{(0)} + \varepsilon h_{\mathrm{c}}^{(1)} + \varepsilon^2 h_{\mathrm{c}}^{(2)} + ...\right) + \tfrac{L}{H}\vec{e}_{\mathrm{z}}\right)\right] \\
&= 0
\end{aligned} \tag{2.18}$$

2.6.1 Dimensionless numbers

For the sake of sorting different orders ε^n, the model is restricted to a specified flow regime, quantified by dimensionless numbers. The Richards equation has

two dimensionless groups:

$$X_1 = \frac{K_g H T}{L^2} \text{ and } \quad X_2 = \frac{H}{L}, \tag{2.19}$$

where T is a characteristic time scale, L the characteristic macroscopic length scale, K_g the geometric mean of saturated hydraulic conductivity and H a characteristic capillary pressure head. The choice of the dimensionless numbers is crucial as a different order of numbers or other model parameters would lead to different upscaled equations [46].

Capillary equilibrium

Here it is assumed that both numbers are in the range of ε^0:

$$\varepsilon^{-1} \ll X_1 \ll \varepsilon^1, \quad \varepsilon^{-1} \ll X_2 \ll \varepsilon^1. \tag{2.20}$$

This assumption leads to the capillary equilibrium. From a physical point of view, this means (1) the typical time scale is slow, as it is associated with the macroscopic length scale L, and (2) the flow is capillary dominated, as the typical capillary pressure head is in the range of the macroscopic length scale.

It is also necessary to quantify the parameter contrast between different materials. In order to obtain equilibrium in the system, here it is assumed that parameter contrasts are in the range ε^0 (small parameter contrast).

For the case that the non-equilibrium effects are considered, it is assumed that the characteristic values of the soil parameters are very contrasted. In particular, it could be assumed that the parameter contrasts between two different materials are in the range of ε^2 (large parameter contrast).

Dependent from the choice of the dimensionless numbers X_1 and X_2 as well as different contrasts between parameters, different upscaled models can be derived.

2.6.2 Upscaled model of Richards equation for capillary equilibrium

Small parameter contrast: With the dimensionless numbers (X_1 and X_2) given above, an upscaled model for small parameter contrast (equilibrium) of the Richards equation can be derived by collecting all terms of order ε^0 and averaging them over the unit cell. In order to obtain a solution, the equations of order ε^{-2} and ε^{-1} also have to be solved. The result can be summarized as follows:

- The first term in the expansion of the capillary head, $h_c^{(0)}$, is independent of the microscopic length scale variable Y. That means it is constant over the unit cell for a given time. This corresponds to a macroscopic capillary equilibrium condition as, e.g., used by Kueper and McWorther [41] or Pickup and Stephen [59].

- The equation for ε^0 yields after volume-averaging over the periodic unit cell:

$$\frac{\partial \Theta_{\text{eff}}(h_{\text{c}}^{(0)})}{\partial t} + \vec{\nabla} \cdot K_{\text{eff}}\left(h_{\text{c}}^{(0)}\right)\left(\vec{\nabla} h_{\text{c}}^{(0)} + e_{\text{z}}\right) = 0, \tag{2.21}$$

  where Θ_{eff} is the upscaled effective water content and K_{eff} is the upscaled effective conductivity.

Large parameter contrast: With the same dimensionless numbers (X_1 and X_2), but in case of large parameter contrast (non-equilibrium) the macroscopic flow model for ε^0 is more complicated, having additional sink/source term:

$$\frac{\partial \Theta_{\text{back}}(h_{\text{c}}^{(0)})}{\partial t} + \vec{\nabla} \cdot K_{\text{back}}\left(h_{\text{c}}^{(0)}\right)\left(\vec{\nabla} h_{\text{c}}^{(0)} + e_{\text{z}}\right) + \langle \frac{\partial \Theta_{\text{incl}}(h_{\text{c}}^{(0)})}{\partial t} \rangle = 0, \tag{2.22}$$

where:

$$\langle \frac{\partial \Theta_{\text{incl}}(h_{\text{c}}^{(0)})}{\partial t} \rangle = \frac{1}{|\Omega|} \int\limits_{\Omega_{\text{incl}}} \frac{\partial \Theta_{\text{incl}}^{(0)}}{\partial t} d\Omega. \tag{2.23}$$

Effective parameters Θ_{back} as well as K_{back} include only background material. The inclusions are not included in those effective parameters. They are included through the additional sink/source term, which comes from the interaction between two different materials. This term is non-linear and requires the solution of the local boundary value problem over the inclusion material. It causes retardation or tailing of the water flux. Θ_{incl} is the effective water content in the inclusions. A more detailed derivation of the non-equilibrium model could be found in Lewandowska et al. [46]. The same type of the problem was also obtained by Hornung [30], using slightly different mathematical methodology.

2.6.3 Effective parameters and soil structure

Small parameter contrast: The effective parameters for equation (2.22) have to be determined for a given parameter field. They are derived on the basis of on the result that the pressure head $h_{\text{c}}^{(0)}$ is constant on the small scale. The water content $\Theta^{(0)}$ and total hydraulic conductivity $K_{\text{u}}^{(0)}$ are functions of $h_{\text{c}}^{(0)}$ in the unit cell. Therefore, they are not constant on the small scale, but fixed for a given value of $h_{\text{c}}^{(0)}$.

The **effective retention function** $\Theta_{\text{eff}}\left(h_{\text{c}}^{(0)}\right)$ is obtained by volume-averaging $\Theta^{(0)}\left(h_{\text{c}}^{(0)}, y\right)$ over the local coordinate y, repeated for all values of $h_{\text{c}}^{(0)}$. For a medium composed of two materials, $\Theta_{\text{eff}}(h_{\text{c}}^{(0)})$ is:

$$\Theta_{\text{eff}}(h_{\text{c}}^{(0)}) = \Phi_1\Theta_1(h_{\text{c}}^{(0)}) + \Phi_2\Theta_2(h_{\text{c}}^{(0)}), \tag{2.24}$$

where Φ_1 and Φ_2 are volume percentages of the materials.

In order to obtain the **effective conductivity** $K_{\text{eff}}\left(h_{\text{c}}^{(0)}\right)$ for a given value of $h_{\text{c}}^{(0)}$, a unit pressure gradient I_1 in x_1 direction and periodic boundary conditions are applied to the unit cell. Then, the total fluxes (Q_{x_1} and Q_{x_2}) through the cell in directions x_1 and x_2 are evaluated. The ratio of the fluxes over the pressure gradient defines the first two elements $K_{\text{eff},11}$ and $K_{\text{eff},12}$ of the effective conductivity tensor. For the other two elements, the same procedure is performed using a unit gradient in x_2-direction. The extension to 3D is straightforward. Repeating the above formalism for different values of $h_{\text{c}}^{(0)}$, the effective relative permeability-saturation curve is obtained. This means the calculation of the effective conductivity for a two-phase flow problem is reduced to the repeated calculation of the effective conductivity for a single phase flow problem, using the unsaturated conductivity for given values of $h_{\text{c}}^{(0)}$.

Large parameter contrast: In case of large parameter contrast, the derivation is the straight forward as in a case of small parameter contrasts, but the inclusions are treated as impermeable obstacles (see equation 2.22).

2.6.4 Information about soil structure and estimation of effective parameters

An upscaled model of the Richards equation can be derived as outlined above if the structure of the parameter field is known in detail. This is usually not the case in practice and the effective parameters have to be estimated based on much less information. For example, only an estimation of the volume percentages of different materials in a soil may be available. Also, the only information about the soil structure may be that one of the materials in the soil is connected throughout the medium. In such cases, the effective retention function (2.24) can be calculated based on the information about the volume percentage of materials only. The effective hydraulic conductivity K_{eff}, however, has to be estimated. One method that might be applied in such cases is the effective medium theory [77].

In this work, an estimation of the $K_{\text{eff}} - S$ relationship (effective conductivity-saturation relationship) based on the volume percentage of the inclusion material using the Maxwell and the self-consistent approach (e.g., [77]) was tested. Both approaches are mean-field approximations.

Maxwell approach: The Maxwell approach is an approximation which is easy to handle in order to calculate effective permeability. The approach is best illustrated by a heterogeneous medium composed of one background material with permeability K_1 and inclusions of some inclusion material with permeability K_2. A sphere of radius R_0 of this heterogeneous material is here considered, which is embedded into pure background material. This picture is compared to a sphere of (unknown) effective permeability material of radius R_0, which is also embedded into the background material (see Figure 2.3).

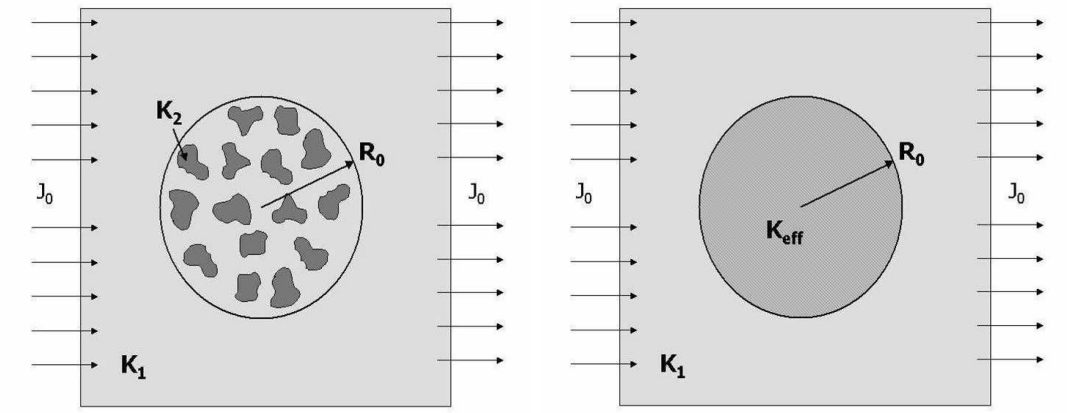

Figure 2.3 Basic principal of the Maxwell approach (Neuweiler [52]).

The perturbations ΔP and $\Delta \vec{J}$ caused to the pressure and the pressure gradient field outside of the spheres due to each of the spheres are compared. The effective permeability is obtained by the demand, that these perturbations have to be equal to each other.

The perturbation field due to the heterogeneous material cannot be calculated since only analytical solutions for spherical inclusions exist and not for an arbitrary structure. Also, the inclusions interact in their influence of the external flow field. Therefore, to get an approximate solution the medium illustrated on the left of Figure 2.3 is simplified using the following assumptions:

- It is assumed that the inclusions are all identical. They are approximated by spheres with radius r_0. If the large sphere of radius R_0 has N inclusions, the volume percentage of inclusions is $\Phi = Nr_0/R_0$ (see Figure 2.4).

- The influence of all inclusions is approximated as the sum of the influence of each single inclusion. This is a severe approximation, as it means we neglect the interaction of the inclusions completely. Clearly this assumption becomes questionable when the volume percentage of the inclusion becomes large.

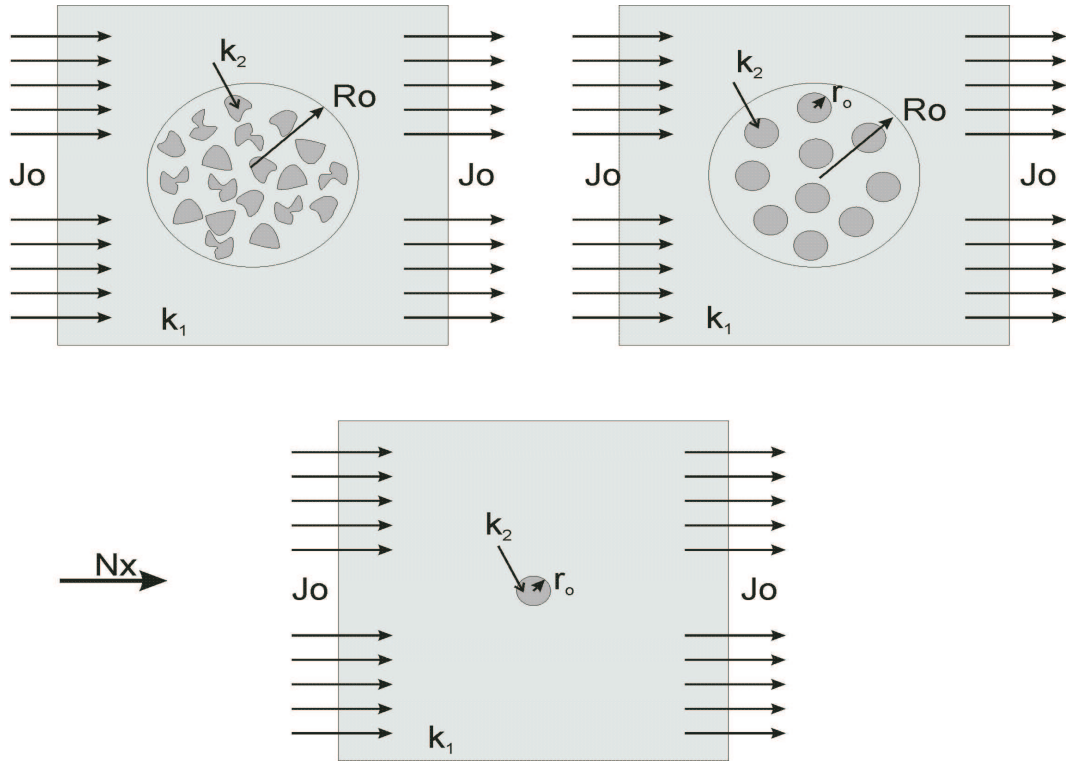

Figure 2.4 Scheme of the simplification in order to calculate the perturbation to the external field caused by the heterogeneous sphere (Neuweiler [52]).

- The sum of the influence of all inclusions is approximated as the sum of the inclusions which are all shifted to the center of the coordinate system.

After equalizing ΔP and $\Delta \vec{J}$, the effective conductivity estimated with the Maxwell approach for for the general (d-dimensional) case and M inclusion materials is:

$$\frac{K_1 - K_{\text{eff}}}{(d-1)\,K_1 + K_{\text{eff}}} = \sum_{\text{i}=1}^{\text{M}} \Phi_{\text{i}} \frac{K_1 - K_2}{(d-1)\,K_1 + K_2}, \tag{2.25}$$

where Φ_{i} is the volume percentage of the inclusion material. The Maxwell approach is appropriate for media with a clear background-inclusion structure (see Figure 2.3).

Self-consisted approach: The heterogeneous material is assumed to be a composite, but there is no background and inclusion material, but both materials are taken into account symmetrically. This means, the medium is made of different patches of the materials (see Figure 2.5). It is assumed, that it can be replaced

by a homogeneous medium with effective permeability. The pressure field (or the pressure gradient field) in the effective homogeneous medium will be analyzed.

The heterogeneous medium in the sketch is periodic, which is not the case in general. The two media are compared in the way, that one by one each patch of the heterogeneous material is placed into the effective homogeneous material. The inclusions of one patch into the effective material will cause a perturbation in the field of the effective material.

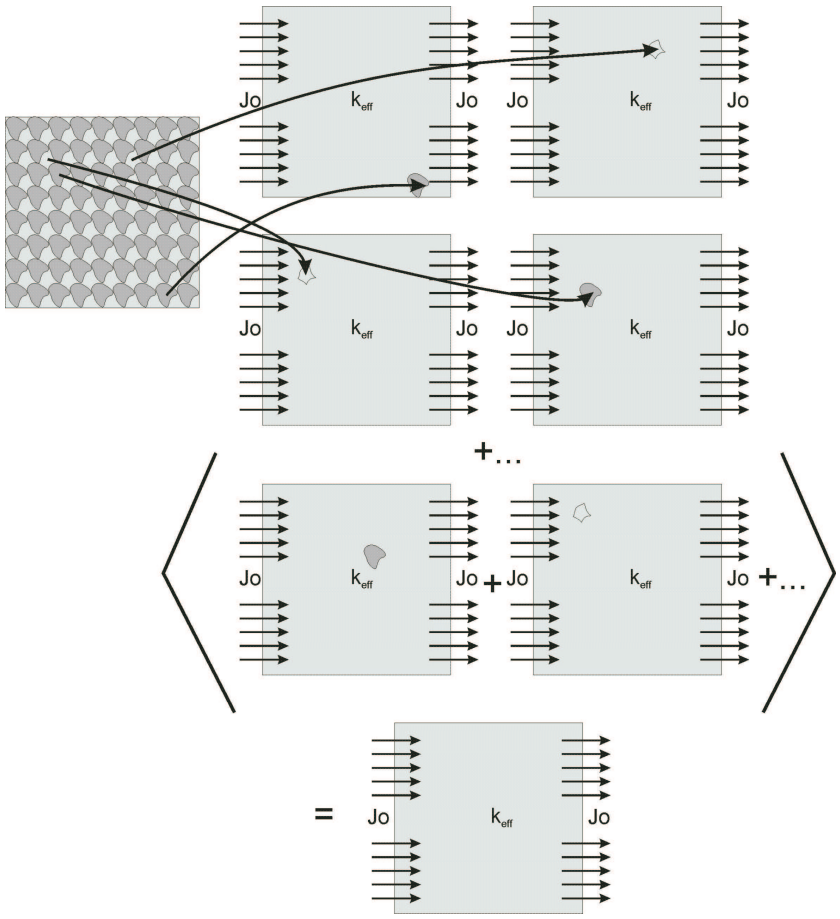

Figure 2.5 Basic principal of the self-consistent approach (Neuweiler [52]).

In the self-consistent approximation the effective permeability is obtained by the requirement, that the perturbations caused by all the included patches into the effective material have to cancel. This will lead to an implicit approach. Clearly, it is not possible to calculate the perturbation of an arbitrary patch analytically. Therefore, similarly to the Maxwell approach, approximations are necessary.

- Each patch is approximated by a sphere with radius R_0 (see Figure 2.6).

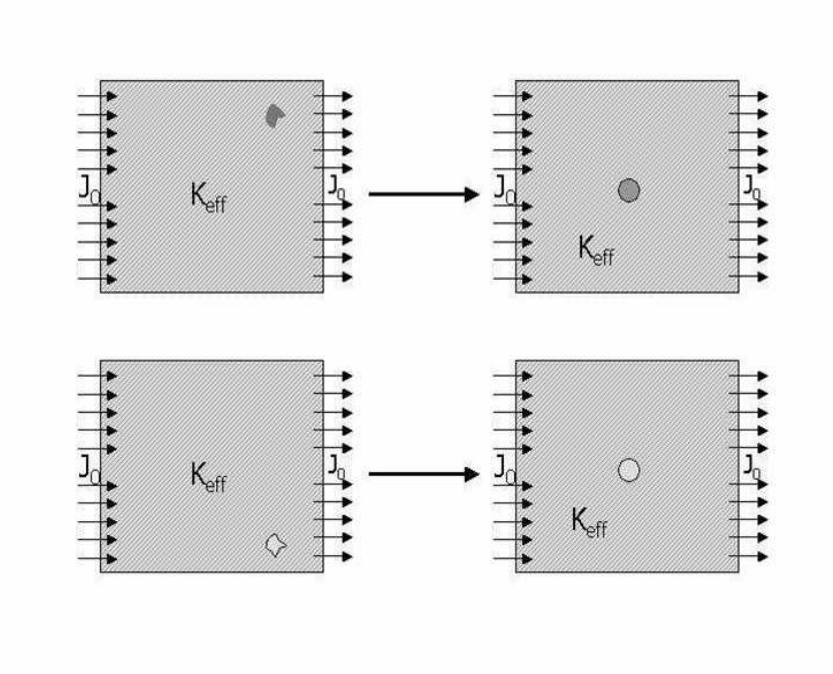

Figure 2.6 Simplification made in self-consistent approach (Neuweiler [52]).

- The average of the fluctuations of all patches is approximated as the sum of the fluctuations caused by each single patch, which is shifted to the center of the coordinate system. That means that we again neglect all interactions of the inclusions.

The effective permeability is obtained by the requirement, that the averaged fluctuation of all inclusions into the effective homogeneous material has to vanish. The general implicit equation for the effective permeability for the d dimensional problem, where a medium is composed of M phases, is

$$\sum_{\mathrm{i}=1}^{\mathrm{M}} \Phi_{\mathrm{i}} \frac{K_{\mathrm{eff}} - K_{\mathrm{i}}}{(d-1)\, K_{\mathrm{eff}} + K_{\mathrm{i}}} = 0. \tag{2.26}$$

The self-consistent approach is appropriate for media without a distinction between background and inclusion (see Figure 2.5).

2.7 Upscaled form of transport equation using homogenization theory

The upscaled form of the transport equation is derived here using the same homogenization approach as in the case of flow. In order to be able to derive the

upscaled transport equation a non-dimensional form of the transport equation (equation 2.11) for a steady state has been used:

$$\frac{L^2}{TD}\Theta\left(\vec{x}\right)\frac{\partial c}{\partial t}+\vec{\nabla}\cdot\left(\frac{LU}{D\bar{\Theta}}\vec{v}\left(\vec{x}\right)c-\Theta\left(\vec{x}\right)\vec{\nabla}c\right)=0, \tag{2.27}$$

where L is the characteristic length $[L]$, T characteristic time $[T]$, U characteristic velocity $[L\,T^{-1}]$, $\bar{\Theta}$ characteristic water content [-] and D $[L^2\,T^{-1}]$ characteristic dispersion coefficient. All variables from now are considered as dimensionless.

Here two dimensionless groups could be distinguished:

$$\frac{L^2}{TD}=N_{\mathrm{f}}\ \text{ and }\ \frac{LU}{D\bar{\Theta}}=P_{\mathrm{e}}. \tag{2.28}$$

The first number N_{f} compares the typical time scale related to the macroscopic length L to typical macroscopic dispersive time scale. The second one P_{e} is a typical Peclet number showing the relation between advection and dispersion in the system for the large length scale.

Here, as in the case of upscaled Richards equation the assumption of periodicity of domain is assumed (Figure 2.7). Therefore, background and inclusion domains could be distinguished and the dimensional numbers for both domains: Pe_{back}, Pe_{incl}, $N_{\mathrm{f,\,back}}$, $N_{\mathrm{f,\,incl}}$ can be identified, where subscript "incl" is used for inclusions and "back" for background material (see Figure 2.7). Also, concentrations in the two domains could be distinguished: c_{back}, c_{incl}.

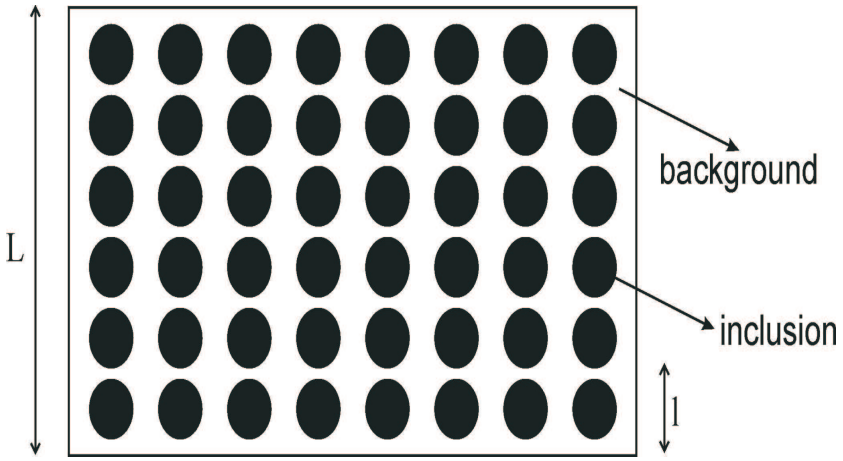

Figure 2.7 Periodic domain and length scales used in derivation of upscaled transport model.

Those two domains are associated to two different time scales T and τ, where T is typical time scale on large length scale and τ typical time scale on small length

scale. The time scale on the large length scale L is dominated by background material, whereas the time scale on the small length scale l is dominated by the inclusions.

Comparing those typical time scales T and τ, three different cases could be distinguished. First, if T is much larger than τ, we would have equilibrium conditions as the processes in inclusions are happening at much faster scale than in background. If T is much smaller than τ, the inclusions are not seen at all and therefore, only background matters. This situation again would lead to an equilibrium conditions. The third case is when T and τ are comparable. The last configuration would lead to non-equilibrium conditions. One possible configuration for such a situation is that advection dominates on the large scale and diffusion (dispersion) dominates on the small scale. This non-equilibrium could be caused by large parameter contracts.

Upscaled models of transport for equilibrium and non-equilibrium conditions will be presented in the following. In case of both upscaled models homogenization theory has been here applied in order to derive them. As in the case of flow, the assumption of scale separation allows the space variable to be treated as two independent variables (x and y). Concentration c in terms of the scale parameter ε has been expanded (equation 2.29) in the transport equation (equation 2.27).

$$c = c^{(0)} + \varepsilon c^{(1)} + \varepsilon^2 c^{(2)}. \tag{2.29}$$

As we have two domains (background and inclusions), two transport equations have to be written. One for the background domain:

$$\begin{aligned}
&\frac{1}{\varepsilon}\Theta_{\text{back}}\left(\vec{y}\right)\frac{\partial}{\partial t}\left(c^{(0)}_{\text{back}} + \varepsilon c^{(1)}_{\text{back}} + \varepsilon^2 c^{(2)}_{\text{back}} + \ldots\right) + \left(\vec{\nabla}_x + \tfrac{1}{\varepsilon}\vec{\nabla}_y\right)\cdot \\
&\Bigg[\frac{1}{\varepsilon}\vec{v}_{\text{back}}\left(\vec{y}\right)\left(c^{(0)}_{\text{back}} + \varepsilon c^{(1)}_{\text{back}} + \varepsilon^2 c^{(2)}_{\text{back}} + ...\right) - \\
&\Theta_{\text{back}}\left(\vec{y}\right)\left(\vec{\nabla}_x + \tfrac{1}{\varepsilon}\vec{\nabla}_y\right)\left(c^{(0)}_{\text{back}} + \varepsilon c^{(1)}_{\text{back}} + \varepsilon^2 c^{(2)}_{\text{back}} + \ldots\right)\Bigg] = 0
\end{aligned} \tag{2.30}$$

and one for inclusions:

$$\begin{aligned}
&\frac{1}{\varepsilon^2}\Theta_{\text{incl}}\left(\vec{y}\right)\frac{\partial}{\partial t}\left(c^{(0)} + \varepsilon c^{(1)}_{\text{incl}} + \varepsilon^2 c^{(2)}_{\text{incl}} + \ldots\right) + \left(\vec{\nabla}_x + \tfrac{1}{\varepsilon}\vec{\nabla}_y\right)\cdot \\
&\Bigg[\vec{v}_{\text{incl}}\left(\vec{y}\right)\left(c^{(0)}_{\text{incl}} + \varepsilon c^{(1)}_{\text{incl}} + \varepsilon^2 c^{(2)}_{\text{incl}} + ...\right) - \\
&\Theta_{\text{incl}}\left(\vec{y}\right)\left(\vec{\nabla}_x + \tfrac{1}{\varepsilon}\vec{\nabla}_y\right)\left(c^{(0)}_{\text{incl}} + \varepsilon c^{(1)}_{\text{incl}} + \varepsilon^2 c^{(2)}_{\text{incl}} + \ldots\right)\Bigg] = 0.
\end{aligned} \tag{2.31}$$

At the interfaces between domains, concentrations (equation 2.32) as well as flux (equation 2.33) have to be continues:

$$c^{(0)}_{\text{back}} + \varepsilon c^{(1)}_{\text{back}} + \varepsilon^2 c^{(2)}_{\text{back}} + \ldots = c^{(0)}_{\text{incl}} + \varepsilon c^{(1)}_{\text{incl}} + \varepsilon^2 c^{(2)}_{\text{incl}} + \ldots \tag{2.32}$$

$$\begin{aligned}
&U_{\text{back}}\vec{v}_{\text{back}} \left(c^{(0)}_{\text{back}} + \varepsilon c^{(1)}_{\text{back}} + \varepsilon^2 c^{(2)}_{\text{back}} + \ldots \right) - \\
&\frac{D_{\text{back}}\bar{\Theta}_{\text{back}}}{L}\Theta_{\text{back}}\left(\vec{y}\right) \left(\vec{\nabla}_x + \tfrac{1}{\varepsilon}\vec{\nabla}_y \right) \left(c^{(0)}_{\text{back}} + \varepsilon c^{(1)}_{\text{back}} + \varepsilon^2 c^{(2)}_{\text{back}} + \ldots \right) = \\
&U_{\text{incl}}\vec{v}_{\text{incl}} \left(c^{(0)}_{\text{incl}} + \varepsilon c^{(1)}_{\text{incl}} + \varepsilon^2 c^{(2)}_{\text{incl}} + \ldots \right) - \\
&\frac{D_{\text{incl}}\bar{\Theta}_{\text{incl}}}{L}\Theta_{\text{incl}}\left(\vec{y}\right) \left(\vec{\nabla}_x + \tfrac{1}{\varepsilon}\vec{\nabla}_y \right) \left(c^{(0)}_{\text{back}} + \varepsilon c^{(1)}_{\text{incl}} + \varepsilon^2 c^{(2)}_{\text{incl}} + \ldots \right) = 0.
\end{aligned} \tag{2.33}$$

The expanded equations (2.30, 2.31, 2.32 and 2.33) contains terms of different orders ε^n. As mentioned, in the limit when the scale parameter ε goes to zero, $\varepsilon \to 0$, the medium appears homogeneous (see Figure 2.2). The upscaled model is derived by considering the transport equations at this limit. Due to the assumption of scale separation, the remaining terms of different orders ε^n are solved independently of each other. That is, the transport equation is split into a coupled system of equations for different orders ε^n and solved separately.

2.7.1 Upscaled models in case of small (equilibrium) and large (non-equilibrium) parameter contrasts

Dimensionless numbers

Large parameter contrast: In case of non-equilibrium the processes in the background material are advection dominated, whereas on the smaller scale diffusion dominates. For the background material a Peclet number of order $Pe_{\text{back}} \approx \varepsilon^{-1}$ has been chosen, which means that advection dominates over diffusion on the large scale. Therefore,

$$Pe_{\text{back}} = N_{\text{f, back}} = \frac{LU_{\text{back}}}{D_{\text{back}}\bar{\Theta}_{\text{back}}} \approx \varepsilon^{-1}. \tag{2.34}$$

In case of non-equilibrium, time scales T and τ have to be comparable. The condition for time scales reads,

$$\tau = \frac{l^2}{D_{\text{incl}}} \approx T = \frac{L\bar{\Theta}_{\text{back}}}{U_{\text{back}}}. \tag{2.35}$$

This configuration would lead to the following dimensionless numbers on the small scale in order to fulfill the condition from equation 2.35

$$Pe_{\text{incl}} = \frac{LU_{\text{incl}}}{D_{\text{incl}}\bar{\Theta}_{\text{incl}}} \approx \varepsilon^0 \quad N_{\text{f, incl}} = \frac{L^2}{TD_{\text{incl}}} = \varepsilon^{-2}\frac{l^2}{TD_{\text{incl}}} \approx \varepsilon^{-2}. \tag{2.36}$$

If the ratio between dimensionless numbers of different materials is taken ($N_{\text{f, incl}}/N_{\text{f, back}}$ and $Pe_{\text{incl}}/Pe_{\text{back}}$) following contrasts between materials are required in order to obtain a non-equilibrium condition in the system

$$\frac{N_{\text{f, incl}}}{N_{\text{f, back}}} = \frac{D_{\text{incl}}}{D_{\text{back}}} = \varepsilon \quad \frac{Pe_{\text{incl}}}{Pe_{\text{back}}} = \frac{U_{\text{incl}}\Phi_{\text{back}}D_{\text{back}}}{U_{\text{back}}\Phi_{\text{incl}}D_{\text{incl}}} = \varepsilon^1 \rightarrow \frac{U_{\text{incl}}\Phi_{\text{back}}}{U_{\text{back}}\Phi_{\text{incl}}} = \varepsilon^2 \tag{2.37}$$

This situation is possible since dispersion (diffusion) depends on tortuosity and could differ much in inclusions if they are much drier than the background material. Furthermore, the filter velocity in the inclusions has to be much smaller than in the background and represent the stagnant zones ($U_{\text{incl}} << U_{\text{back}}$). This is also possible since dry inclusion close to its residual saturation could hardly conduct any water (e.g. $U_{\text{incl}}/U_{\text{back}} \approx \varepsilon^3$), whereas background wet material is still conductive.

Small parameter contrast: In case of equilibrium processes on both length scales are dominated by the advection. Therefore, for the same choice of Peclet number at the large length scale ($Pe_{\text{back}} \approx \varepsilon^{-1}$) the ratio between velocities ($U_{\text{incl}}/U_{\text{back}}$) is approximately of order $O(\varepsilon^0)$. Therefore, in the system, there are no stagnant zones as well as the contrast between parameters is smaller than in the previous case.

Upscaled models

Small parameter contrast: In case of equilibrium, the macroscopic model derived using homogenization approach explained above is

$$\begin{aligned} &\Theta_{\text{eff}}\frac{\partial c_{\text{macro}}}{\partial t} + \vec{\nabla}\cdot\left(\vec{v}_{\text{eff}}c_{\text{macro}} - \Theta_{\text{eff}}D_{\text{eff}}\vec{\nabla}c_{\text{macro}}\right) = 0 \\ &c_{\text{macro}} = c_{\text{back}}\Phi_{\text{back}} + c_{\text{incl}}\Phi_{\text{incl}} \end{aligned} \tag{2.38}$$

where Θ_{eff} is effective water content, v_{eff} effective velocity, D_{eff} effective dispersion tensor (see equation 2.39), Φ_{back} volume percentage of background material and Φ_{incl} volume percentage of inclusion material. The effective parameters are obtained as follows (see also section 2.5.3)

$$\begin{aligned} &\Theta_{\text{eff}} = \Theta_{\text{back}}\Phi_{\text{back}} + \Theta_{\text{incl}}\Phi_{\text{incl}}, \\ &\vec{v}_{\text{eff}} = \langle\vec{v}_{\text{back}} + \vec{v}_{\text{incl}}\rangle, \\ &D_{\text{eff}} = D_{\text{diffusion}} + \underbrace{\langle\vec{v}_{\text{back}}(\vec{y})\,\vec{\chi}(\vec{y})\rangle\Phi_{\text{back}}}_{\text{Macrodispersion}}. \end{aligned} \tag{2.39}$$

The vector $\vec{\chi}(\vec{y})$ is the solution of a linear local boundary value problem. The vector field $\vec{\chi}(\vec{y})$ characterizes the micro geometry of the period from the point of view of the transfer of water. In order to solve it the information about the microscopic geometry of the porous medium is required. Except for some particular cases, this problem has to be numerically solved.

Large parameter contrast: As mentioned, in case of non-equilibrium in macroscopic model a large contrast between material properties has been considered (see equation 2.37), such as velocities or dispersion. Also, as in the case of upscaled model for flow, when there is a large parameter contrasts (see section 2.5.2), the effective parameters do not see inclusions, meaning that they are treated as impermeable obstacles. The non-equilibrium macroscopic model could be written as

$$\langle\Theta_{\text{back}}(\vec{y})\rangle_{\Phi_{\text{back}}}\frac{\partial c^{(0)}_{\text{back}}}{\partial t}+\langle\Theta_{\text{back}}(\vec{y})\,\vec{\chi}(\vec{y})\rangle_{\Phi_{\text{back}}}\frac{\partial}{\partial t}\vec{\nabla}_{\text{x}}c^{(0)}_{\text{back}}+\langle\vec{v}_{\text{back}}(\vec{y})\rangle_{\Phi_1}\vec{\nabla}_{\text{x}}c^{(0)}_{\text{back}}-$$
$$\vec{\nabla}_{\text{x}}D_{\text{back}}\langle\Theta_{\text{back}}(\vec{y})\rangle_{\Phi_{\text{back}}}\vec{\nabla}_{\text{x}}c^{(0)}_{\text{back}}-\underbrace{\vec{\nabla}_{\text{x}}\langle\vec{v}_{\text{back}}(\vec{y})\,\vec{\chi}(\vec{y})\rangle_{\Phi_{\text{back}}}\vec{\nabla}_{\text{x}}c^{(0)}_{\text{back}}}_{\text{Macrodispersion}}=\underbrace{\frac{\partial\langle c^{(0)}_{\text{incl}}\rangle_{\Phi_{\text{incl}}}}{\partial t}}_{\text{Source}}. \tag{2.40}$$

where:

$$\frac{\partial\langle c^{(0)}_{\text{incl}}\rangle_{\Phi_{\text{incl}}}}{\partial t}-\langle\vec{\nabla}_{\text{y}}D_{\text{incl}}\Theta_{\text{incl}}(\vec{y})\,\vec{\nabla}_{\text{y}}c^{(0)}_{\text{incl}}\rangle_{\Phi_{\text{incl}}}=0. \tag{2.41}$$

Effective parameters Θ_{back} as well as D_{back} include only background material. Inclusions are not considered in those effective parameters. They are included through additional sink/source term, which comes from the interaction between two different materials. This term causes tailing or retardation of the concentration.

Chapter 3

Experimental and modeling studies of flow: influence of structure and different parameter contrasts on upscaled flow model

In this chapter, the analysis of the structural influence on estimation of effective parameters (Question 1), assessment of assumptions (Question 2) as well as time analysis (Question 3) for **flow upscaled models** will be addressed and illustrated on two experimental examples.

The first example (**Experiment I**) has been focused on flow in the unsaturated zone under equilibrium conditions, meaning that the contrast between the sand properties used in the experiment has been small. Different structures, with significantly different conductivities have been investigated in order to gain a better knowledge of the structural influence on the estimation of effective parameters for the upscaled flow model derived under equilibrium condition (Question 1). The applicability of mentioned upscaled flow model under ideal and non-ideal conditions has also been assessed (Question 2).

The materials used during Experiment I were two sands chosen according to the requirement of small parameter contrast necessary to obtain equilibrium conditions in the sample. In order to observe the structural influences for the estimation of effective parameters, multi-step drainage experiments with two differently packed columns (periodic and random structures) have been performed. Beside the outflow, a spatial water distribution was measured by means of neutron radiography/tomography. Additionally, the applicability of this upscaled model was tested by investigating the influence of violating periodicity assumption in random structure, but also of increase of parameter contrast between used materials as a requirement for equilibrium condition.

The second experimental study (**Experiment II**) was focused on flow in the

unsaturated zone under non-equilibrium. This implies that the parameter contrasts between soil materials in this case were large (see Chapter 2). It has been shown in section 1.2.2 that this kind of process could be modeled by means of non-equilibrium models. However, in order to choose if non-equilibrium models are needed, typical time scales have to be estimated (Question 3). This estimation is not straight forward. Therefore, in this study it was tried to illustrate the different options for estimation of time scales. Here a non-equilibrium configuration by the macroscopic trapping effect due to the reduced permeability of the surrounding material was analyzed with a drainage experiment. The outflow was measured and 3D spatial water distribution during the transient process has been monitored by means of fast neutron tomography. Prior to Experiment II, which has been done in order to map above mentioned trapping effect, the needed time for drainage of two sand inclusions was tried to be estimated based on the time analysis.

All mentioned experiments were performed at the NEUTRA facility at the Paul Scherrer Institute, Villingen [reference: http://neutra.web.psi.ch].

3.1 Experiment I: Multi-step drainage experiments in columns with different structures

3.1.1 General setup of the columns and experiment

Column setup:

The size of the columns used for the multi-step outflow experiments was $10\times10\times20$ cm^3. In order to generate artificial heterogeneity, the columns were packed layer by layer with individual sand cubes of 1 cm^3 ($1\times1\times1$ cm^3) by means of a metal lattice in dry conditions. After each layer, the lattice was slowly pulled upwards to allow sufficient free height for the next layer. In order to avoid preferential flow paths between the cubes, the column was shaken moderately with a sieving machine after each layer had been packed.

The cubes were made of two different sand types. The finer sand had a particle size distribution ranging from 0.08 to 0.2 mm and the coarse sand from 0.1 to 0.5 mm. The percentage of the coarse material in both columns was 32% in order to be close to the percolation threshold for 3D prismatic domains. At this threshold the inclusion material forms a connected cluster in an uncorrelated random field [74].

The first column had a random structure and connected clusters of coarse as well as of fine material, which expanded from the top to the bottom of the column, in accordance with the percolation threshold. The structure had no typical length scale that would be small compared with the size of the column. In the following, this column is referred to as "random structure". By contrast,

the second column has a periodic structure, where the coarse inclusion material is not interconnected but forms isolated structures, while the fine material forms an interconnected background. This column is referred to as "periodic structure". The periodic structure fits to the assumptions made in homogenization theory and to the assumption when estimating the effective parameters with the Maxwell approach. The two columns can be considered opposite extremes in terms of interconnected structures and periodicity. The structures are shown in Figure 3.1.

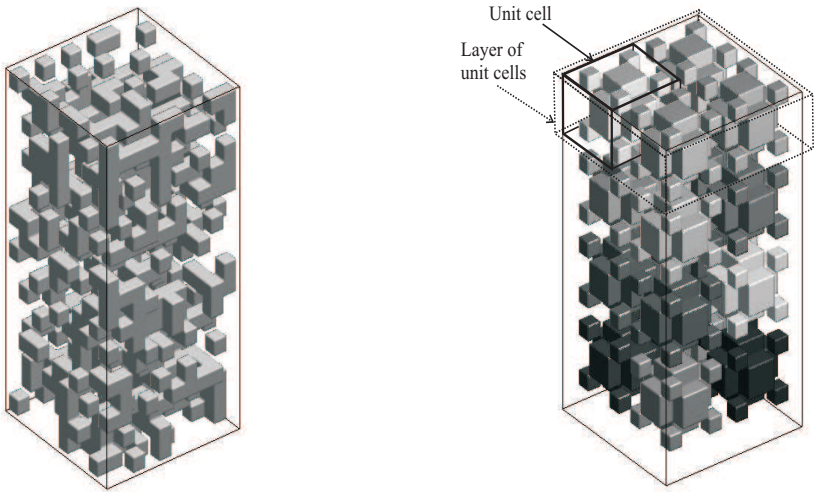

Figure 3.1 Random and periodic structure of the inclusion material in the columns (coarse sand), not to scale

The columns were packed under dry conditions. To ensure complete water saturation, the columns were flushed with 10±2 pore volumes of CO_2 and then covered with aluminium foil in order to minimize air diffusion into the column. Then, the column was slowly flushed with 5 pore volumes of degassed heavy water (D_2O), letting the CO_2 dissolve in the water. Heavy water was used for the sake of reduced neutron attenuation during neutron radiography/tomography. Evaluated from empty, dry and wet mass of the columns, saturations up to 98% were achieved. The gravimetrically determined saturations and porosities with their measurement errors are shown in Table 3.1.

The bottoms of the columns were closed with porous plates covered with fine tissue, which were kept fully water saturated. Previous test experiments showed that this porous plate-tissue system prevents air from entering the column up to a bottom suction of -80 cm. The measured saturated hydraulic conductivity of the porous plates was $K = 3.0 \times 10^{-5} \pm 6.0 \times 10^{-6}$ m/s.

Table 3.1 Initial saturation and porosity of the columns.

Column	Saturation [-]	ϕ [-]
Periodic	0.98 ± 0.0082	0.45 ± 0.0011
Random	0.97 ± 0.0084	0.43 ± 0.0011

Experimental setup:

For each multi-step outflow experiment, the bottom outlet of the column was connected to a water reservoir. The height of the reservoir was adjustable in order to control the bottom boundary condition. It was placed on a balance, so that the cumulative outflow over time could be measured. The reservoir was flat and wide in order to minimize changes in the water level (and hence the bottom boundary condition) during the experiment. The entire experimental setup was installed in the NEUTRA beam line. The balance was monitored by a camera outside the measurement room. All the controls except for the water table adjustment were accessible from outside the chamber.

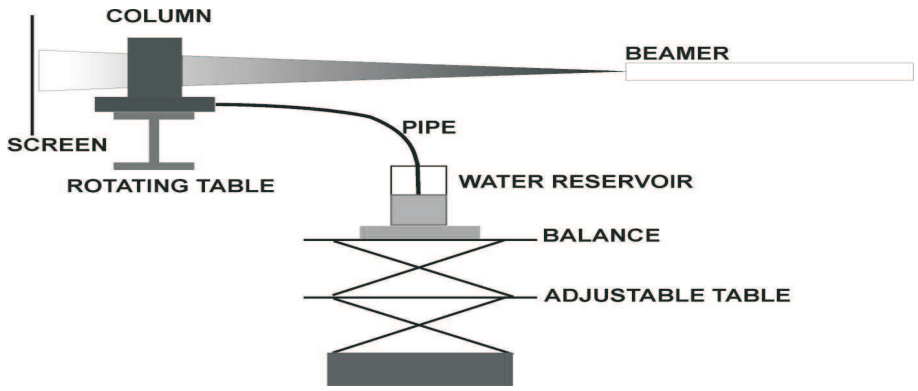

Figure 3.2 Set up of the experiment.

Neutron Radiography and Slow Tomography:

Neutron radiography provides 2D information about the water saturation of a sample, integrated along the horizontal, parallel neutron beam. One 2D measurement for the column takes 20 seconds. Hence, the method is applicable to slow transient drainage processes, which do not significantly change the sample's state of saturation in this time range. Neutron radiography is based on the Lambert-Beer law for attenuation of neutron beam intensity:

$$I = I_0\, exp\left(-\sum_i \alpha_\mathrm{i} d_\mathrm{i}\right), \tag{3.1}$$

where I_0 is the intensity of the neutron beam before passing through the matter, I the intensity of the neutron beam after passing through the matter, α a material-specific attenuation coefficient, d the length that the beam passes through and the index i stands for the individual attenuating materials. In this experiment, these were the aluminum walls of the column, sand and heavy water; air was neglected.

The transmitted neutron beam intensity was measured with a 6Li-scintillator in combination with a CCD camera. The pixel size was 0.272 x 0.272 mm^2, resulting in 772 x 375 pixels for the column.

Tomography provides full 3D images of objects by recording 2D transmission images from many different directions and reconstructing the attenuation coefficients in 3D from its projections. Therefore, the columns were installed on a rotating table. The table rotation is automatically controlled and synchronized with the detector system by the tomography software.

The projections were achieved by rotating the columns in 300 small angular steps over 180°. Details about the inversion process can be found in Kak and Slaney [36]. The 3D resolution of the column was $772 \times 375 \times 375$ voxels. The recording time for a slow tomogram of the sample was around 2 hours. Therefore, it is only applicable for the equilibrium states between the pressure steps of the multi-step drainage experiments.

3.1.2 Image analysis

Fully saturated images (2D radiograms and 3D tomograms) were taken before the multi-step outflow experiments started. After the experiments were finished, the columns were dried in an oven at 90°C for two weeks, and dry images (2D and 3D) were taken. The undisturbed (open-beam), saturated and dry images serve as reference values. Although the attenuation coefficient α of heavy water is known fairly well (e.g., [50]), a better accordance with the water mass measured on the balance was achieved by using the two-point calibration with the wet and dry image as described below (equation 3.2).

Although heavy water was used, which has a smaller attenuation coefficient than normal water, the undisturbed neutron intensity dropped to 0.5% of the initial intensity after passing the saturated sample. This transmission value is expected on the basis of the exponential law of attenuation (equation 3.1). In reality, the intensities reaching the detector are superposed by neutrons that are scattered either in the sample or at the experimental setup. The scattering contribution corresponds to 10% or more of the open beam value and is therefore

far beyond the actual transmission value. For this reason, it is absolutely necessary to correct the raw radiograms by subtracting the scattering contributions (see Figure). The sample scattering is computed on the basis of point scattered functions, while the background scattering is measured behind a non-transparent block. In addition, spectral effects such as beam hardening and the energy dependent detector efficiency must be taken into account (e.g., [25]).

After these corrections for scattering and spectral effects, the pixel-wise saturations S are obtained by:

$$\begin{aligned} \ln \frac{I_1}{I_{\text{dry}}} &= \alpha_{\text{water}} d_{\text{water}} \\ \ln \frac{I_{\text{sat}}}{I_{\text{dry}}} &= \alpha_{\text{water}} d_{\text{water sat}} \\ S = \frac{d_{\text{water}}}{d_{\text{water sat}}} &= \frac{\alpha_{\text{water}}^{-1} (\ln\, I_1 - \ln\, I_{\text{dry}})}{\alpha_{\text{water}}^{-1} (\ln\, I_{\text{sat}} - \ln\, I_{\text{dry}})}, \end{aligned} \tag{3.2}$$

where I_{dry}, I_{sat} and I_1 are the neutron intensities after passing through the dry column, the saturated column and the column at partly saturated conditions, respectively. α_{water} the calibrated attenuation coefficient of heavy water, and $d_{\text{water sat}}$ and d_{water} are the total thicknesses of water in the column at saturated and variably saturated conditions respectively. Note that the computed values of S are independent of α_{water}.

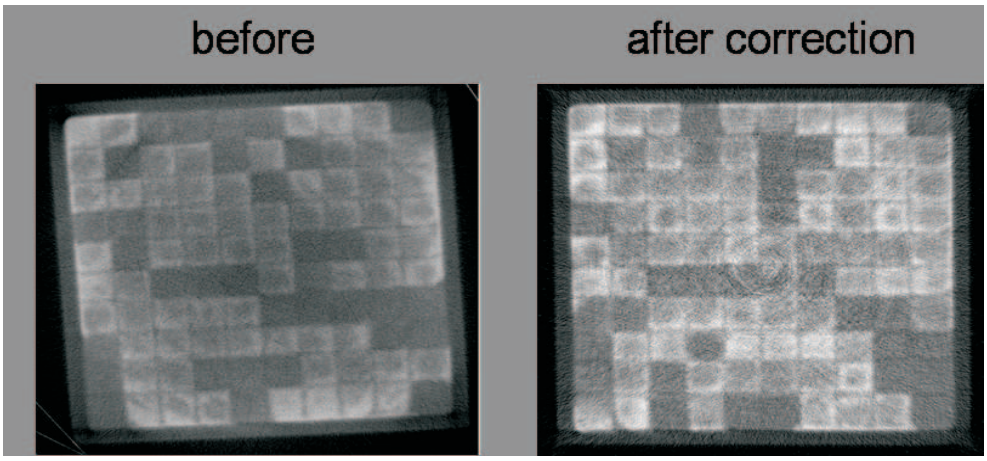

Figure 3.3 Horizontal cross section of the random sand column before and after correction has been performed.

For quality control, the total water masses in the columns at the steady states were computed from the tomograms (equation 3.2) for each time step and compared with the curve of total water mass obtained from weighting the outflow.

The comparison showed a maximum relative error of 5%. From sample statistics of 40 layer averaged saturations at a saturation value of unity, the standard deviation $\sigma_s = 0.02\ (-)$ was evaluated for the error of tomography saturation measurements.

For the later comparison with numerical results, also averaged values for the saturation in each of the individual $1{\times}1{\times}1$ cm^3 sand cubes were computed from the images. In order to identify the edges of the sand cubes in the images, a Gaussian filter with a standard deviation of 1.5 pixels for noise reduction was first applied. Then, the sums of saturations in all pixels parallel to the principal Cartesian axes were computed. For the x-profile, this is:

$$P_x(x) = \sum_{y=0}^{y_{max}} \sum_{z=0}^{z_{max}} |\nabla S(x,y,z)|. \tag{3.3}$$

From the profile P_x, we determine an interface indicator using the morphological operator $EMAX_h$ described by Soille and Talbot [73] that defines the cube edges. With these edges as boundaries for the cubes, the water content could be computed for each cube. Since the cube arrangement is known, the total water content for each sand type can be computed by direct mapping.

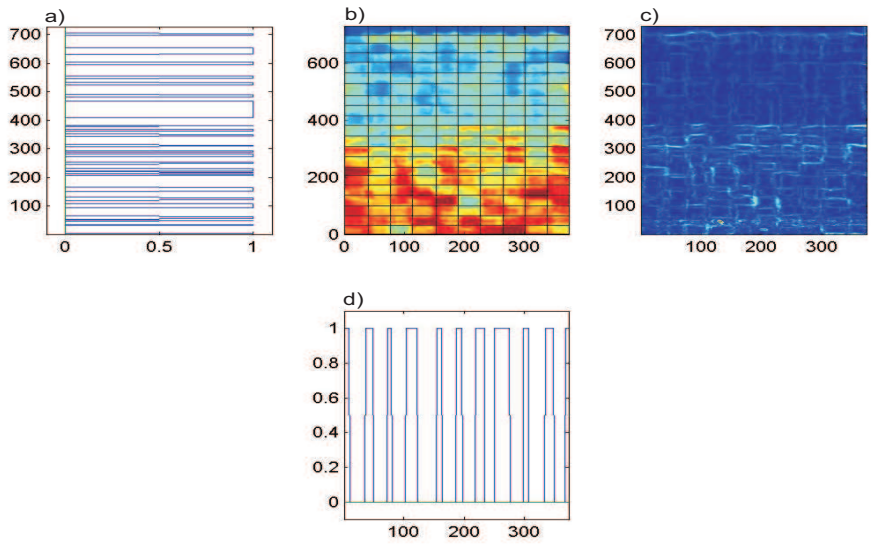

Figure 3.4 Edge determination: a) Local max regions in y-direction, b) defined edges, c) saturation gradient and d) local max regions in x-direction

3.1.3 Experiments and results

Both columns had fixed-pressure (suction) boundary conditions applied at the bottom. At the top, the columns were open to the air at atmospheric pressure. Pressure heads from +20 to -50 cm were applied at the bottom of the column (porous plate) in steps of 10 cm during the multi-step drainage experiment.

During each pressure step, the cumulative mass of the outflow was recorded over time. 2D images of saturation were captured every minute. After the water in the column reached equilibrium between the pressure steps, 3D tomograms were taken. Figures 3.6 and 3.7 show the 3D water content at steady state, derived from the tomograms. Figure 3.8 shows the depth averaged water content at transient conditions, derived from radiograms. In Figure 3.5, the total outflow of water over time is presented. In case of the periodic structure during the first two steps no outflow has been measured. Therefore, those two steps are not visible in Figure 3.5.

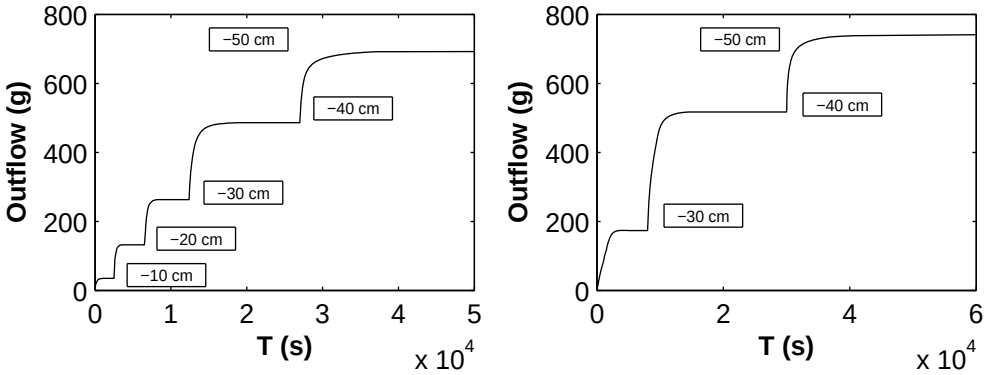

Figure 3.5 Measured cumulative outflow curves. Left: random structure; right: periodic structure. Pressure labels indicate the pressure value at the bottom boundary leading to the respective steady states.

A clear influence of the structure of the columns is visible from the different onset of drainage in the columns and from the difference in the water content in the columns at the steady states in Figure 3.5. In the periodic column, water was trapped in the coarse-material inclusions, as air could not access the coarse cells through the fully saturated surrounding material (see assumptions of Richards equation in the section 2.1). Therefore, the outflow starts only after the pressure head was lowered to -30 cm at the bottom boundary, and the earlier steps are not shown in the graph.

Figure 3.8 shows a snapshot of the transient 2D depth-averaged saturation distributions in the random and the periodic column, taken during the pressure step from -20 cm to -30 cm. The bottom part of the periodic column is still completely wet, while it is partly drained in the random column. In this transient state, the lowest cells of coarse material in the periodic column have not been

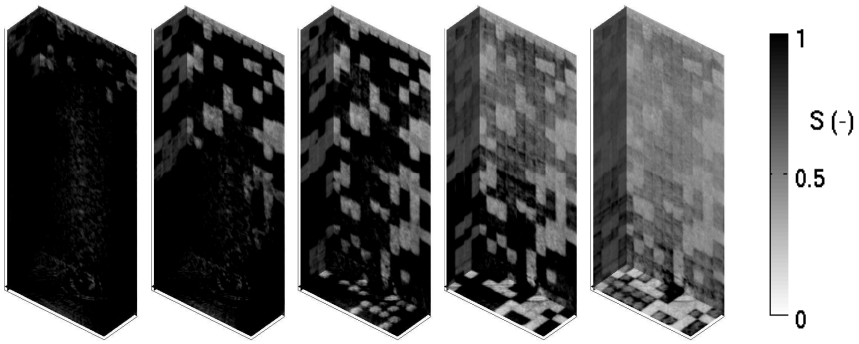

Figure 3.6 Steady-state 3D tomography (random structure): water distribution in one cross section of the 3D image. The pressure head at the lower boundary is (from left to right): -10 cm, -20 cm, -30 cm, -40 cm and -50 cm. High water content is indicated by dark grey.

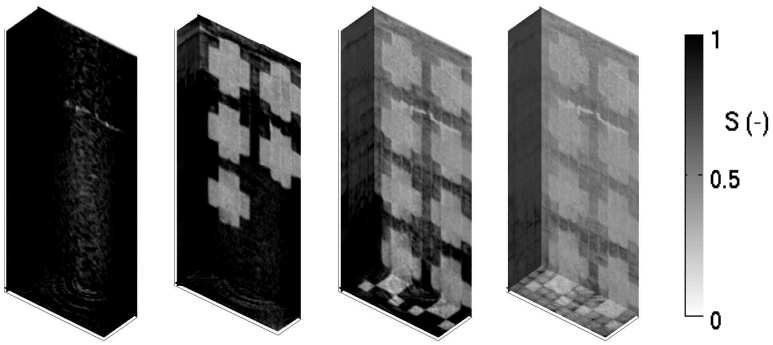

Figure 3.7 Steady-state 3D tomography (periodic structure): water distribution in one cross section of the 3D image. The pressure head at the lower boundary is (from left to right): -20 cm, -30 cm, -40 cm and -50 cm. High water content is indicated by dark grey.

drained yet as water is still trapped. During this pressure step, the third and fourth row of coarse cells (from the bottom) drained quite rapidly. In the second row, the front two of four cells started draining in the periodic column. This can be seen in the slightly lighter gray color in Figure 3.8. In the steady state after this pressure step, only these two of four course cells in the second row have drained. The two other cells, still completely saturated with water, can be seen in the 3D cross-section in Figure 3.7, where only the third and fourth row of coarse cells have lost water yet (second picture from the left).

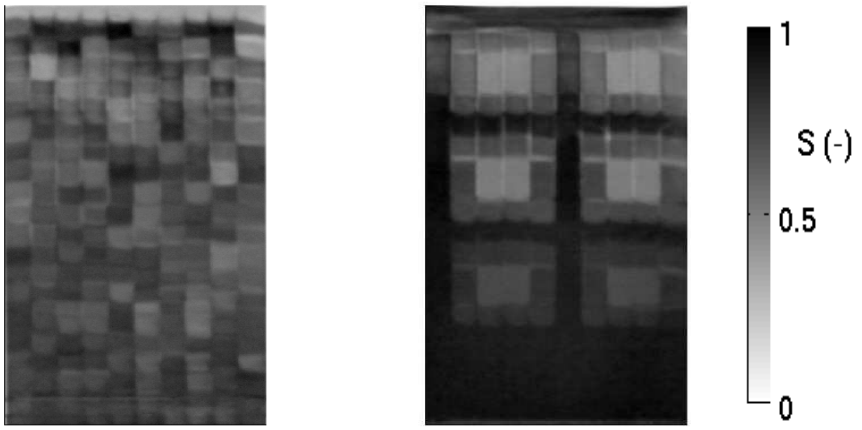

Figure 3.8 Transient 2D radiography: snapshots of depth-averaged water distributions. Left: random structure; Right: periodic structure. The pressure has decreased from -20 cm to -30 cm. High water content is indicated by dark grey.

The water level in the fine material in the periodic column had just about reached the upper part of the coarse cells in question after the third pressure step (-30 cm), so that it depended on single configurations of the pore-scale structure (most likely at the column walls) of the packing whether a coarse cell drained or not. Trapping of water in the periodic structure ceased to occur only after the pressure head was lowered to -40 cm.

The $h_c - S$ relationships for both sand types were calculated from horizontal steady-state layer-wise averages of the measured 3D water saturations in each material after each pressure step, assuming a hydrostatic pressure distribution within the column at steady state. They are shown in Figures 3.9 and 3.10. The error bars for saturations account for the measurement errors of the neutron intensities and boundary conditions. By comparing the $h_c - S$ relationships of coarse sand for both structures, we clearly see that the structure has a strong influence on the retention curves.

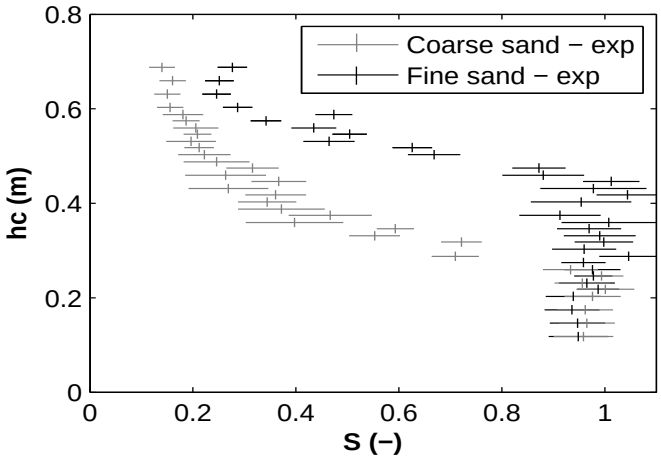

Figure 3.9 $h_c - S$ relationship (random structure) gained from experimental tomograms at each pressure step at steady states.

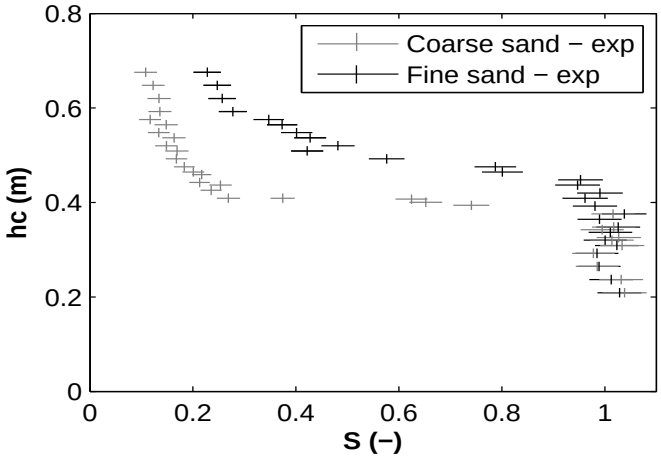

Figure 3.10 $h_c - S$ relationship (periodic structure) gained from experimental tomograms at each pressure step at steady states.

3.2 Model parameters

3.2.1 Predetermined sand parameters

To compare the measured water content with predictions made with the upscaled model, numerical simulations of the outflow experiments were performed. The quasi one-dimensional upscaled model described in section 2 (in the following referred to as "upscaled 1D model") and Richards model (equation 2.10) using the heterogeneous 3D model parameter structure (in the following referred to as "3D heterogeneous model") were used. For all numerical simulations, the MUFTE-UG code [28] that solves Richards equation using a non-centered finite volume (box) method with an implicit backward Euler discretization in time has been used.

As input, the upscaled model needs the parameters of both sands ($h_c - S$, $K_u - S$), which are sufficiently known from separate measurements in ideal cases. The parameters of the sand types used in the experiments had already been determined by Ursino and Gimmi [78] for their experiments. However, preliminary simulations with these parameters (not shown here) showed very poor agreement with the measurements. Therefore, the parameters were re-determined from samples of both sands in independent measurements using the method described in Lehmann et al. [43]. As will be demonstrated in this section, these estimates could also not be used to reproduce the measurements in numerical simulations. They will, however, be discussed here in order to illustrate the predictive power of estimated or independent parameters for processes in heterogeneous packings.

The saturated conductivities of both sands were measured in a standard flow experiment. The retention functions were gained from samples of both materials and a pore network model. The pore space of samples of both materials (fine and coarse sand) was measured using X-rays from synchrotrons at the Hamburger Synchrotron laboratories (coarse sand, voxel size 11 microns, 0.5 billion voxels) and at the Swiss Light Source (fine sand, voxel size 7 micron, 53 million voxels). The pore-network model was generated by inserting spherical structural elements in the imaged pore structure to determine the pore size diameter. The drainage was computed using an invasion-percolation algorithm. From the pore network model, the retention curves for both materials were calculated applying equilibrium conditions.

As constitutive relationships for the sands, the Brooks-Corey model for relative permeability and the retention function [6] to the data taken from Lehmann et al. [43] was fitted. The reason for choosing the Brooks Corey model was that the observed trapping of air in the periodic column can only be explained with an air entry pressure head. The Brooks-Corey model is given by:

$$S_{\mathrm{e}} = \frac{S - S_{\mathrm{rw}}}{1 - S_{\mathrm{rw}}} = \left(\frac{h_{\mathrm{d}}}{h_{\mathrm{c}}}\right)^{\lambda} \quad \text{for} \quad h_{\mathrm{c}} \geq h_{\mathrm{d}}$$
$$K_{\mathrm{u}} = K S_{\mathrm{e}}^{\frac{2+3\lambda}{\lambda}}, \tag{3.4}$$

where S_{e} [-] is the effective saturation, S_{rw} [-] the residual saturation, S the water saturation, h_{d} $[L]$ the air entry pressure head, K_{u} $[L\,T^{-1}]$ the unsaturated hydraulic conductivity, K $[L\,T^{-1}]$ the saturated conductivity, λ [-] the Brooks-Corey parameter. The independently measured parameter values of the two sands are shown in Table 3.2 and retention functions for both materials are presented in Figure 3.11.

Table 3.2 Parameter values estimated from independent measurements for the sand types used in the experiment.

Material	**K (m/s)**	λ **(-)**	h_{d} **(m)**	$S_{\mathrm{rw}}(-)$
Fine sand	1.08×10^{-4}	7.8	0.44	0.22
Coarse sand	2.43×10^{-4}	11.0	0.25	0.14

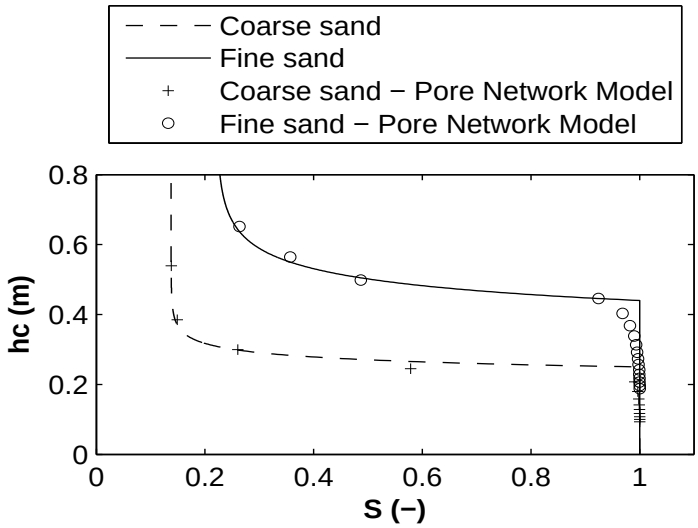

Figure 3.11 $h_{\mathrm{c}} - S$ relationships of both materials fitted to the values from pore network model.

The upscaled parameter functions based on these parameter values were then calculated as outlined in Chapter 2. For the random structure, the effective con-

ductivity was calculated using the self-consistent approach, as it has no background-inclusion structure and for a periodic one using Maxwell approach as inclusions could be easily distinguished from the background.

The comparison of measured and simulated outflow curves (3D heterogeneous model and upscaled 1D model) using the parameters from Table 2 for the random structure is presented in Figure 3.12. Also, the $h_c - S$ relationships used in the model (Table 3.2) were compared with the apparent $h_c - S$ relationships measured in the experiment in the random column (see Figure 3.13). The correspondence between experiment and prediction with the 3D heterogeneous model was poor. Therefore, the comparison is restricted to the random structure only.

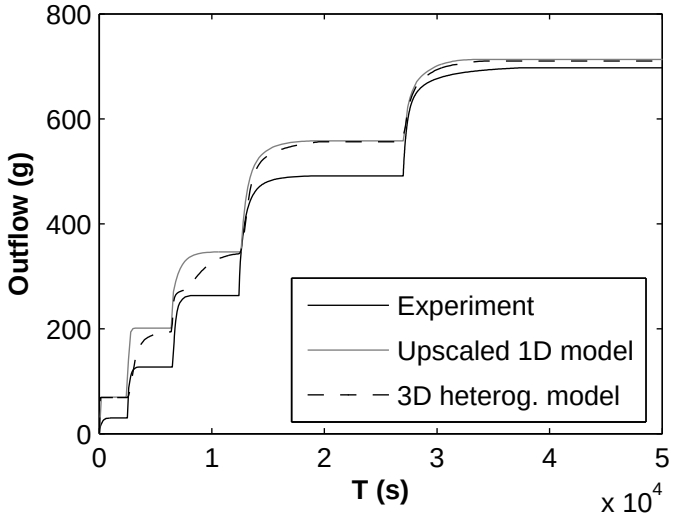

Figure 3.12 Outflow curves (random structure): Comparison of experiment, 3D heterogeneous and upscaled 1D model (with independently measured parameter values shown in Table 3.2).

Besides preferential flow at the boundaries and settling effects during the packing, some of the discrepancies can be explained by the heterogeneous structure in the columns, because the retention function could be predicted well with the same pore-network model in other studies (e.g. [1]), where homogeneous packings were analyzed. In this study, with heterogenous packings, a mixing zone of both materials at the interfaces between the different sand types occurs. In this mixing zone, the pore space is very different from the pore space in the single sand samples which were used to determine the parameters. The cubes in the heterogeneous columns should therefore not be considered to consist of one single material; their properties have rather to be considered as effective parameters which account for the effects of the interfaces.

One notable aspect of the mismatch is that the upscaled 1D model failed to follow the time behavior of the 3D heterogeneous model. The difference between

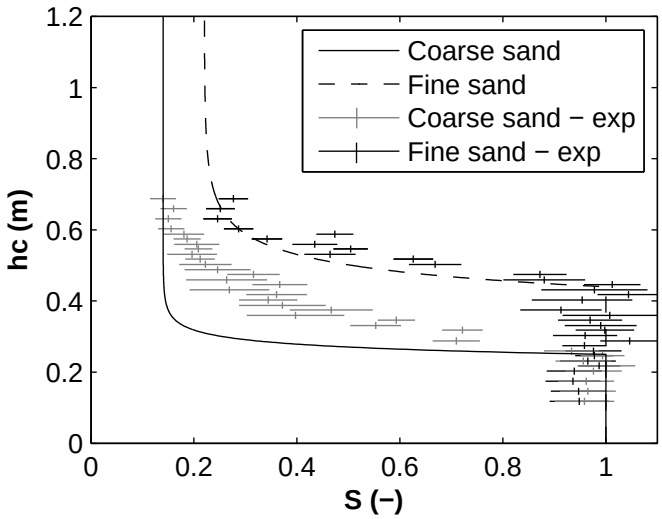

Figure 3.13 Steady state $h_c - S$ relationship (random structure) for coarse and fine material. Lines indicate model parameter functions from independent measurements (shown in Table 3.2) while symbols (error bars) indicate point values obtained by tomography in the random structure.

the outflow curves from the upscaled 1D and 3D heterogeneous models at the pressure steps to −20 cm and to −30 cm was significant (Fig 3.12). The reason why 3D model was much slower than with respect to a drainage process during the first three steps is that the effective conductivity K_{eff} was overpredicted.

An important aspect of the mismatch is that the water content in the sands is very different at comparable pressure values, leading to a very different retention behavior. According to the independent parameter values used in the numerical simulations, there is a rapid outflow from the coarse material after its air entry pressure head of 25 cm has been exceeded, and the coarse material should be almost dry at the steady state after the boundary pressure head has been lowered to -30 cm (compare Figures 3.12 and 3.13). During that same pressure step, the air entry pressure of the fine material of 44 cm has not yet been exceeded. Hence, it remains fully saturated. The upscaled 1D retention function is the averaged curve of the both sands and therefore predicts flux much faster than in the case of the 3D heterogeneous model. In this case of predetermined parameters the parameter contrast between conductivities is no longer small, implying the failure of the upscaled flow model to capture the dynamic behavior of the process.

3.2.2 Estimation of sand parameters

A comparison between the numerically simulated outflow curve using the 3D heterogeneous model and the experimental measurements shows that the parameters of the sand cubes in the columns cannot be represented well by the independently

measured parameter values (see Table 3.2). The parameters for the sands in the cubes have to be seen rather as averaged parameters which capture the specific packing and interface properties between the cubes. As these parameters cannot be measured from sand samples, they were determined from the outflow experiment described in section 3.1.3. The usual Brooks Corey model was here adjusted by assuming different λ-coefficients for the retention function and hydraulic conductivity: λ_1 is the Brooks-Corey parameter for the $h_c - S$ relationship and λ_2 is the Brooks-Corey parameter for the $K_u - S$ relationship:

$$\begin{aligned} S_e &= \frac{S - S_{rw}}{1 - S_{rw}} = \left(\frac{h_d}{h_c}\right)^{\lambda_1} \quad \text{for} \quad h_c \geq h_d \\ K_u &= K S_e^{\frac{2+3\lambda_2}{\lambda_2}}, \end{aligned} \tag{3.5}$$

where S_e [-] is the effective saturation, S_{rw} [-] the residual saturation, S the water saturation, h_d $[L]$ the air entry pressure head, K_{rw} [-] the unsaturated hydraulic conductivity, K $[L\,T^{-1}]$ the saturated conductivity, λ_1 [-] the Brooks-Corey parameters for the $h_c - S$ relationship and λ_2 [-] the Brooks-Corey parameter for the $K_u - S$ relationship.

Retention functions

The parameters of the Brooks Corey model were fitted to the data by least squares fitting (e.g., [61]). The most reliable information gained from the experiments were the measured saturations at the steady states. On the assumption of hydrostatic pressure distributions at the steady states, a water pressure head can be assigned to each vertical position in the column. These data for the fitting, supported by the cumulative outflow at steady states measured with the balance were used. The saturation measurement affected by trapped water in the periodic column discussed in section 3 (Figure 3.8) were excluded. The fitted retention functions are shown in Figure 3.14 and 3.15 and the resulting parameter values are given in Table 3.3.

The trapping in the periodic structure was accounted artificially by assigning an apparent air entry pressure ($h_{e,\,app}$) to the coarse sand, set equal to the air entry pressure of the fine sand. The apparent retention function of the coarse material in the periodic structure was then constructed so that the apparent air entry pressure head ($h_{e,\,app}$) was assigned to all saturations where the pressure head falls below the apparent value $h_{e,\,app}$ (Figure 3.15).

Hydraulic conductivities

Given the retention functions, the hydraulic conductivities were estimated by fitting the measured and the modeled outflow curves using detailed 3D numerical

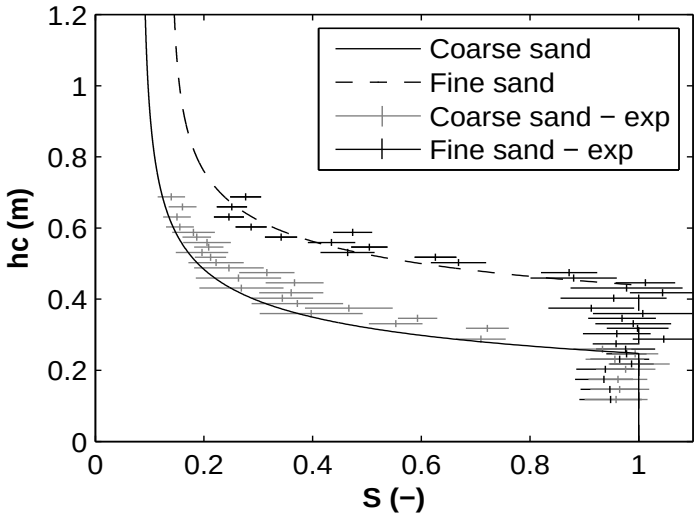

Figure 3.14 Steady state $h_c - S$ relationship (random structure) for coarse and fine material. Lines indicate calibrated model parameter functions (fitted with outflow curve, see Table 3.3) while symbols (error bars) indicate point values obtained by tomography in the random structure.

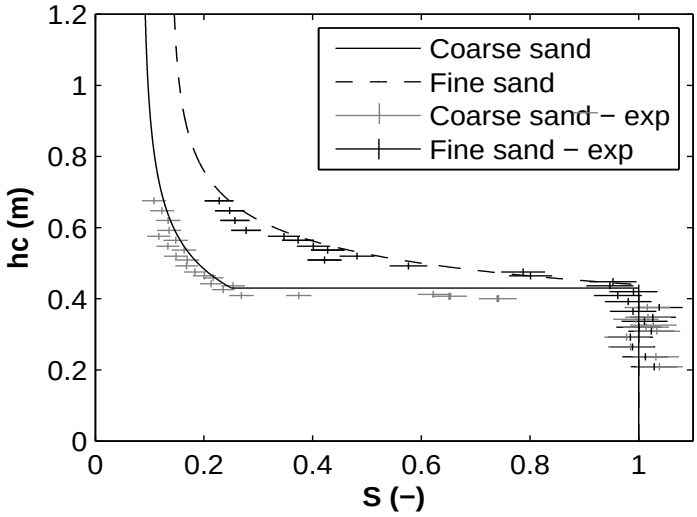

Figure 3.15 Steady state $h_c - S$ relationship (periodic structure) for coarse and fine material. Lines indicate calibrated model parameter functions (fitted with outflow curves, see Table 3.3) while symbols (error bars) indicate the values obtained by tomography in the periodic structure.

simulations. The outflow curves measured with the balance were used instead of the spatially detailed information from the radiography. The outflow directly after each pressure step happened on much faster time scales, which we resolved sufficiently with our measurements of cumulative outflow.

The total of four parameters for the hydraulic conductivity (K and λ_2 for each sand type) according to the Brooks-Corey model (equation 3.5) were fitted to the outflow curves using the Gauss-Newton combined with the Levenberg-Marquardt algorithm (e.g., [61]).

Gauss-Newton algorithm (GN): The GN algorithm was used in order to calibrate four parameters of both sands (K and λ_2 for each sand type). Here, only the basic ideas of method will be presented as well as how it was applied in this case. More detailed information about both methods could be found in Nowak [55].

GN is derived from Newton's method [61], which is used for finding a local extremum. The GN can be used only to optimize sum of square function values and has the advantage that it does not use the second derivatives [61], which is in contrary to Newton's method. The matrix of second derivatives in GN method is approximated. Therefore, GN is much faster that Newton's method. Generally, the objective function to be minimized could be presented as:

$$\chi^2 = \sum_{\mathrm{i}=1}^{\mathrm{m}} \left(f\left(x_{\mathrm{i}}\right)\right)^2 \tag{3.6}$$

An unknown $n_{\mathrm{g}} \times 1$ vector of parameters ξ (e.g. conductivities) is related to the $m_{\mathrm{g}} \times 1$ vector of measurements y (e.g. outflow, where $m_{\mathrm{g}} > n_{\mathrm{g}}$), by the relation $y = f\left(\xi\right) + r$. n_{g} is number of parameters, m_{g} number of measurements, r vector of measurement error and $f\left(\xi\right)$ a model transfer function. The objective function to be minimized is:

$$\chi^2 = \left(y - f\left(\xi\right)\right)^{\mathrm{T}} W_{\xi\xi} \left(y - f\left(\xi\right)\right) \tag{3.7}$$

where $W_{\xi\xi}$ is a $m_{\mathrm{g}} \times m_{\mathrm{g}}$ weighting matrix. This matrix is important in order to emphasis measurements, which are more certain (smaller measurement error) during minimization of the objective function. If both type of measurement (certain and not very certain) are used in the objective function, the more certain data are emphasized by choosing a higher value for that measurement in the weighting matrix $W_{\xi\xi}$. Usually, each element of the diagonal weight matrix, $W_{\xi\xi}$ should,ideally, be equal to the reciprocal of the variance (σ_{i}^2) of the measurements.

In order to minimize the square of deviations of model predictions from measurement the best possible combination of unknown parameters, which are stored in vector ξ have to be found. A brief GN algorithm would be the following [55].

- Define an initial guess of unknown parameters ξ_0. As better the initial guess, the better and faster the convergence towards the right solution will be.

- Compute $\tilde{H}_{\mathrm{k}} = \dfrac{\partial f(\xi)}{\partial \xi} \mid_{\xi_{\mathrm{k}}}$, where $\tilde{H}_{\mathrm{k}}$ is sensitivity matrix in k-th iteration step with dimensions of $m_{\mathrm{g}} \times n_{\mathrm{g}}$

- Find the next set of parameters $\xi_{\mathrm{k}+1}$ by solving:

$$\begin{aligned} \xi_{\mathrm{k}+1} &= \xi_{\mathrm{k}} + \Delta\xi \\ \Delta\xi &= \left[\tilde{H}_{\mathrm{k}}^{\mathrm{T}} W_{\xi\xi} \tilde{H}_{\mathrm{k}}\right] \left[-\tilde{H}_{\mathrm{k}}^{\mathrm{T}} W_{\xi\xi}\right] [y - f(\xi)] \end{aligned} \tag{3.8}$$

  This can be derived by linearly approximating the vector of functions $(y - f(\xi))$. The task of finding $\Delta\xi$ minimizing the sum of squares is a linear least squares problem, which can be solved explicitly. $\tilde{H}_{\mathrm{k}}^{\mathrm{T}} W_{\xi\xi} \tilde{H}_{\mathrm{k}}$ is the approximation of the matrix of second derivatives of function $f(\xi)$. Detail derivation of this problem could be find in [61].

- Increase k by 1 and repeat until convergence.

Levenberg-Marquardt algorithm (LM): The LM algorithm is a modification of the GN method that, in a self-adaptive manner, navigates between the GN algorithm and the method of steepest descent [61]. The algorithm of steepest decent points always only in direction of gradient, which means that it can take many iterations to converge towards a local minimum, if the curvature in different directions is very different (see Figure 3.16). Nevertheless, GN could have an overshoots for high non-linear problems as it linearizes the problem. Therefore, the basic idea of LM is that linear approximation of GN is good if the step is smaller. Exactly by controlling the step size LM algorithm could avoid the overshoots of the solution.

Combining the robustness of the latter with the computational efficiency of the GN method, the LM algorithm has become a highly valued optimization tool for non-linear problems of least-squares fitting in many engineering fields. The LM algorithm suppresses overshoots by controlling the step size and direction. It does it by amplifying the diagonal entries of equation 3.8 in GN algorithm. This concept has already been applied to geostatistical inverse modeling. In cokriging-like procedures, the measurement error appears on the main diagonal of the so-called cokriging matrix, which resembles the matrix of second derivatives in many ways. It has advantage over GN that it finds solution even if initial guess is very far from a final minimum. A brief LM algorithm would be the following [55].

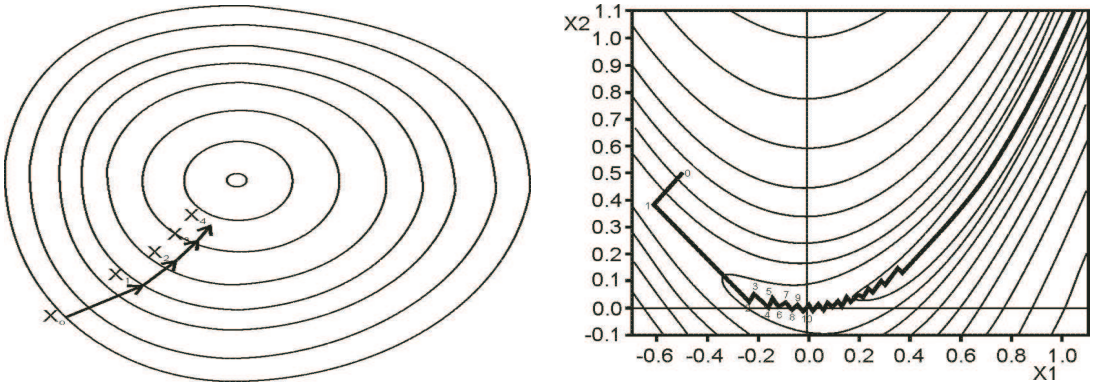

Figure 3.16 Left: Steepest descent are suitable for ellipse shaped objective functions. Right: Steepest descent is not suitable when curvature is very different in different directions (banana shaped).

- Define an initial guess of unknown parameters ξ_0 and initialize the LM parameter for innovation λ with $\lambda > 0$.
- Compute sensitivity matrix $\tilde{H}_{\mathrm{k}}$.
- Compute the next set of parameters $\xi_{\mathrm{k}+1}$ by solving:

$$\begin{aligned} \xi_{\mathrm{k}+1} &= \xi_{\mathrm{k}} + \Delta\xi \\ \Delta\xi &= \left[\tilde{H}_{\mathrm{k}}^{\mathrm{T}} W_{\xi\xi} \tilde{H}_{\mathrm{k}} + \lambda D\right] \left[-\tilde{H}_{\mathrm{k}}^{\mathrm{T}} W_{\xi\xi}\right] [y - f(\xi)] \end{aligned} \tag{3.9}$$

  if the objective function does not improve, increase λ and repeat step 2, otherwise decrease λ
- Increase k by 1 and repeat until convergence.

The D is a unit matrix. The term λD amplify the diagonal entries of the Hessian matrix in equation 3.9. Initially, λ is assigned a low value, $\lambda > 0$. Whenever convergence is poor, λ is increased by a user-defined factor, and is again decreased whenever convergence is good. For $\lambda \to \infty$, the step size $|\Delta\xi|$ approaches zero, the search direction approaches the direction of steepest descent, and there is always an improvement of the objective function unless ξ_{k} is a minimum. As ξ_{k} converges towards the solution, λ can be decreased to zero. Ideally, during the last iteration steps, the unmodified system of equations is used and the algorithm is identical to GN algorithm.

Application of GN and LM algorithm in calibration of the parameters: In order to calibrate parameters of both sands, both GN and LM algorithm have been combined. Four parameters for $h_{\mathrm{c}} - S$ relationships are already obtained

by means of least square analysis (see previous section). As initial guess ξ_0 for the rest of four unknown parameters (K and λ_2 for each sand type), the values obtained from independent measurements (see Table 3.2) have been used.

Two unknown parameters of the coarse sand (K and λ_2) were calibrated using only the first two steps of outflow curve from the random structure (-10 cm and -20 cm from the bottom of the column) as fine sand in the random structure did not drain at all for those two pressure steps (see Figure 3.6). This was very helpful as the remaining parameters of each material separately could be obtained. In order to calibrate the parameters of the coarse sand, the measured data of outflow for the first two steps in the random structure were sorted in the vector y. In order to calculate sensitivity matrix $\tilde{H}_{\mathrm{k}}$ two simulations have been performed. In the first one only hydraulic saturated conductivity of the coarse sand K (see Table 3.2) was increased for ΔK, whereas in the second simulation only λ_2 (see Table 3.2) was increased for $\Delta\lambda_2$. After obtaining results from those two simulations, the sensitivity matrix of derivatives $\tilde{H}_{\mathrm{k}}$ could be calculated and parameters K and λ_2 for coarse sand according to GN algorithm could be updated. The updated parameters were subjected to one more GN step using the same procedure as described above in order to improve the fit for the first two steps in the outflow curve (random structure). After performing the second GN loop, the LM algorithm was used in order to find a local minimum of objective function (equation 3.7) and further improve fit of outflow. The LM parameter λ (see equation 3.9) has been changed several times. The global minimum of the objective function (equation 3.7) was found for $\lambda = 0.6$. Those parameters K and λ_2 of coarse sand for which the minimum of objective function has been reached are defined as a calibrated values and used in further calculations in order to find the remaining two unknown values K and λ_2 of fine sand.

A similar procedure as explained for coarse sand has been used in order to fit the remaining two unknown parameters of fine sand (K and λ_2), but this time all outflow date gained from both columns were used in order to fit the remaining two parameters. In order to do that, the measured data (outflow) from both columns were sorted in one vector y (data from periodic column at the top and random at the bottom of the vector). Again, as initial guess ξ_0 for K and λ_2 of fine sand, the values obtained from independent measurements (see Table 3.2) have been used. This time in order to be able to construct the sensitivity matrix, four simulations needed to be done. By increasing saturated conductivity K by ΔK, the simulations of outflow in both columns were performed. Again, λ_2 of fine sand has been increases for $\Delta\lambda_2$ and simulations of outflow in both structures were performed. Again the $\tilde{H}_{\mathrm{k}}$ matrix of derivatives was calculated and new values of parameters K and λ_2 were defined according to algorithm of GN presented above. One more GN has been repeated and afterwards LM algorithm was applied, where the local minimum of objective function has been found for $\lambda = 0.62$.

The modeled and measured outflow curves are shown in Figures 3.17 and 3.18, and the parameters are given in Table 3.3. The random structure shows a good overall fit. The periodic structure shows a different picture. The outflow for the last pressure step (-50 cm) matched well, but the third and fourth pressure steps (-30 cm and -40 cm) of the periodic column do not match satisfactory at all. They are, however, not expected to match due to the restricted air entry into the coarse cells and the corresponding trapping effects. This effect in the retention function was considered by means of the horizontal line shown in Figure 3.15. This line is certainly artificial and is not expected to fit the experiments in every respect. It leads to accurate steady-state saturations, but overestimates the speed of drainage when the coarse cells suddenly drain (seen in the third and the fourth pressure steps).

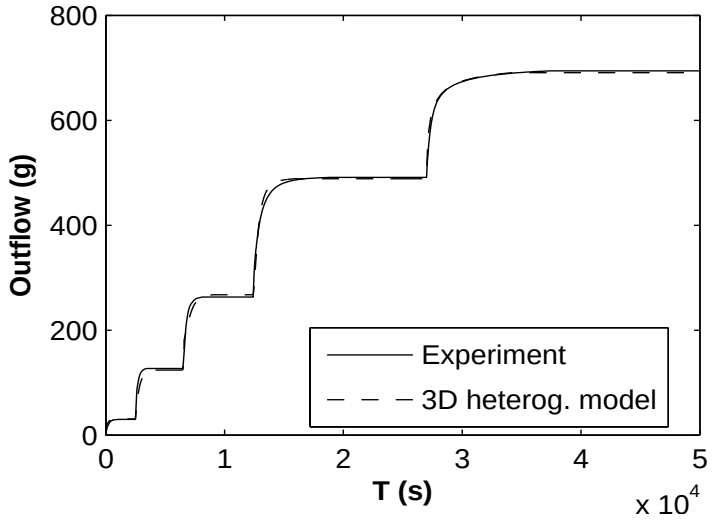

Figure 3.17 Outflow curves (periodic structure): Comparison of measured and simulated outflow using calibrated parameters (see Table 3).

Table 3.3 Parameter values for the sand types used in the experiment from the calibration.

Material	**K (m/s)**	λ_1 **(-)**	λ_2 **(-)**	h_d **(m)**	$S_\mathrm{rw}(-)$
Fine sand	3.78×10^{-5}	4.7	9.9	0.44	0.14
Coarse sand	5.83×10^{-3}	2.9	9.9	0.25	0.10

In order to control the goodness of fit for the outflow curves, a one-sided χ^2 hypothesis test (equation 3.10) on a 5% significance level was performed for both

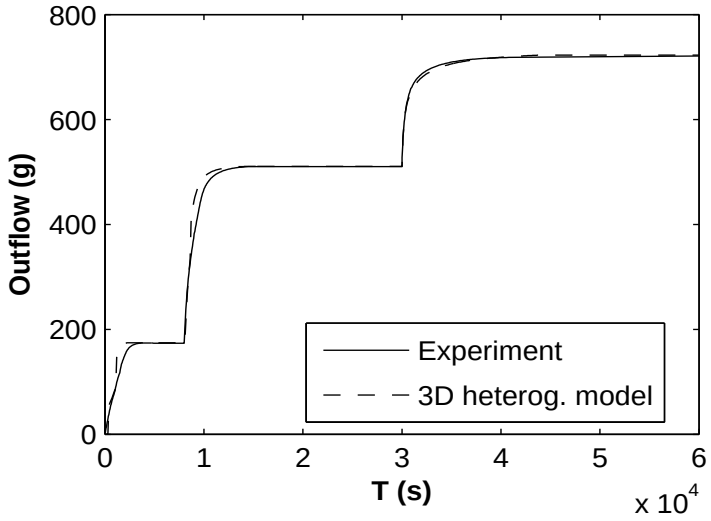

Figure 3.18 Outflow curves (random structure): Comparison of measured and simulated outflow using calibrated parameters (see Table 3).

outflow curves separately. The overall fit is accepted if the value of χ_0^2 gained from equation 3.10 is smaller than the critical value $\chi_{0.05}^2$ for both columns. Here, the number of degrees of freedom (n) in the χ^2 distribution is the number of the outflow measurements ($m = 283$ for the random column and $m = 322$ for the periodic column) minus the number of fitted parameters ($p = 8$ for both columns as we have four unknown parameters for each sand). The critical values resulting from the χ^2 distribution with n as given above and $P = 95\%$ were $\chi_{0.05}^2 = 315$ for the random and $\chi_{0.05}^2 = 355$ for the periodic structure. The test value is given by:

$$\chi_0^2 = \sum_{\mathrm{i}=1}^{n} \frac{(O_{\mathrm{mod}} - O_{\mathrm{meas}})^2}{\sigma_{\mathrm{dev}}^2 + \sigma_{\mathrm{obs}}^2 + \sigma_{\mathrm{bc}}^2}, \tag{3.10}$$

where O_{mod} is the simulated outflow, O_{meas} the measured outflow, σ_{dev} the standard deviation of mass measured with the balance, σ_{obs} the standard deviation due to uncertainties in the time of measurement (higher for fast outflow and zero in case of equilibrium) and σ_{bc} the standard deviation due to uncertainties in fixing the pressure boundary condition. The fit was clearly accepted with $\chi_0^2 = 298 \ll 315$ for the random column and $\chi_0^2 = 312 \ll= 355$ for the periodic one.

The measurement error σ_{h} for the head of the boundary condition was in the range of ± 1 cm. The resulting error of water mass in the column was estimated the following way. The water mass in the columns at each boundary condition h_{b} related to the values $h_{\mathrm{b}}+1$ cm and $h_{\mathrm{b}}-1$ cm was determined. The difference

between corresponding water mass values was identified with the 95% confidence interval of a normal distribution and set to $4\sigma_{\mathrm{bc}}$. For example, in the case of the random structure for boundary condition of -20 cm, σ_{bc} was estimated to be 5.5 g and in the case of -40 cm, σ_{bc} was 12.0 g.

As a second error, the observation error (σ_{obs}) was included in the total error. As the outflow from the column was rapid after boundary pressure decrease, it was assumed that the time error was σ_{t} =1 second. The time error decreased with time as the outflow became slower. Therefore, σ_{obs} was determined according to equation 3.11:

$$\sigma_{\mathrm{obs}}^2 = \sigma_{\mathrm{t}}^2 \left(\frac{\partial O_{\mathrm{meas}}}{\partial t} \right)^2 . \tag{3.11}$$

The standard deviation due to the error of the balance σ_{dev} was negligible compared with the previous two.

Upscaled model

The effective retention function and the effective conductivity based on the fitted parameters for both sands presented in Table 3 were calculated as described in section 2. The effective conductivities were estimated with the self-consistent approach (equation 2.26), which is appropriate for the random structure, and with the Maxwell approach (equation 2.25), which is appropriate for the periodic structure.

The effective retention curve for the periodic column was derived according to equation 2.24. As retention curve of the coarse material, the changed curve with the apparent entry pressure as described in section 5.1 was used. However, the exact value of $h_{\mathrm{e,\,fine}}$ as apparent entry pressure was not used, as this would lead to an over prediction of water content in the column. In reality, a whole coarse block drains as soon as the surrounding fine material touching the uppermost part of the block starts to drain. The effective model with $h_{\mathrm{e,\,app}} = h_{\mathrm{e,\,fine}}$ would predict drainage of the uppermost layer of the coarse cell only, as it is only there that $h_{\mathrm{e,\,fine}}$ is exceeded. In order to account for the immediate and complete drainage of the entire coarse inclusion block once the fine material drains in the upper part and air can enter the coarse material, an apparent air entry pressure head which is slightly smaller than $h_{\mathrm{e,\,fine}}$ was chosen. The effective retention curves are shown in Figures 3.19 and 3.20. The outflow curves predicted with the upscaled 1D model and the estimated parameters together with the measured outflow curves are shown in Figures 3.21 and 3.22.

The effective conductivity $K_{\mathrm{eff}}(h_{\mathrm{c}})$ of the periodic column was, additionally to the Maxwell approach estimate (equation 2.25), derived as prescribed by the homogenization theory (see section 2.1.4). The two curves differ only slightly

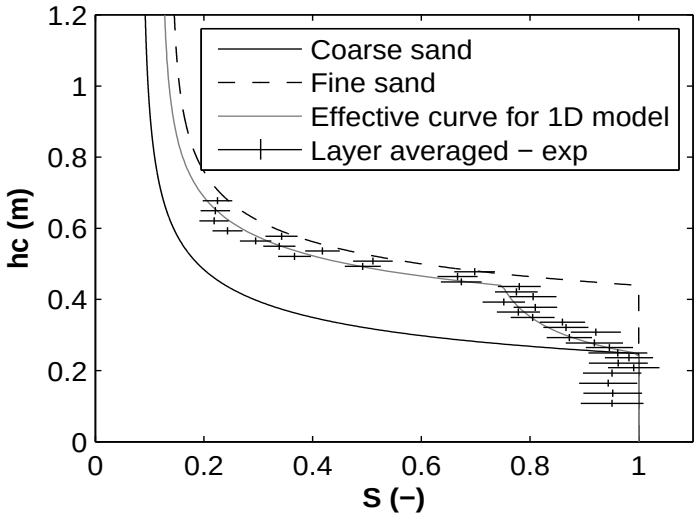

Figure 3.19 Effective retention curves (random structure): Comparison of the effective Brooks-Corey retention curve with the apparent steady-state retention curve observed in the experiment at steady states.

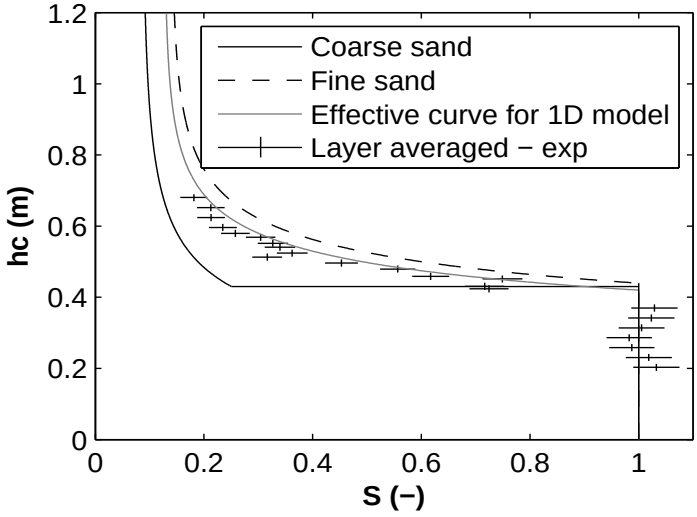

Figure 3.20 Effective retention curves (periodic structure): Comparison of the effective Brooks-Corey retention curve (fitted to the upscaled curve according to homogenization theory) with the apparent steady-state retention curve observed in the experiment at steady states.

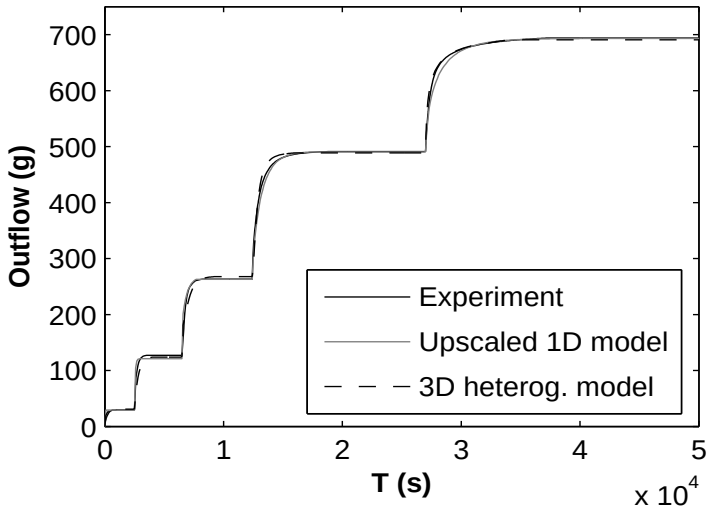

Figure 3.21 Outflow curves (random structure): Comparison of experiment, 3D heterogeneous and upscaled 1D model (using the calibrated parameter values shown in Table 3.3).

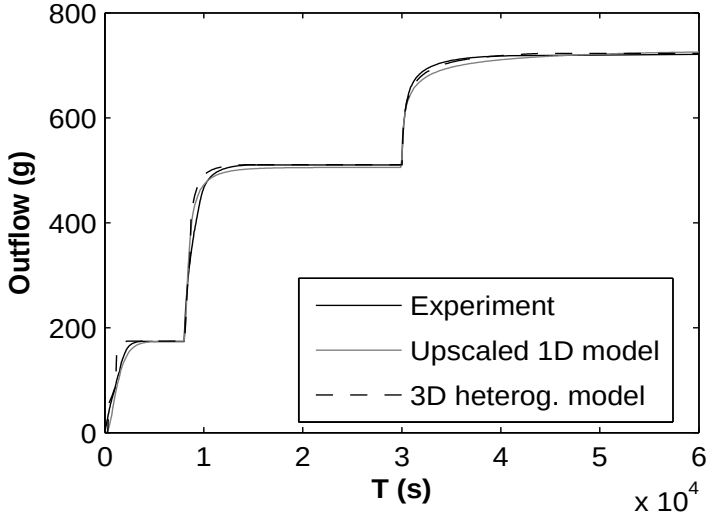

Figure 3.22 Outflow curves (periodic structure): Comparison of experiment, 3D heterogeneous and upscaled 1D model (using the calibrated parameter values shown in Table 3.3).

for capillary pressure heads higher than the entry pressure head ($h_{\mathrm{e,\,fine}}$). Nevertheless, in the range below the entry pressure head (saturated conditions), the saturated conductivity predicted with the homogenization theory is higher than the one predicted with the Maxwell approach (Figure 3.23). As the time behavior of outflow at saturated conditions is strongly dominated by the derivative of the $h_{\mathrm{c}}-S$ relationship ($\partial h_{\mathrm{c}}/\partial S$), the different effective conductivity curves $K_{\mathrm{eff}}\,(h_{\mathrm{c}})$ at saturated conditions do not influence the time of outflow significantly. Therefore, the corresponding outflow curve can hardly be distinguished from the outflow curve simulated with the estimated parameters (Maxwell approach) except for a slightly slower outflow under rather dry conditions, where the influence of $K_{\mathrm{eff}}\,(h_{\mathrm{c}})$ on the time behavior increases. The outflow curves are shown in Figure 3.24.

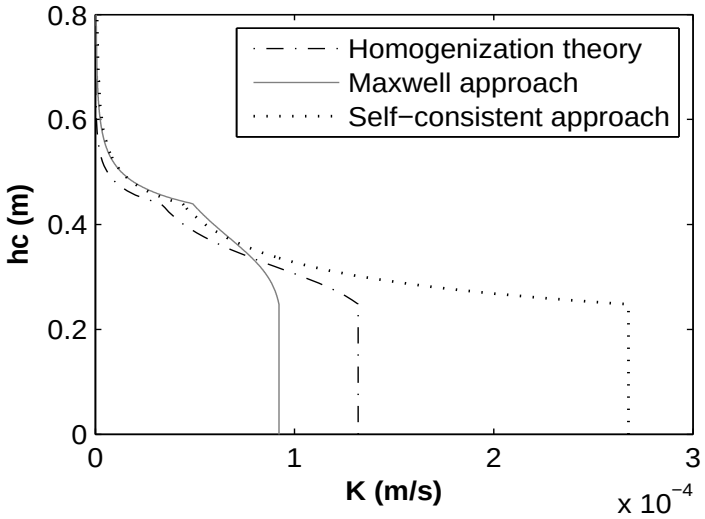

Figure 3.23 Comparison of $K_{\mathrm{eff}}\,(h_{\mathrm{c}})$ curves derived by Maxwell approach, self-consistent approach and homogenization theory.

3.3 Comparison of experiments and models

The purpose of this study was to compare predictions of unsaturated flow made with upscaled models with experimental observations in heterogeneous media. The two columns used for these experiments (the multi-step outflow experiments discussed in section 3) had the same spatial dimensions and were filled with the same volume percentages of the two sand materials. The crucial difference is that one had a regular, periodic structure and thus a well-defined macroscopic elementary volume. The existence of a representative elementary volume is an important requirement for upscaling methods. Moreover, the fine sand in the periodic structure was connected throughout the entire column, while the coarse

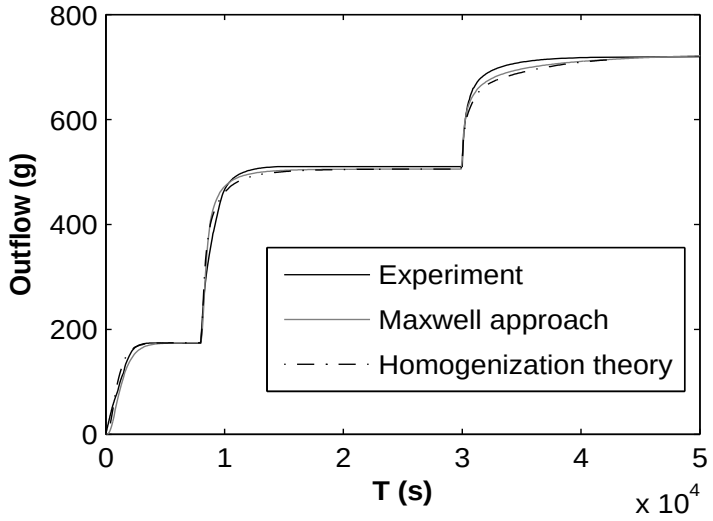

Figure 3.24 Outflow curves (periodic structure): Comparison of experiment, upscaled 1D model with the parameters estimated with the Maxwell approach and upscaled 1D model with the parameters obtained from the homogenization theory

sand was structured in completely isolated inclusions. Therefore, estimations of the hydraulic conductivity based on the Maxwell approach are assumed to be suitable for the periodic structure. The other column can be considered the opposite in these two respects. It has no macroscopic representative elementary volume and both coarse and fine sands have connected paths running through the entire column.

The first question to be addressed is how well upscaled models predict the movement of water if the assumptions made in upscaling methods are met as good as possible (as in the outflow experiments in the periodic structure). The second question is how good these predictions are once the assumptions are no longer met (as in the outflow experiments in the random structure).

3.3.1 Modeling water content in the periodic structure

During the drainage process in the periodic column, water was trapped in the inclusion material (discussed below in section 6.3). Trapping of water is not described by the Richards equation. It is thus only reasonable to compare the upscaled 1D model with the experiment for conditions where all the trapped water had drained. This was the case in the last pressure step (to -50 cm).

For this pressure step, the upscaled 1D model with the estimated parameters made good predictions for the periodic column, both with respect to the steady states in the column and for the time behavior of the total outflow (Figure 3.22) from the column. The upscaled model overpredicts the equilibrium time of the

outflow only slightly.

This statement also holds for local water content inside the column. As the periodic structure consists of 16 unit cells arranged in four layers (Figure 3.1), the averaged saturations in the bottom and the top of the four horizontal layers of unit cells over time were compared. The averaged water content in the first and fourth layer of unit cells from the bottom is shown on the right in Figure 3.25 for the fifth pressure step (to -50 cm) and shows a good agreement. On the left of Figure 3.25, the fourth pressure step (to -40 cm) is shown. In this case, the time behavior of the decreasing water content is predicted much too fast by the upscaled 1D model. This was to be expected due to the horizontal tangent of the effective retention curve (Figure 3.25), which was introduced to account for the trapping of water. It is clear that this construction of the effective retention function can only account for the total mass of water in the column at the steady states, but not for the time behavior of the outflow.

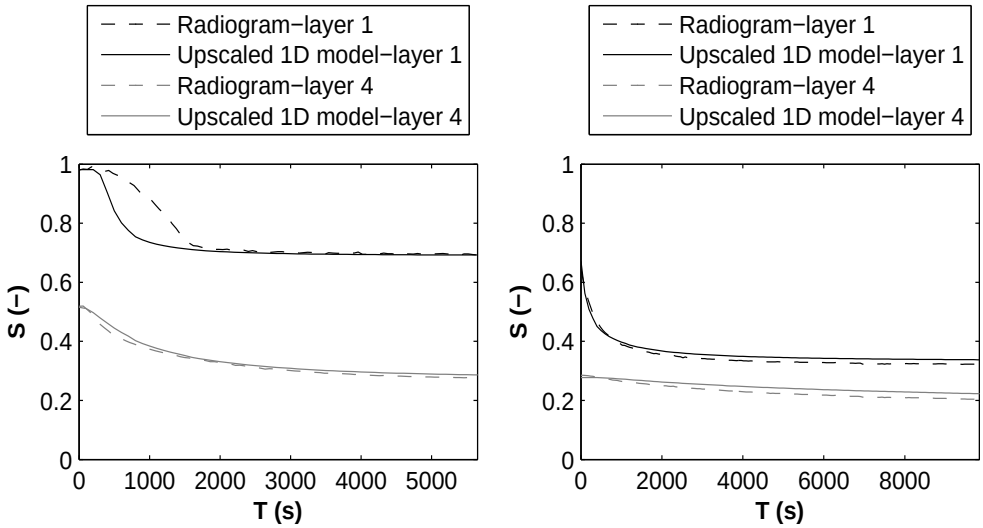

Figure 3.25 Transient saturations (periodic structure): Comparison of simulated transient saturations (layer 1 and 4 from the bottom, using calibrated parameter values shown in Table 3) to the layer-average of the transient saturations measured in time series of 2D radiograms. Left: pressure drop from -30 cm to -40 cm; right: pressure drop from -40 cm to -50 cm.

The periodic structure was designed to fulfill the assumptions made in the upscaled model as much as possible. Still, the criterion of separation of length scales is hardly met for the column. The typical microscopic length scale ℓ is the size of the unit cell, while the typical macroscopic length scale L is the size of the column. Here, the ratio between the two length scales was $\varepsilon = \ell/L = 0.25$, which is smaller than, but not very small compared to one. That means, the structure is at the borderline of fulfilling the assumptions of scale separation. It

is remarkable that, despite of this discrepancy, the upscaled 1D model using the homogenized parameters did not deviate much from the measurements. Also, the outflow curves of the upscaled 1D model using the homogenized and estimated parameters did not significantly differ, except under dry condition, where they differed slightly. This is an indication that, unless under very dry conditions, the few pieces of information used in the Maxwell approach are sufficient to predict drainage processes.

3.3.2 Modeling water content in the random structure

As for the periodic structure, the experimental retention function and outflow curve are compared with the prediction made with the 1D upscaled model. The upscaled 1D model is the same as that used for the periodic structure, except that no apparent entry pressure was assigned to the retention function (Figure 3.14). As in the periodic structure, the predictions made with the upscaled 1D model were good (see Figure 3.21).

This statement is also true for the locally averaged water content in the column. As the random structure has no defined unit cell, the spatial averages of the water content over the same subvolumes as for the periodic structure (four layers) were compared. The averaged water content of the first and fourth layer are shown in Figure 3.26.

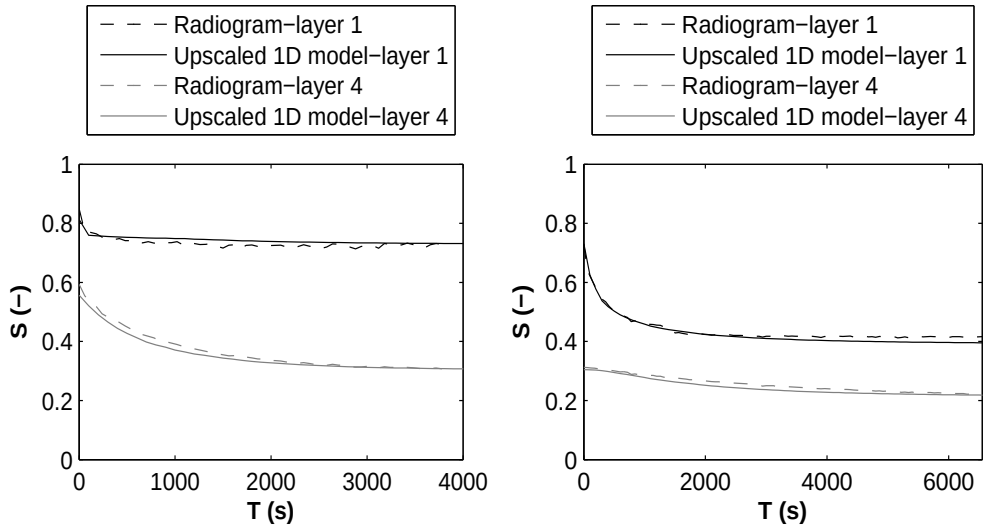

Figure 3.26 Transient saturations (random structure): Comparison of simulated transient saturations (layer 1 and 4 from the bottom, using calibrated parameter values shown in Table 3) to the layer-average of the transient saturations measured in time series of 2D radiograms. Left: pressure drop from -30 cm to -40 cm; right: pressure drop from -40 cm to -50 cm.

Although, in the random structure, the assumption of scale separation made

in the derivation of the upscaled model is clearly violated, the predictions with the upscaled 1D model are good. Apparently, for the experiments carried out here, the violated assumptions regarding the structure did not limit the applicability of the upscaled model.

3.3.3 Influence of structure on the outflow process

As outlined above, the heterogeneous structure of the column did not restrict the applicability of the upscaled model for the predictions of flow. However, it had an influence on the flow behavior and the upscaled models were able to account for these differences.

The **retention behavior** of the columns was effected by their structure due to the trapping of water. In the periodic structure, the drainage did not start before a bottom boundary pressure head of -30 cm was applied, as the coarse material was not connected to the top (see section 3). Therefore, water was trapped in the coarse cells, as air could not reach them through the completely wet fine material. When the flow in the columns is modeled with the Richards equation, this trapping effect in the periodic column can not be captured directly. The Richards equation assumes that air is always connected to the atmosphere, so that water-saturated capillary barriers cannot prevent air entry into regions that would otherwise drain. In principle, the process would have to be modeled with a two-phase flow model. In this study, the trapping of water in the periodic column was accounted by assigning an apparent entry pressure to the coarse material (see section 3 and Figure 3.15). This model simplifies the accessibility for air with the horizontal line in the $h_c - S$ curve.

In order to predict such apparent entry pressure effects in practical applications, the fact that coarse sand is embedded in fine sand has to be known. Information about such structures could be obtained, e.g., from the genesis of the soil, if connected structures of fine material are expected in sediments. The entry pressure of the fine sand may be estimated from information on the grain-size distribution. Even if the material properties of the soil are not known very well, qualitative understanding of the flow behavior in such a medium can be improved by structural information. Without this information and the accordingly modifications, the upscaled 1D model used for the periodic structure would falsely be assumed to be applicable. An unmodified model would clearly make poor predictions (in this case it would, e.g., predict five outflow events instead of three for the periodic structure).

Apart from the retention curves, the structure of the columns had no significant influence. The **hydraulic conductivity** of the two columns could be modeled in the upscaled 1D model with the same properties. This can be illustrated by comparing the transient outflow during the last pressure step (from -40 cm to -50 cm, see Figure 3.5). As discussed before, the water content was

comparable in both columns at the beginning of this pressure step. The relaxation time for the drainage after this pressure step was equivalent for both columns. As the time behavior of the flow depends on the conductivity of the medium, it is concluded that the structure of the columns did not have a strong influence on the effective conductivity of the columns.

This conclusion, however, is not a general one. For materials with higher parameter contrasts, we might expect to encounter different behavior.

3.3.4 Extended analysis with numerical simulations

Validated models (1D upscaled and 3D heterogeneous model) from section 3.3 have been used to investigate both columns numerically. The main goal was to test how upscaled model would behave when the sands in columns were more drained towards very low saturation as at the end of the multi-step drainage experiments presented here the average saturation in columns was around 0.4. Further drainage would lead to very long equilibrium time. Observations during such a long time were not possible as available measurement time in the facility at PSI was limited. Therefore, the numerical simulations for both columns have been run when boundary condition was lowered to -60 cm and than to -70 cm below the porous plate.

The resulting outflow curves from 3D heterogeneous model and 1D upscaled for both columns are presented in the Figures 3.27 and 3.28.

It can be seen that the 1D upscaled model underpredicts the equilibrium time scale for both time steps in comparison to the 3D heterogeneous model for random case. For the periodic case, it underpredicts the last pressure step.

In Figure 3.29 the contrast (ratio) between total conductivities of both sands related to the pressure in the sample is presented. It can be seen that in case of further drainage the contrast between materials is increased. Similar as in the case of pre-determined parameters (see section 3.2.1), the estimated effective conductivity by means of Maxwell and self-consistent approach are overestimated.

For materials with higher parameter contrasts, we might expect to encounter different behavior. In this case, it might be possible to capture the averaged flow behavior using non-equilibrium models (as derived, e.g., by Lewandowska et al. [46]) or by including dynamic effects (as discussed, e.g., by Hassanizadeh et al. [26]). In order to investigate further situations when the contrasts between parameters are higher and non-equilibrium conditions in the system occur, Experiment II has been performed.

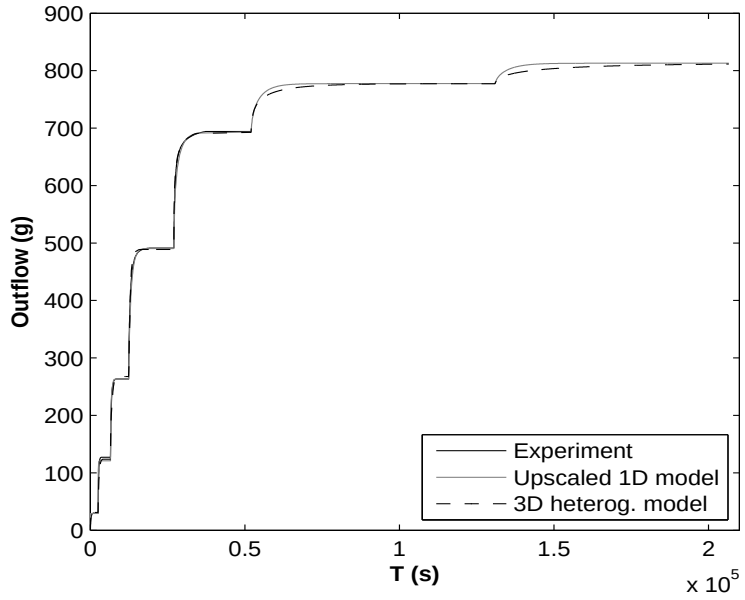

Figure 3.27 Outflow curves (random structure): Comparison of upscaled 1D model with the parameters estimated with the self-consistent approach and 3D heterogenous model in case when, boundary conditions has been lowered to -60 cm and then to -70 cm below the porous plate.

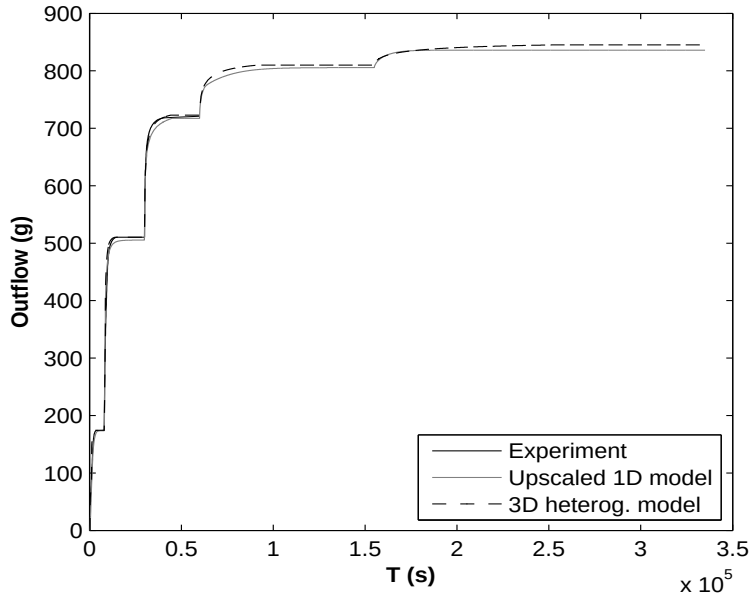

Figure 3.28 Outflow curves (periodic structure): Comparison of upscaled 1D model with the parameters estimated with the Maxwell approach and 3D heterogenous model in case when, boundary conditions has been lowered to -60 cm and then to -70 cm below the porous plate.

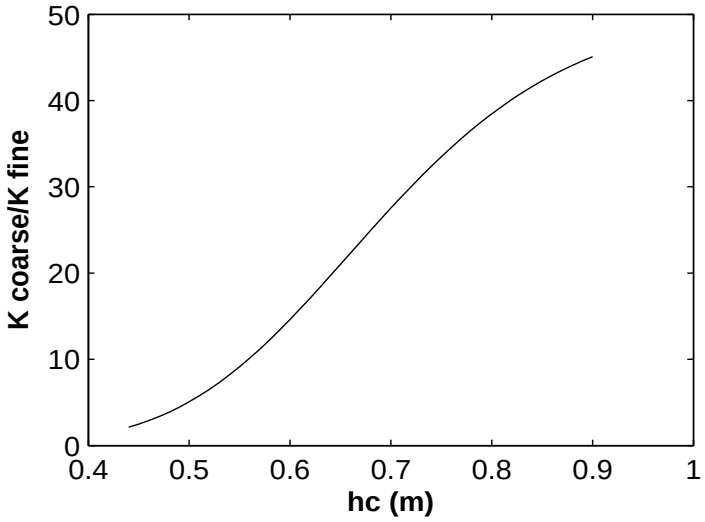

Figure 3.29 Ratio between total conductivities of coarse and fine sand dependent from the pressure in the sample.

3.4 Experiment II: Trapping of water during drainage

When upscaling unsaturated flow, heterogeneous substructures on a smaller scale may lead to phenomena, which causes deviations from the Richards model, because the water content inside of REV of the model is not at equilibrium. Those deviations can be caused by high parameter contrasts between soil parameters within the heterogeneous domain. To estimate if such phenomena has to be accounted for in a model concept, the typical time scales for the different processes need to be estimated.

The estimation of time scales is, however, for two-phase flow phenomena not straightforward, since the parameters are not fixed numbers, but depend on the variables in the medium (see Hilfer and Øren [29]). The prediction of typical time scales is still an open and challenging task because various choices of typical values for estimation of the time scales for drainage could lead to very different predictions.

In this study, an example for non-equilibrium flow is presented. It is caused by retardation of water in inclusions, which are composed of fine material compared to the surrounding material. In this case a large contrast between conductivities of materials occurs and leads to non-equilibrium conditions in the domain.

Several approaches to choose typical values are here discussed. Different predictions of time scales were compared to experimental results.

3.4.1 Time scale analysis

An estimation of the typical time scale for drainage is based on the saturation formulation of the Richards equation, which describes the change of water content in the column

$$\phi \frac{\partial S}{\partial t} + \vec{\nabla} K_{\mathrm{u}}(S) \left(\frac{dh_{\mathrm{c}}}{dS} \vec{\nabla} S + \vec{e}_{\mathrm{z}} \right) = 0, \tag{3.12}$$

where ϕ [-] is the porosity of the porous medium, S [-] the water saturation, K_{u} $[L\,T^{-1}]$ the (unsaturated) hydraulic conductivity, $\vec{e}_{\mathrm{z}}$ [-] the unit vector in z direction and h_{c} $[L]$ the capillary pressure head, which is assumed to be uniquely related to the water saturation. In order to perform a time analysis a dimensionless form of Richards equation is needed (see Chapter 2). However, to make time analysis here clearer, the dimensionless Richard equation with the dimensionless groups will be briefly showed again.

In order to present the equation 3.12 in a dimensionless way, the following dimensionless variables are used:

$$t^* = \frac{t}{T}, \;\; L^* = \frac{l}{L}, \;\; K_{\mathrm{u}}^* = \frac{K_{\mathrm{u}}}{K}, \;\; \left(\frac{dh_{\mathrm{c}}}{dS} \right)^* = \frac{dh_{\mathrm{c}}}{dS} \frac{1}{C}, \tag{3.13}$$

where variables and parameters with a star index are dimensionless, T $[T]$ is the typical time scale, C $[L]$ a typical value of the inverse capacity dh_{c}/dS, L $[L]$ a typical length scale and K $[L\,T^{-1}]$ a typical unsaturated hydraulic conductivity. The dimensionless form yields:

$$\frac{\partial S}{\partial t^*} + \vec{\nabla}^* K_{\mathrm{u}}^* \left(\frac{KTC}{\phi L^2} \left(\frac{dh_{\mathrm{c}}}{dS} \right)^* \vec{\nabla} S^* + \frac{KT}{\phi L} \vec{e}_{\mathrm{z}} \right) = 0. \tag{3.14}$$

There are two dimensionless groups, which quantify the contributions of the driving forces. If the dimensionless number is close to unity there is a significant change of saturation in the considered time scale and over the length scale L. Two typical time scales can be defined by that. A typical time scale for capillary driven flow (T_{c}):

$$T_{\mathrm{c}} = \frac{\phi L^2}{KC} \tag{3.15}$$

and a typical time scale for gravity driven flow (T_{g}):

$$T_{\mathrm{g}} = \frac{\phi L}{K} \tag{3.16}$$

The typical parameters are here not constant, but dependent on the water saturation (for example, the capacity C). Therefore, when estimating the typical time scale for a certain process, it is not evident how to choose the typical conductivity or the typical water capacity. A different options for estimating the time scales have been comapred to the experiment. The choice of the typical scales used for the experiment presented in the next section is discussed later.

3.4.2 Drainage experiment

A drainage experiment in a heterogeneously packed column was carried out, where fine sand was enclosed in coarse sand. The column was closed at the sides, open to the top and had at the bottom a connection to a reservoir, where the water level could be adjusted. The column was drained slowly until the air entry pressure of the fine sand in the upper inclusion was nearly reached (from -12 cm to -32.5 cm measured from the bottom of the column). This period of pressure decrease is referred in the following as "the first pressure step". At the final stage of the first pressure step, the surrounding coarse sand was already very dry close to its residual saturation. The water pressure at the bottom of the column was then decreased in one step ($\Delta t \to 0$) to a value, where the air entry pressure of the fine material was exceeded inside the whole column (-32.5 cm to 45 cm measured from the bottom of the column). This period is referred to as "the second pressure step". The outflow from the column and 3D transient spatial water distribution was measured during the experiment. Fast thermal neutron tomography (Hassanein et al. [25]) has been used to image 3D spatial water distribution during the transient flow.

Setup of the column

The column had two inclusions made out of fine sand. Those inclusions were surrounded by coarser sand (Figure 3.30). The same sands as in Experiment I have been used. The finer sand had a particle size distribution ranging from 0.08 mm to 0.2 mm and the coarse sand from 0.1 mm to 0.5 mm.

The column had a size of 5×5×12 cm^3 and was packed with individual sand cubes of 1cm^3 (1×1×1 cm^3) by means of a metal lattice layer by layer. After packing of each layer a moderate shaking has been applied. At the bottom of the column (above the porous plate) was a layer of 2 cm of fine sand for preventing entering of air. The column was packed under dry conditions. To ensure that air is not trapped in the sample during wetting, the column with dry sand was flushed with CO_2. Afterwards, the column was slowly flushed with degassed heavy water (D_2O), letting CO_2 to dissolve in the water. The degassed heavy water (D_2O) was used for sake of reducing the neutron attenuation of the neutron rays. The gravimetrically determined porosity of the sample ($\rho_{\text{sand}} = 2650\,\text{kg/m}^3$-

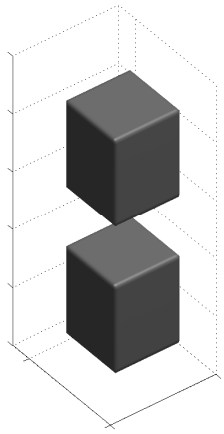

Figure 3.30 Structure of the inclusions made of finer material in the column.

solid density of the sand and $m_{\text{sand}} = 0.47\,\text{kg}$ - mass of the sand in the column) was 41% and the achieved saturation of the sample was 95%.

Fast Neutron Tomography and Radiography

In the previous Experiment I (see section 3.1.1) the slow neutron tomography was used to monitor 3D spatial distribution. Slow neutron tomography was applicable only for the samples, which are at the steady state since time needed for one tomogram was around 2h. In the case of small column, the fast neutron tomography was used. It needs 45 seconds in order to scan one tomogram. Therefore, it was applicable to monitor transient water distribution for slow processes and only to the samples that are limited to few centimeters.

The 3D resolution of the column was 945×396×396 voxels. The resulting voxel size of the images was 0.127×0.127×0.127 mm^3.

Experimental setup

The boundary condition in the column was controlled by connecting the bottom outlet with the water reservoir. The reservoir was placed on a balance, allowing to measure the outflow over time. Since the balance was on a movable table the boundary condition could be adjusted (Figure 3.2).

The saturated sample was installed on a rotating table in the NEUTRA beam line (see Figure 3.2). The table rotation is automatically controlled and synchronized with the detector system by the tomography software. The balance measuring the outflow was monitored from outside the measurement room using a camera.

The reservoir adjusting the boundary condition at the bottom of the column was linearly decreased in the first pressure step from -12 cm till -32.5 cm measured

from the bottom over a time span of 30 minutes. At the end position, the air entry pressure of the surrounding coarse material was exceeded in the whole column, while it was nearly reached for the fine material in upper inclusion. As both sands are very uniform, the surrounding coarse material was already very dry (almost at residual saturation), while the included fine material was still completely wet. This condition was used as initial condition in order to observe the retardation effect, when the boundary has been changed from 32.5 cm to -45 cm in the second pressure step.

Material properties - predetermined parameters

The time analysis and predictions of the time scales in the sample have been performed with the parameters, which were determined prior to the experiment. The parameters are presented in the Table 3.2 and the retention functions in Figure 3.11. As mentioned, the saturated conductivities of both sands were measured in a standard flow experiment. The retention function parameters were predetermined from a pore network model of the two sands separately (Lehmann [43]). Those parameters were determined with homogeneous packing of each material, meaning that no material interfaces were present in the samples during the measurements.

Estimation of time scales

Prior to the experiment the typical time scales for drainage of inclusions have been estimated using the time analysis, see section 3.4.1. Since the aim was to observe the water content of two inclusions in the column, the choice of the typical length scale was half of the column length, $L = 0.05$ m. The porosity has been measured as $\phi = 0.41$. For the typical hydraulic conductivity (K), the value of the coarse surrounding material has been chosen, as the conductivity in that material was very small at the moment when it was drained close to its residual saturation and thus determined the flow. The capacity (C) has been chosen as that of inclusion material, as this value drives the outflow. However, it is not clear for which capillary pressure head these parameters (K and C) should be chosen as it changes significantly from beginning to end stage. Thus, different choices of typical parameter values were compared.

To estimate the drainage times of the lower and upper inclusion, as the typical pressure heads for the hydraulic conductivity $K_{\mathrm{u}}(h_{\mathrm{c}})$, the pressure heads below the bottom of both inclusions at steady state for the first and the second pressure step have been used (for the first pressure step: -35.5 cm/-40.5 cm for the lower/upper inclusion and for the second pressure step: -48 cm/-53 cm for the lower/upper inclusion, see Figure 3.31a). For the typical values of capacities $C(h_{\mathrm{c}})$, the heads at the center of the inclusions were chosen. The values of the typical heads in the center of inclusions for the first pressure step (-37 cm and

-42 cm) yield capacities dh_c/dS of infinity for finer sand, whereas the estimated reaction time goes to zero or to very short reaction time as those values are below entry pressure of fine sand. Since this is artificial, instead of using these values at the steady state for the first pressure step, the heads at the beginning, intermediate and end state of the second pressure step in the center of the inclusions were used. For the values at the beginning of the second pressure step, the value of -45 cm (boundary condition) for both inclusions has been chosen, which was just above the entry pressure of the fine material (-44 cm), see Figure 3.31b. For the intermediate state, the values between two steady states after the first and the second pressure step have been chosen (-48.25 cm for the upper inclusion and -45 cm for the lower inclusion as intermediate value of -43.25 cm was again below of the entry pressure of fine material, see Figure 3.31b). Finally, the values in the center of the inclusions at the steady state after the second pressure step (-54.5 cm for the upper and -49.5 cm for the lower inclusion) were chosen. All chosen values for capacities are presented in Figure 3.31b.

Certainly, this choice of the typical values is subjected to discussion. However, prior to the experiment this choice seemed to be reasonable.

a) b)

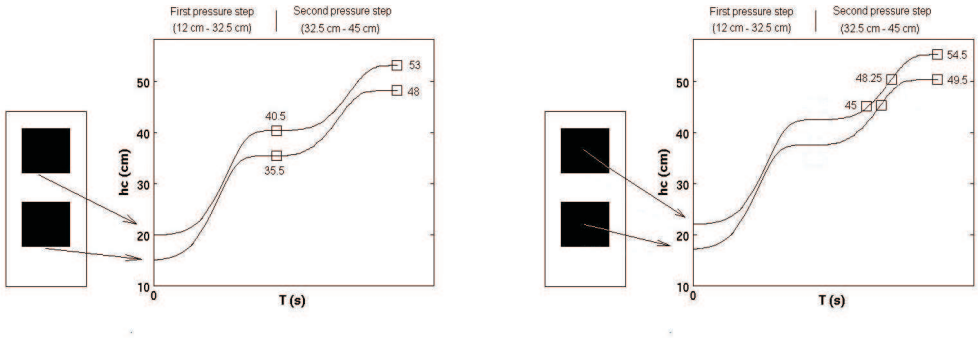

Figure 3.31 Schematic pressure propagation during the experiment at the locations where the typical values of pressure heads (□ - symbol) were chosen: a) for conductivity and b) for capacity.

The estimated time scales of draining using equations 3.15 and 3.16 are given in Table 3.4 (see only for "Predetermined parameters"). The different conductivities of the surrounding material and different slopes of the retention curve of the inclusion material for different capillary heads lead to a high difference between the differently estimated time scales for predetermined parameters, but in all cases they predict drainage of the inclusions within several days up to years. Predictions of long drainage times for fine sand inclusions have indicated, prior to experiment, that water is indeed retarded due to the reduced conductivity of the surrounding material.

Table 3.4 Estimated time scales using the pressure heads below the bottom of the inclusions at steady state for the first (K_{first}) and for the second (K_{second}) pressure step for typical conductivity and pressure heads at the beginning (C_{beg}), intermediate (C_{inter}) and end (C_{end}) state of the second pressure step for typical capacity.

Combination	T_c (s) K_{first} C_{beg}	T_c (s) K_{first} C_{inter}	T_c (s) K_{first} C_{end}	T_c (s) K_{second} C_{beg}	T_c (s) K_{second} C_{inter}	T_c (s) K_{second} C_{end}	T_g (s) K_{first}	T_g (s) K_{second}
Predetermined parameters								
Lower inclusion	$4.0{\cdot}10^{7}$	$1.0{\cdot}10^{7}$	$7.8{\cdot}10^{5}$	$3.9{\cdot}10^{9}$	$3.9{\cdot}10^{9}$	$1.7{\cdot}10^{9}$	$1.8{\cdot}10^{7}$	$6.9{\cdot}10^{9}$
Upper inclusion	$1.0{\cdot}10^{9}$	$5.5{\cdot}10^{8}$	$4.2{\cdot}10^{6}$	$1.3{\cdot}10^{11}$	$6.8{\cdot}10^{10}$	$2.3{\cdot}10^{10}$	$1.8{\cdot}10^{9}$	$2.2{\cdot}10^{11}$
Interfaces								
Lower inclusion	$7.2{\cdot}10^{4}$	$7.2{\cdot}10^{4}$	$4.0{\cdot}10^{4}$				$1.8{\cdot}10^{7}$	
Upper inclusion	$7.3{\cdot}10^{6}$	$2.3{\cdot}10^{7}$	$4.7{\cdot}10^{3}$				$1.8{\cdot}10^{9}$	

Experimental results

The cumulative mass of the outflow measured with the balance was recorded over time. The resulting outflow curve is presented in Figure 3.32. At the end of the experiment the outflow was less than 0.05 g/min. The pressures (boundary conditions) at the bottom of the columns are marked in Figure 3.32.

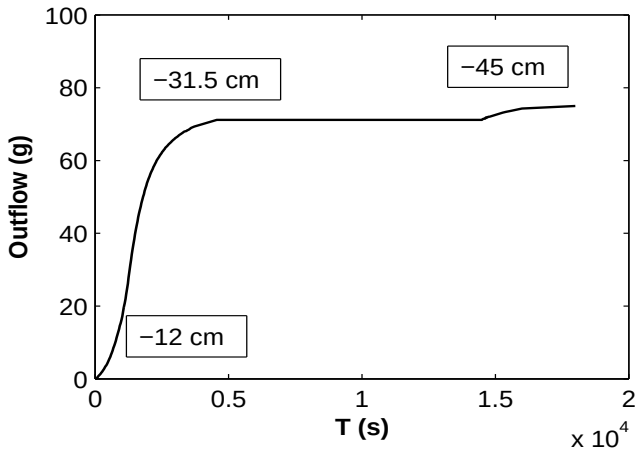

Figure 3.32 Outflow from the column over time.

Beside the outflow, the 3D spatial water distribution during the drainage was monitored by means of fast neutron tomography. In Figure 3.33, cross sections through the column for the completely saturated sample (Figure 3.33a), after the boundary condition of -32.5 cm has been reached in the first pressure step (Figure 3.33b), at the steady state after the first pressure step (Figure 3.33c) and at the steady state after the second pressure step (Figure 3.33d), are presented.

The time span between the decrease of the boundary pressure in the second pressure step and the last picture was one hour. In this time the inclusions remained wet. Furthermore, during this pressure step no drainage of surrounding

material has been observed (see Figures 3.33c, 3.33d) since it was dry close to residual saturation after the first pressure step. That implies that the conductivity of the surrounding material at the end of the first pressure step did not change significantly during the second pressure step and therefore, only K_{first} was used in further analysis (see Table 3.4). However, it can be seen from the outflow curve that there was a slight outflow of water. It can be observed from the outflow curve (Figure 3.32) as well as from the picture of the water content (Figure 3.33d) that the interfaces within the upper inclusion drained in a time span of an hour. Those interfaces were created during the packing procedure due to usage of the metal lattice. It is remarkable that the preferred drainage of interfaces can be observed only in the fine and not in the coarse material (Figure 3.33b).

a) b) c) d)

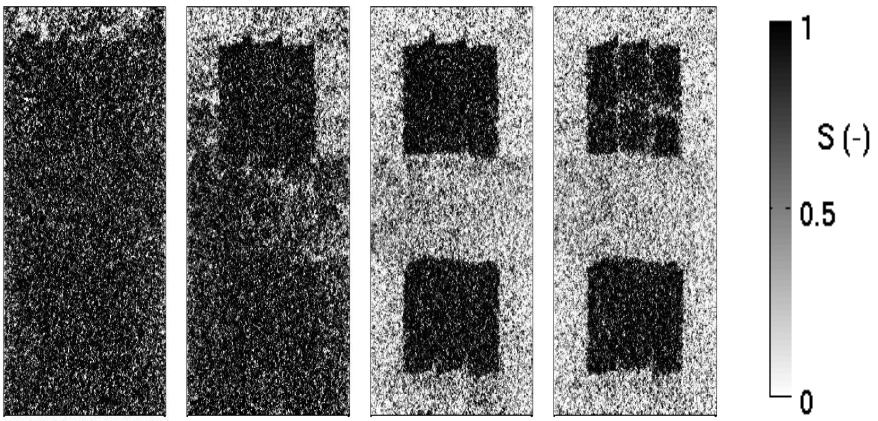

Figure 3.33 Cross section through the column: a) at the beginning of the experiment, b) after the boundary condition of -32.5 cm has been reached for the first pressure step, c) at steady state (first pressure step), d) at steady state (second pressure step).

The inner part of the inclusions did not drain over the time span of one hour after the second pressure step. It should be noted that in the drainage experiment with the same materials, where the fine material was not isolated, the fine sand drained for a comparable boundary condition (cf. Experiment I). This observation of retardation of drainage fits to the predictions of drainage times with predetermined parameters. However, the actual time scales could not be compared, since no drainage occurred during the available observation time in the facilities at PSI. Thus, from the inner part of the inclusions it could not be concluded how to choose the appropriate drainage time scale. The interfaces between the cubes, however, drained on a time scale of an hour.

3.4.3 Numerical simulation

From experiment presented above it is clear that drainage from upper inclusion was retarded as predicted by the time analysis. The numerical model (MUFTE-UG [28]) has been used to analyze the predicted time scales of both inclusions. Additionally, the model has been used to compare the drainage time of interfaces, which was measured during the experiment.

Model with two materials (coarse and fine sand)

Simulations have been performed with predetermined parameters (Table 3.2). Despite having a Brooks Corey parametrization for predetermined parameters from previous experiments (Table 3.2), the pore network model data (Lehman et al. [43]) was fitted to the Van Genuchten model [80], as a sharp entry pressure was not observed during this experiment. The amount of drained water (at the steady state) modeled with this parameter set match very well for the first pressure step (from -12 cm to -32.5 cm), where only coarse sand has been drained. Nevertheless, in order to capture the time behavior of the first pressure step, the $K_{\mathrm{u}} - S$ function for coarse sand had to be calibrated by using the measured outflow curve as the classical Van Genuchten approach could not fit the time behavior. In the case of fine sand, where no drainage during both pressure steps occurred, the predetermined parameters fitted to Van Genuchten model has been used as no other information could be extracted from the experimental results. The resulting parameters are presented in Table 3.5 and the resulting $h_{\mathrm{c}} - S$ curves are presented in Figure 3.34. Very high values of the parameter n were obtained, as the $h_{\mathrm{c}} - S$ curves obtained with the pore network model were very flat.

Table 3.5 Parameter values for the sand types used in the experiment, gained from pore network model and calibration.

Material	K (m/s)	n **(-)**	α **(m)**	$\mathrm{S_{rw}}(-)$
Fine sand	1.1×10^{-5}	20	0.5	0.22
Coarse sand	2.4×10^{-5}	23	0.27	0.14

Using this set of parameters (Table 3.5) the whole experiment was modeled. The outflow and water saturation during the first pressure step matched very well. The second pressure step showed less good agreement. This was expected, because the influence of the interfaces between the materials is not captured in one parameter set of fine material. Note, that the pre-determined parameters has

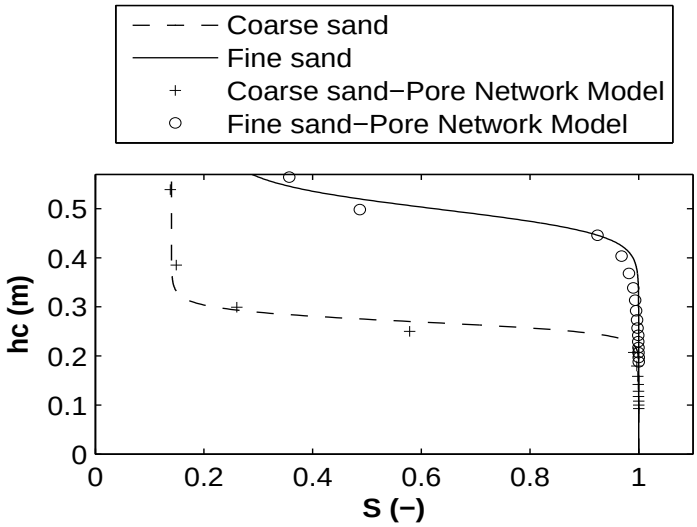

Figure 3.34 $h_c - S$ relationships (van Genuchten parametrization) of both materials fitted to the values from pore network model.

been obtained from homogeneous samples without interfaces. The comparison is shown in Figure 3.35, where the saturations of each of the two inclusion blocks have been averaged and compared to the simulation. The same has been done for the surrounding coarse sand. The comparison of the saturations in the column between the simulation and experiment is shown in Figure 3.35-left. The saturations in the coarse material and in the lower inclusion matched well. In the upper inclusion, there is a significant difference in the saturation at the end of the second pressure step. This difference comes from the drainage of the interfaces, which could not be captured by the simulation. This can be seen also in Figure 3.35-right, where the mass of water in the whole column in the experiment and the simulation is compared. At the end of the simulation the water mass is slightly higher than in the experiment. The influence of interfaces will be discussed in details in the next section.

However, in order to observe when the inclusions would drain using this parameter set and to compare drainage times with estimated times, the simulation was run for a longer period of time (see Figure 3.36). In Figure 3.36 as expected it can be seen that lower inclusion drain the first in comparison with the upper one. A drainage time needed for the complete drainage of the lower inclusion was approximately 5×10^5 seconds and for the upper one approximately 2×10^6 seconds as no drainage occurred afterwards. Calculated time scales by means of numerical model fit very well with the predictions of time scales made when K_{first} and C_{end} were used (see Table 3.4). Nevertheless, the drainage time scales predicted with K_{first} and C_{end} could not be compared with the experiment since time available at PSI was limited. However, the interfaces have drained during the experiment.

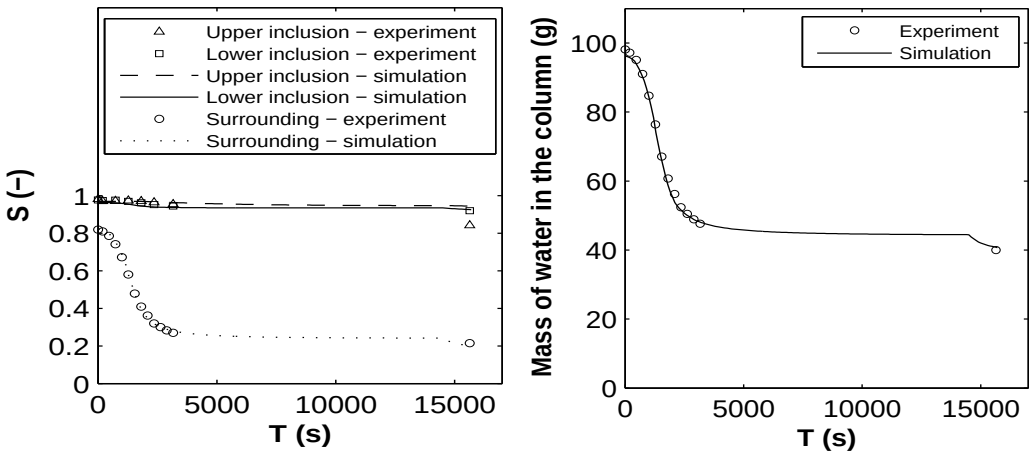

Figure 3.35 Left: Comparison of the averaged saturations in inclusions and surrounding material between the experiment and simulation. Right: Comparison of the masses of water in the whole sample during the experiment and simulation.

Therefore, another simulation was carried out, where the interfaces were treated as a third material. Typical time scales for drainage of interfaces obtained for combination of K_{first} and C_{end} are compared with experimental observations.

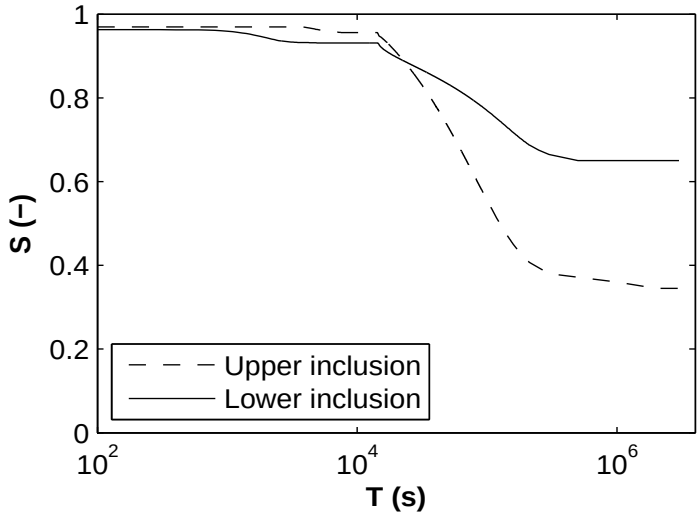

Figure 3.36 Drainage of upper and lower inclusions according to the performed simulation.

Model with interfaces

In order to perform simulations including interfaces, the parameters of the third (interface) material have been calibrated. The air entry pressure head of the inner

part of the inclusions and the interfaces could be considered as a comparable and both have a value of around -44 cm. This fact is based on the following items:

- Entry pressure for the fine sand of -44 cm is determined by Lehmann et al. [43] - predetermined parameters. In addition to that, the calibrated entry pressure in Experiment I for the same fine sand, also indicated the value of -44 cm (see Table 3.3). Therefore, one can conclude that entry pressure for this sand can not vary much from this value.

- Interfaces do not drain at the end of the first pressure step (from -12 cm to -32.5 cm), where the pressure on the top of the upper inclusion is -43.5 cm for the assumed hydrostatic pressure distribution. As interfaces during the second pressure step (-45 cm at the bottom of the column) drain before the inner part of inclusions, which entry pressure is assumed to be -44 cm, the entry pressure of interfaces could vary only between -43.5 cm and -44 cm.

The outflow time behavior during the second pressure step observed during the experiment (drainage of interfaces) has been used to calibrate other parameters of the interfaces. The entry pressure of interface material was fixed to a value slightly smaller than -44 cm. The $h_c - S$ relationship of interface sand is presented in Figure 3.37. The interfaces consist of more uniform material having the same largest pore diameter as the inner material, but obviously they are represented more than in the inner material, where also smaller pores occur. Therefore, the interface material has a similar entry pressure as the inner fine sand, but smaller slope dh_c/dS.

The simulation using those parameters could successfully reproduce the drainage of the interfaces as observed in the experiment. The interfaces in the upper inclusion have been drained within 1 hour whereas the inclusion itself remains wet (see Figure 3.38). The only difference observed was at the first horizontal interface (from the top of the column), where the water in the experiment did not drain. Most probably at that position the interface created during the packing procedure was less loose.

The time scales for the drainage of the interfaces were estimated according to equations 3.15 and 3.16. The resulting estimated times are presented in Table 3.4 (see only for "Interfaces"). The prediction of interface drainage in the upper inclusion was very good for the combination C_{end} - K_{first} as it was suggested from previous simulation with two materials. The predicted drainage of ca. 1.5 hours fits reasonably well with the observed drainage time scale of one hour.

Influence of interfaces

Prior to the experiment the existence of interfaces has not been predicted. However, from the experiment it is clear that they occur. The time scale of drainage of

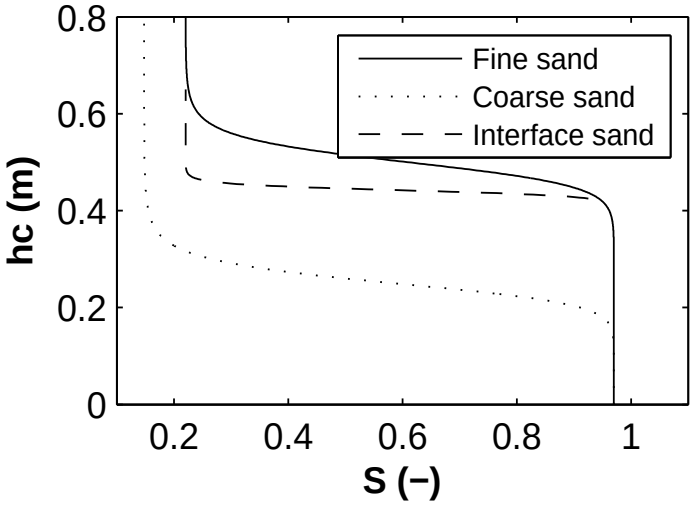

Figure 3.37 Comparison between the $h_c - S$ relationships for the fine, coarse and interface sand.

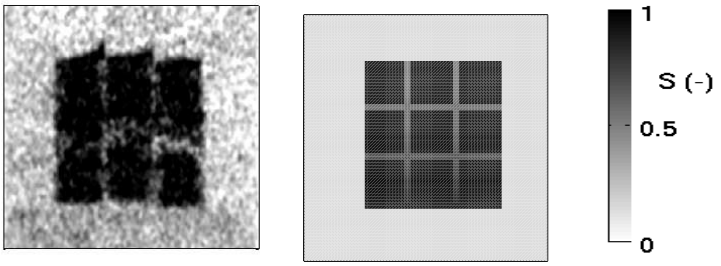

Figure 3.38 Cross section through the upper part of the for the boundary of -45 cm. Left: experiment. Right: simulation.

interfaces in this case could be predicted well. Nevertheless, as the interfaces drain within the upper inclusion, their conductivity is decreased significantly creating a barriers for flow of water in the inclusion similar to the case of the surrounding dry coarse sand and wet inclusions. In order to evaluate the influence of interfaces on drainage of inclusions, averaged saturations in the upper inclusion were compared between the simulations, where (1) only two materials have been used (without interfaces) and (2) the simulation, where all three materials (interfaces included) are used. In the case of the simulation with three materials, the saturations were averaged only for fine inner sand (interfaces were not included). The simulations have been compared and the results are presented in Figure 3.39.

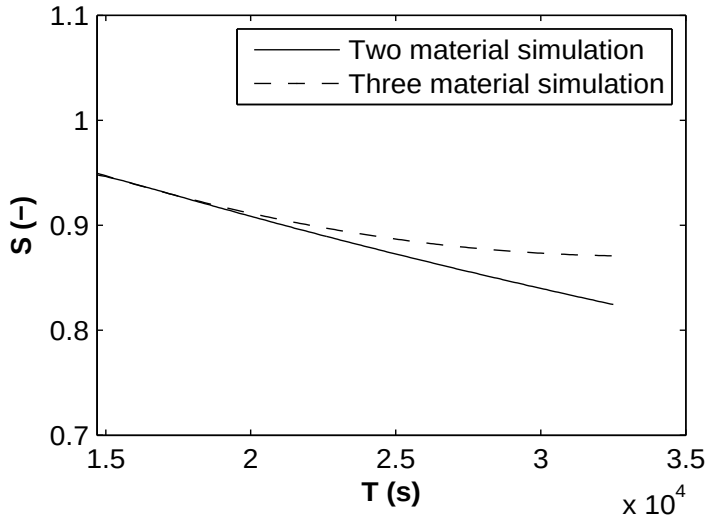

Figure 3.39 Comparison of drainage of the upper inclusion in case of existence of interfaces and in the case, when they are not occurring.

It can be seen from Figure 3.39 that the interfaces have retarded the drainage of the upper inclusion significantly, meaning that it is necessary to include their properties in the time scale analysis in order to estimate drainage time scales properly.

3.4.4 Discussion

The trapping or retardation of water in fine material, which is included in coarse material, during drainage is an important effect when modeling water flow in the unsaturated zone on larger scales since it could lead to non-equilibrium of the flow in the domain. This situation could be handled by means of non-equilibrium models, but in order to use them the typical time scales in the system have to be estimated. However, due to the strong non-linearity of the flow equations, the estimation is not straightforward. The definition of the required typical values

and results based on different approximations can yield results which differ over many orders of magnitudes. In this study, this difficulty by predicting the typical time scales during the drainage for simple example has been illustrated.

The trapping of water in such a scenario in a heterogeneously packed sand column has been observed and water content has been monitored with neutron tomography. Time scales for trapping were estimated based on predetermined sand parameters for the sands and on different approximations for the estimation of time scales. The resulting drainage times differed over several orders of magnitude.

Estimation of time scales

The prediction made by the time analysis indicated that the crucial parameter in order to have a good prediction of drainage time scales for this system is the capacity. The conductivity of surrounding material did not vary much between end of the first and second pressure step since before the second pressure decrease the saturation was close to its residual value. Using pressure heads for capacities at the end of the second pressure step would lead to good prediction of the drainage time scales of the sample (lower/upper inclusions as well as the interfaces), while capacities chosen during the pressure step would overpredict the drainage time. That means, from the span between fast and slow reaction times that could be estimated with the possible range of parameters, the system reacted with the fastest time scale.

The drainage of the interfaces in the upper inclusion could be monitored in the experiment and compared to estimated time scales. However, the inner part of the inclusions could not be observed for a long enough time span to conclude about the estimate of time scales. Therefore, estimated time scales for inclusion have been compared with the numerical simulations, where only two materials have been used. This comparison shows a good match between predictions and simulations in case of both inclusions. In case of interfaces, the predicted and simulated drainage time scales fit reasonably well with the experimental results. Both inclusions and interfaces have reacted with the fastest time scale in this example.

Influence of material interfaces

The predetermined parameters for the two materials alone are useful for the prediction of processes, which do not involve material interfaces. Using comparison of the saturations in upper inclusion between simulation with two materials and the one with three, it was clearly indicated that the drainage of upper inclusion has been retarded due to the presence of interfaces. The dry interfaces have formed barriers due to decreased conductivity for flow inside of the inclusions. This caused an extended time of drainage of inclusion, which could not be predicted

with the parameters determined from the two materials independently. It was obvious from the experiments that inclusions and interfaces have to be treated as different materials for the estimation of trapping. The role of the interfaces on the drainage of the inclusion cells suggests that the effective retention behavior away from the equilibrium of a composite porous medium depends not only on the materials it consists of, but also on the size and shape of the inclusions.

Chapter 4

Experimental studies of solute transport: influence of different parameter contrasts

4.1 Introduction

Substructures within the REV and high parameter contrast could cause retardation of water in fine sand inclusions, leading to non-equilibrium flow as discussed in the second part of Chapter 3. Non-equilibrium conditions could appear for solute transport as well. The last step of this research was to investigate non-equilibrium effects on transport in the unsaturated zone, where non-equilibrium is caused by high parameter contrasts in an investigated domain. If such a non-equilibrium situations could be predicted, a suitable non-equilibrium model (see section 2.7.1) could be used to model transport propertly. Similar to the upscaled flow models, criteria for applicability of non-equilibrium models are based on estimated time scales in the system (see section 3.4). A non-equilibrium conditions occur when time scale T at large length scale (background material) is comparable to time scale τ on small length scale (see section 2.5.1). On one specific example, it was here tried to estimate time scales and to predict if non-equilibrium conditions would occur in the investigated domain. Prior to the experiments a time analysis has been performed, where typical time scales have been determined. In that way, based on a time scale analysis the necessity for non-equilibrium approach could be predicted in order to model the transport properly. The estimates from time analysis were compared with 2D transport experiments in a flume. Heterogeneous structures have been artificially created using different materials (very fine, fine and coarse glass beads). The background of the experimental flume was filled with fine glass beads, whereas the inclusions have been filled either with coarse or very fine glass beads. The packed flume was at unsaturated conditions, where at the top of the flume water was infiltrated with constant rate. Afterwards,

dyed water (tracer) has been infiltrated in order to observe tracer front behavior. When the sample was completely colored by tracer, the infiltration was switched again to clean water. The experimental results (breakthrough curves) have been compared (additionally to the time estimates) to the analytical solution.

In order to observe water distribution and concentration of the tracer in the flume during the experiments, the light transmission method (LTM) [75] was used. Glass beads were used as filling material, because they are more transparent to the light transmission.

Among several experiments, in this section only two experiments were chosen to be presented in order to emphasize the influence of non-equilibrium on transport of conservative solute tracer caused by high parameter contrasts. Further in the study those experiments will be referred as "Experiment A" and "Experiment B".

4.2 General setup of the experiments and material properties

4.2.1 Flume setup

The flume used in experiments had dimensions of $60\times40\times1$ cm^3. The front and back side of the flume consisted of glass panels to allow transmission of light. Three different sizes of glass beads were used to pack the flume. The finer glass beads had a particle size distribution ranging from 0.1 to 0.2 mm, the coarse from 0.25 to 0.5 mm and the very fine from 0.04 to 0.07 mm. The flume has been packed horizontally to avoid layering of the material during the packing. At the beginning, the frame was glued to one glass panel using silicon. Than, the whole flume was filled with fine glass beads since this material was chosen as background (see Figure 4.1). Afterwards, using a metal lattice of different sizes, various structures of coarse material were created. The lattice was pressed in the fine glass beads background material. By means of the vacuum cleaner the area within the lattice was sucked out (see Figure 4.1). When the structure of the inclusion material was achieved the second glass panel was glued at the top to the frame, again using silicon. After the silicon dried, the glass panels were placed into the metal frame. A similar packing technique has been already tested in experiments of Heiss et al. [27].

The left and right boundaries of the flume were packed with very fine material (0.04-0.07 mm) to avoid preferential flow of air close to the boundaries reducing the width of the flume from 60 to 50 cm. The glass beads were weighted before being filled into the flume. By controlling the weight, similar properties of the glass beads packings for each experiment (every new experiment was done with a new packing) were kept. Repacking had the disadvantage that small variations

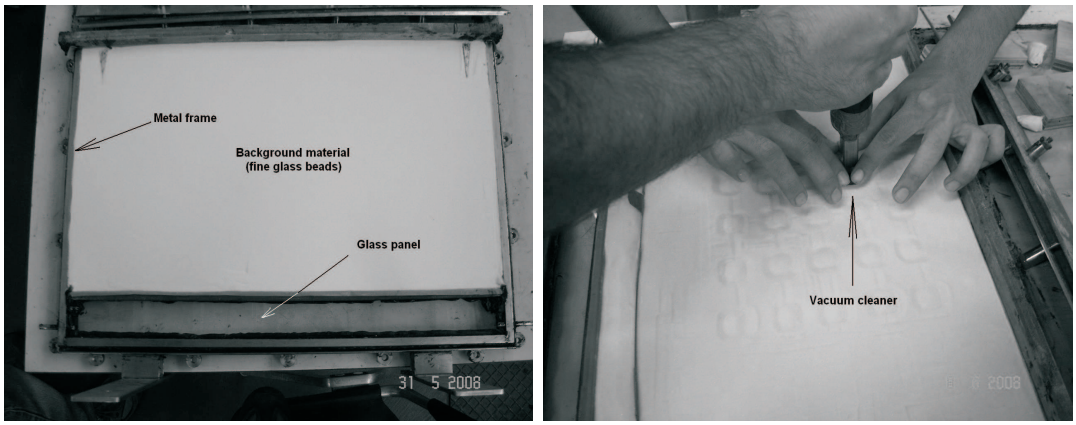

Figure 4.1 Left: Main parts of the flume. Right: Creation of the inclusions using vacuum cleaner.

in the packed structures as well as in the material properties occurred.

The flume had two outlets at the left and right hand side (see Figure 4.2), which were connected to water reservoirs. They have been used to control the boundary condition at the bottom (suction). As flow of water towards left and right outlets would create a flow field in diagonal direction from the vertical center of the flume towards the outlets, a metal bar above the outlet was included in order to create a vertical flow field. The metal bar had holes of 2 mm diameter along the whole bar. At the top, the bar was covered with a fine mesh to avoid that the glass beads drop in the lower water compartment at the bottom of the flume. Furthermore, in order to prevent air to enter into the water compartment during suction, a layer of very fine sand (0.04-0.07 mm) was created at the top of the bar (approximately 2 cm). By having this setup (metal bar and protective layer) the flow field was vertical and the lower water compartment was protected of air entering during the suction in the flume. The packed flume set up is presented in Figure 4.2

4.2.2 Material properties

The $h_c - S$ relationships of the glass beads has been measured with a classical multi-step outflow experiments [18]. The $h_c - S$ relationships of fine and coarse glass beads have been measured 2 times and by means of least square error the Van Genuchten model was fitted to the measurements. The $h_c - S$ relationship of very fine glass beads (0.04-0.07 mm) was not measured as it was expected that this material remains completely wet (saturated conditions) during performed experiments. In all experiments presented here, the entry pressure of this material has not been exceeded. The setup of the device used to measure the $h_c - S$ curves is presented in Figure 4.3. The resulting $h_c - S$ relationships of both material

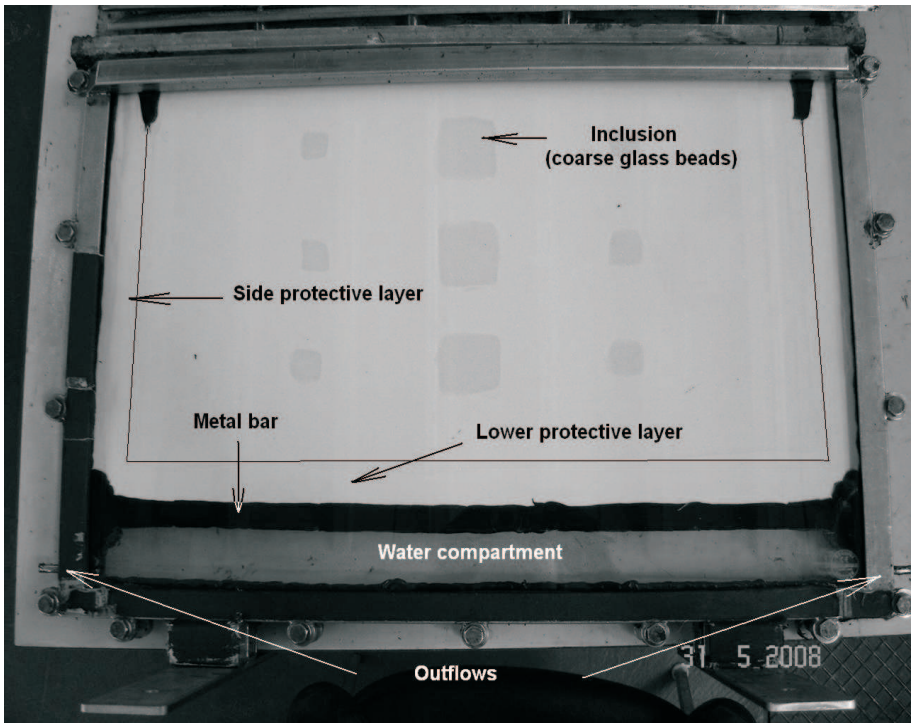

Figure 4.2 Packed flume.

together with measurement data are presented in Figure 4.4. The Van Genuchten model is used for fine and coarse glass beads, whereas the very fine glass beads remain saturated. The high values of n parameters are resulting from the very uniform glass beads grain distribution causing very flat $h_c - S$ relationships for both materials.

The intrinsic permeability, for each type of glass bead was experimentally determined using a constant head permeability test (see Figure 2.1). All measured properties are presented in Table 4.1.

Table 4.1 Parameter values for the glass beads measured in multi-step and constant head permeability experiments.

Material	**K (m/s)**	**n (-)**	α **(m)**	$S_{\mathrm{rw}}(-)$	ϕ (-)
Coarse glass beads (0.25-0.5 mm)	9.1×10^{-4}	31	0.20	0.05	0.37 ± 0.0011
Fine glass beads (0.1-0.2 mm)	2.0×10^{-4}	53	0.45	0.10	0.39 ± 0.0011
Very fine glass beads (0.04-0.07 mm)	5.5×10^{-6}	-	-	-	0.40 ± 0.0011

Figure 4.3 Device used to measure $h_c - S$ relationships of fine and coarse glass beads.

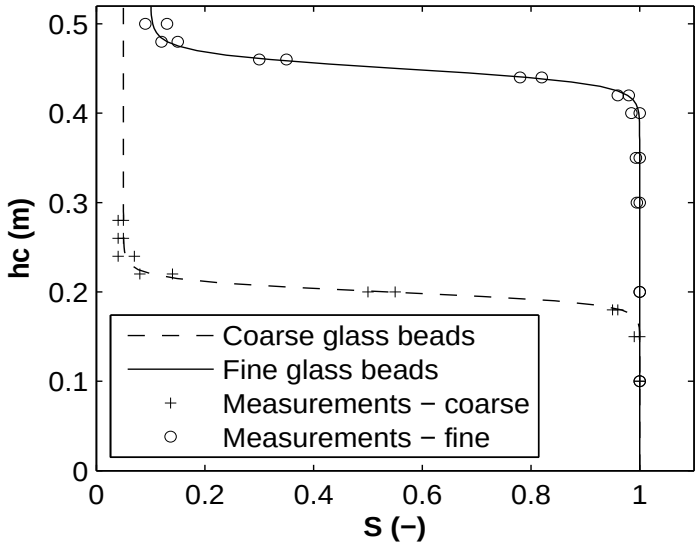

Figure 4.4 Fitted Van Genuchten model for $h_c - S$ to the measurements.

4.2.3 Experimental setup

The flume was placed in a dark chamber in order to reduce the reflection of light. At the back side of the chamber, behind the flume, a light source was placed that consisted out of six fluorescent bulbs that were installed to record the progress of the infiltration front. A camera was placed in front of the flume (see Figure 4.5).

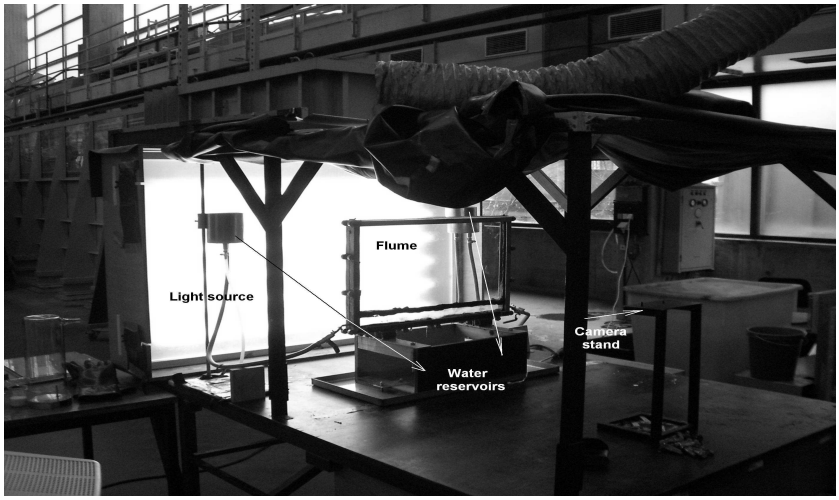

Figure 4.5 Experimental setup.

Since the flume was initially packed in dry conditions and to ensure complete water saturation, it was flushed with several pore volumes of CO_2. The top of the flume was covered with aluminium foil with tiny holes in order to minimize back air diffusion into the flume. Then, the flume was slowly flushed with 5 pore volumes of degassed water, letting the CO_2 dissolve in the water.

After the flume was initially saturated the bottom boundary condition, which was controlled by two water reservoirs, has been lowered to -26 cm from the metal bar (datum level) and waited till steady state in the flume has been reached (no outflow from the flume). At this point unsaturated conditions in the flume were achieved, where the pressure distribution in flume was assumed to be hydrostatic. After equilibrium has been reached, a uniform infiltration of clean water at the top of the flume (50×1 cm^2) with a very small flow rate ($q = 3.0$ ml/min) was started. The flow rate was controlled by means of a peristaltic pump. Uniform distribution of the inflow has been achieved using a self constructed inflow device. The inflow device had 14 outlets, where water was dropping on the top of the flume (Figure 4.6).

In each experiments, the inflow of clear water at the top of the flume has been run three days with the same inflow rate, where continuously at the bottom the same suction of -26 cm at the level of the metal bar was held constant. After a certain time, the inflow at top was equalized to the outflow at the bottom of the

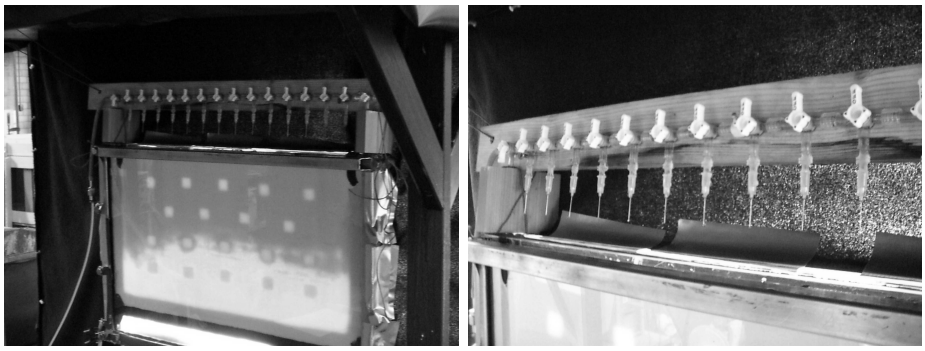

Figure 4.6 Left: Inflow device located above the flume. Right: Zoomed view on the inflow device.

flume and a quasi steady state condition in the flume was achieved. In the experiments, this was the initial condition for start of tracer infiltration into the flume. Using this small infiltration rate, the pressure distribution could be approximated as hydrostatically distributed. This approximation has been tested by simulating homogeneous flume filled with fine glass beads with same initial and boundary conditions as in the experiments, using HYDRUS 1D [69]. The measured parameters from Table 4.1 were used in the simulations. The simulations showed that the approximation of the pressure distribution as hydrostatic was feasible (see Figure 4.7), especially in lower part of the flume, where breakthrough curves are planned to be measured.

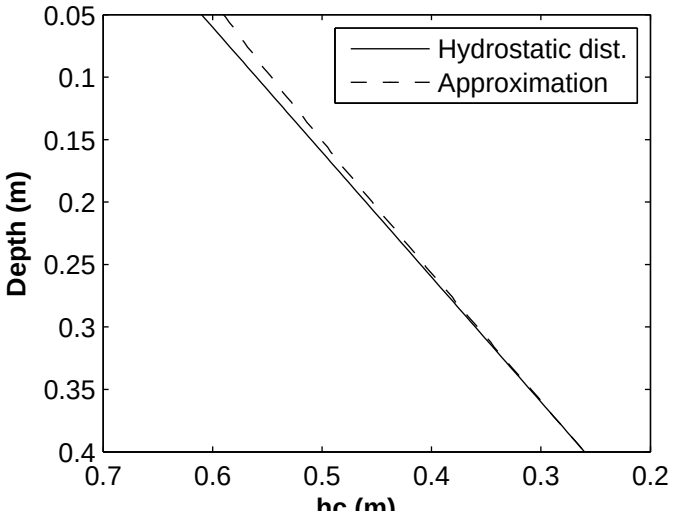

Figure 4.7 Hydrostatic pressure distribution for the known boundary conditions and the real pressure distribution (approximation).

After the quasi steady state condition was obtained (same inflow as outflow) infiltration of blue tracer was started (BASF - Patent Blue 85E 131 with chemical

formula $(C_{27}H_{31}N_2O_7S_2)_2\,Ca$) from the top with a concentration of 0.04 g/l.

As the pressure field in the flume was assumed to be known, the saturation field could be recalculated with the measured $h_c - S$ relationships (Figure 4.4). In order to be able to monitor the concentrations within the flume by using the camera images, calibration experiments were carried out, which gave the dependence of the light intensity and concentration for a certain saturation.

4.3 Calibration experiments

Calibration experiments were carried out for fine and coarse glass beads. As mentioned, the pressure field was approximated as hydrostatic. Therefore, the light transmission through the flume in relation to the concentration of the tracer could be calibrated, assuming the saturation field as known. The saturation field was calculated using the hydrostatic pressure field and measured retention curves (see Table 4.1). In next paragraphs, the calibration procedure will be briefly presented.

The flume was packed 5 times homogenously for each of the two materials (fine and coarse glass beads) resulting in total 10 packings. The calibration experiments were done for tracer concentrations of: 0 g/l, 0.02 g/l, 0.04 g/l, 0.06 g/l, 0.08 g/l. For each experiment the filling material has been weighted so that the packings did not differ from each other significantly. First, the flume was initially saturated, placed in front of the light source and an image of the saturated flume has been taken (Figure 4.8-left). Afterwards, the boundary condition was lowered to -26 cm from the metal bar. After steady state was achieved (no outflow from the flume) an image of the unsaturated flume (Figure 4.8-right) was taken. The corresponding pressure and saturation fields for the flume filled with the fine glass beads are presented in Figure 4.9. On the left and right hand side of the flume an influence of boundaries can be observed (see Figure 4.8). These areas were excluded.

Both images (saturated and unsaturated flume conditions) in case of all 10 calibration experiments were taken in two different camera modes. The first mode (further on this mode is referred in text as "Mode 1") is more suitable to monitor fine glass beads, under dry conditions, because in this case the light transmission is very low and this mode makes low transmission areas more visible. The second mode (further on this mode is referred in text as "Mode 2") is preferred in case of dry coarse sand as well as not so dry fine glass beads. In Mode 1, the shutter speed was set to 1/3 seconds and in the Mode 2 to 1/20 seconds, where the shutter speed of the camera is the time for which the shutter is held open during an taking of image. F-number in both modes was set to 3.2, where f-number of an optical system expresses the diameter of the entrance pupil in terms of the effective focal length of the lens. It is the quantitative measure of lens speed.

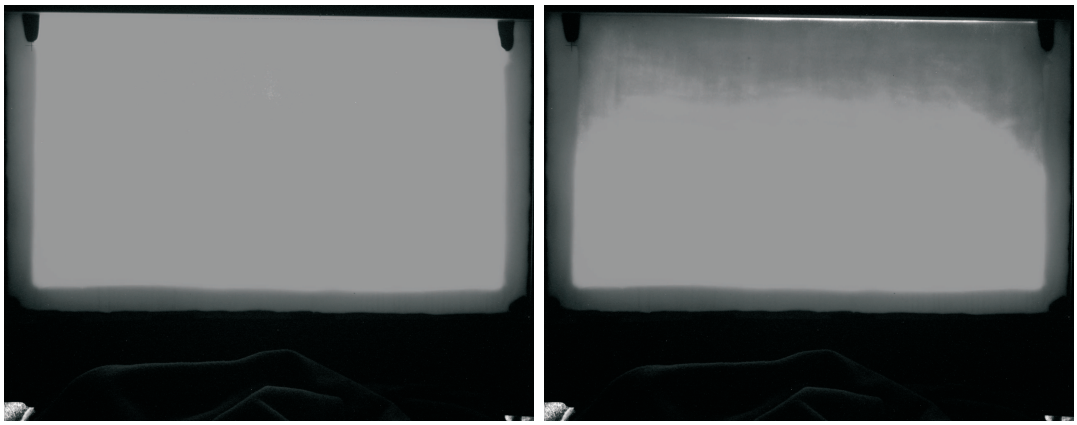

Figure 4.8 Left: Image of the saturated flume filled with fine glass beads with a tracer concentration of 0.04 g/l. Right: Image of the unsaturated flume (-26 cm boundary condition from the metal bar) filled with fine glass beads with tracer concentration of 0.04 g/l.

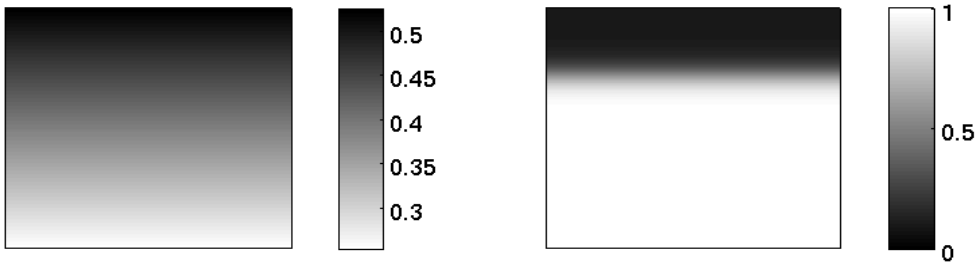

Figure 4.9 Left: Pressure field within the flume for a fine glass beads in meters. Right: Reconstructed saturation field with in the flume for a fine glass beads using parameters from Table 4.1.

The images were analyzed in MATLAB in order to define the calibration surfaces (Z axis - light intensity (I), Y axis - saturation (S), X axis - tracer concentration (C)), which could be used for extracting concentration from the images taken during the experiments. JPEG image contains three color layers: red, green and blue (RGB). The RGB color model is an additive model that combines red, green and blue in multiple ways to reproduce other colors.

In order to determine which color layer could be used for the experiments the calibration was done for all three color layers (red, green or blue) for both materials (coarse and fine glass beads) and both camera modes (Mode 1 and Mode 2), resulting in total 12 calibration surfaces. After careful analysis in several prior experiments the most sensitive surfaces for each mode and each material have been chosen, resulting in total 4 calibrated surfaces, which were used as the final calibration surfaces (two for Mode 1 - fine, coarse glass beads and two for Mode 2 - fine, coarse glass beads) in order to extract concentrations out of digital images.

In case of Mode 1 the red signal was chosen for both fine (see Figure 4.10-up) and coarse glass beads, whereas for Mode 2 the green signal was chosen. In case of fine glass beads the calibrated surfaces were monotonic having only one solution (concentration) for a certain light intensity. However, during the calibration experiment with coarse glass beads, this material has been drained to the residual saturation. Therefore, only light intensities at residual saturation have been presented. The chosen surfaces in case of fine glass beads as well as chosen values in case of coarse glass beads are presented more in details in Figures 4.11 and 4.12.

4.4 Flume experiments

As mentioned, here only two experiments (Experiment A and Experiment B) will be presented, which will emphasize the influence of non-equilibrium on transport of solute conservative tracer caused by high parameter contrasts.

After preparation and achievement of quasi steady state conditions with suction at the bottom of -26 cm in the flume (see section 4.1.1) tracer was infiltrated from the top of the flume. When tracer front had reached the bottom of the flume, the infiltration has been switched to clear water. In both experiments (Experiment A and Experiment B) the same heterogeneous structure was created (see Figure 4.13). During both experiments, tracer with concentration of $c = 0.04$ g/l at the top of the flume has been infiltrated. In the Experiment A coarse glass bead have been used as inclusion material, whereas in the Experiment B inclusions were made of very fine glass beads. In both experiments fine glass beads were used as a background material. The boundary and initial condition were the same for both experiments. In this way, the breakthrough curves of both experiments were comparable.

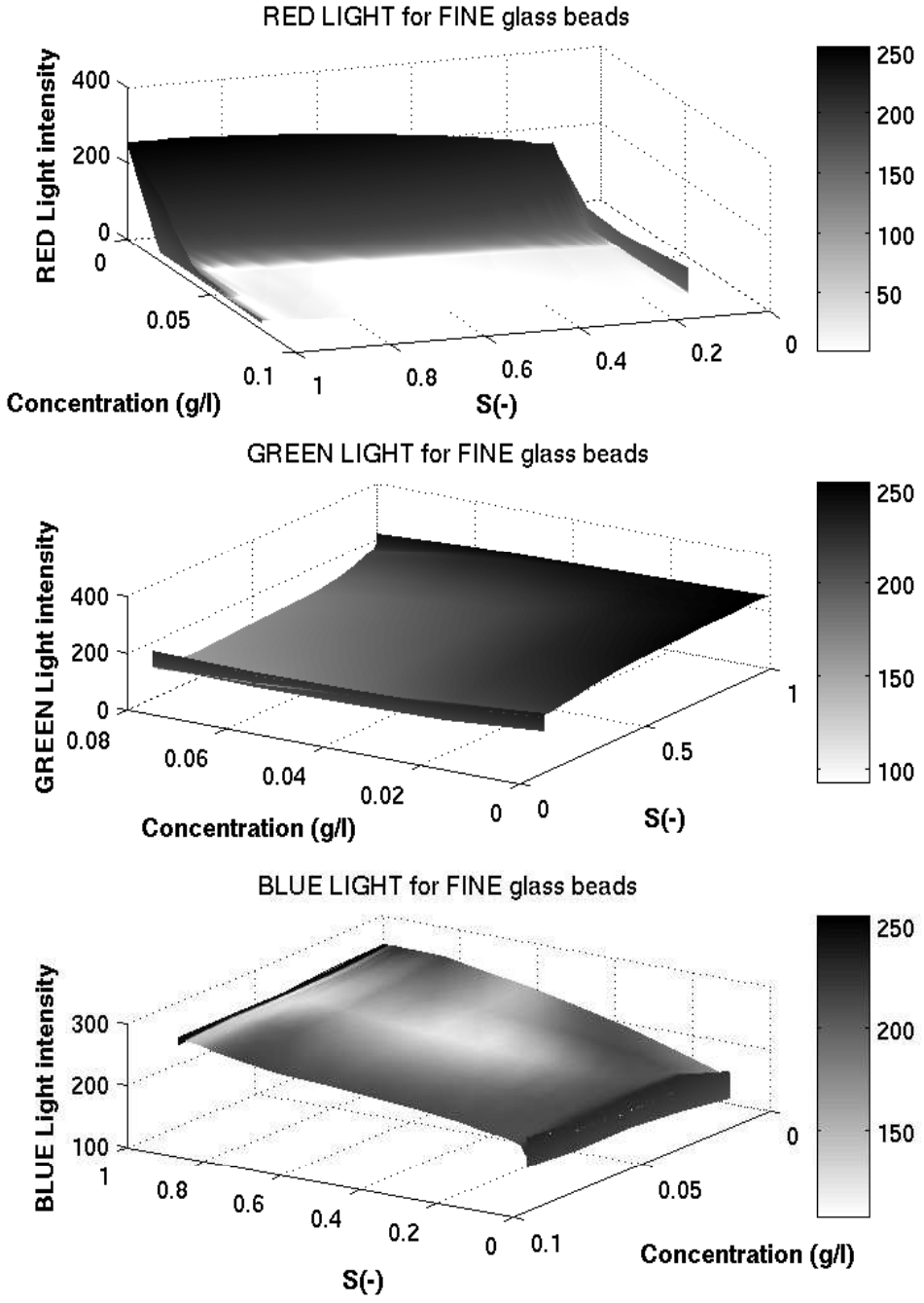

Figure 4.10 Calibration surfaces for fine glass beads and for camera Mode 1 for: up is red, middle is green and down is blue signal.

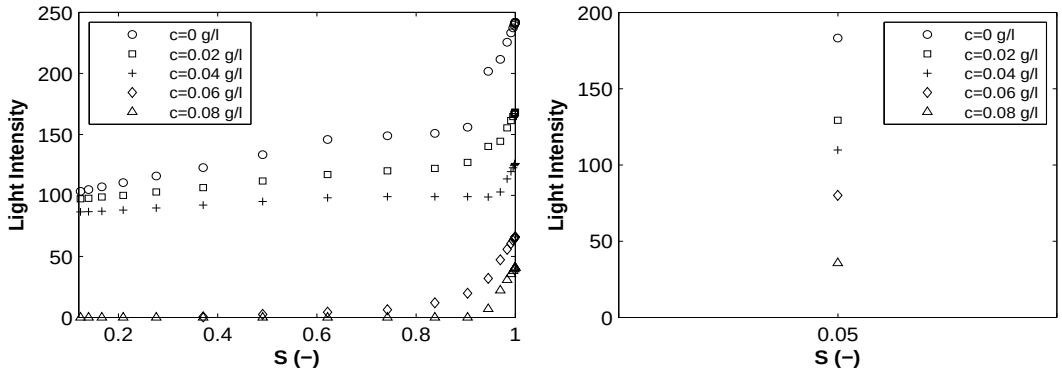

Figure 4.11 Calibration curves for different concentrations (calibration surfaces for green light (Mode 2)). Left: fine glass beads. Right: coarse glass beads.

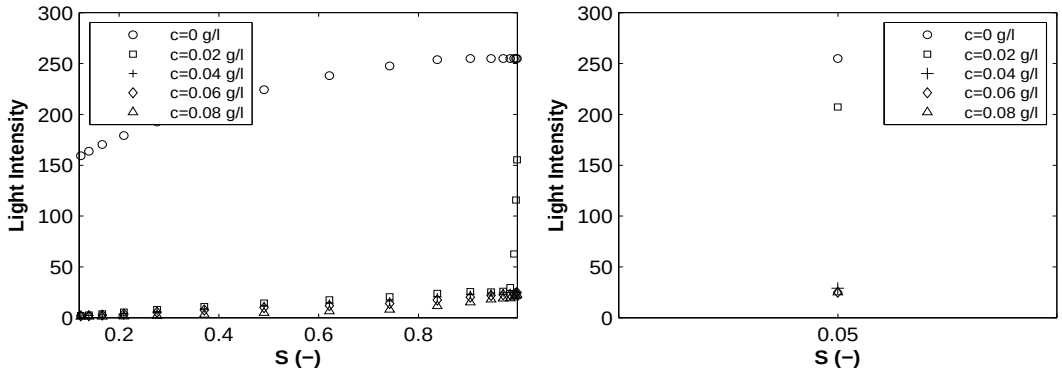

Figure 4.12 Calibration curves for different concentrations (calibration surfaces for red light (Mode 1)). Left: fine glass beads. Right: coarse glass beads.

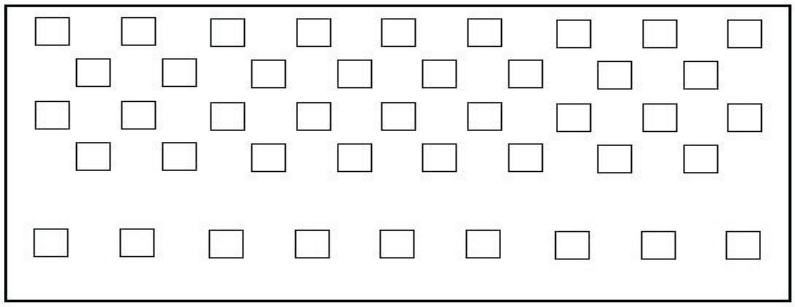

Figure 4.13 Structure created in the flume. Not to scale

In case of Experiment A, it was assumed that the coarse glass inclusions will drain and become very impermeable, whereas in Experiment B very fine glass beads would stay wet during the experiment. In both experiments the inclusions were less permeable than the background material, but the contrast between conductivities of inclusion and background material in Experiment A would be much higher than in case of Experiment B, where the inclusions would be still wet and conductive.

4.4.1 Experiment A

Typical values and time scale analysis: As mentioned, when estimating transport time scales, it was assumed that the inclusions made of coarse glass beads would be drained close to their residual saturation according to the boundary conditions of -26 cm and the measured $h_c - S$ relationship (see Figure 4.4). Therefore, the coarse glass beads inclusions were considered as very impermeable, creating stagnant zones within the domain. Therefore, the processes in the inclusions were dominated by diffusion. Typical time scales for τ and T are estimated by means of equation 2.35. The typical values used in equation 2.35 were presented in Table 4.2.

Table 4.2 Typical values used in time scale analysis.

l (m)	**L (m)**	$\bar{\Theta}_{\text{back}}$ **(-)**	U_{back} **(m/s)**	$D_{\text{incl}}(\text{m}^2/\text{s})$	$\bar{\Theta}_{\text{incl}}$ **(-)**	U_{incl} **(m/s)**
0.02	0.40	0.30	1.02×10^{-5}	2.9×10^{-8}	0.0185	3.0×10^{-30}

For a typical length scale l, the length of the inclusions has been chosen and for the large length scale L the hight of the flume. As the typical water content of background material $\bar{\Theta}_{\text{back}}$, the volume averaged water content in the background material has been selected. The water content field has been determined using the measured $h_c - S$ relationship for fine glass beads, approximating hydrostatic pressure distribution in the flume (boundary condition -26 cm from the metal bar). The Darcy's velocity in the background material U_{back} was estimated as the inflow rate at the top of the flume. The typical water content for inclusion coarse material $\bar{\Theta}_{\text{incl}}$ has been taken at residual saturation. As typical velocity in the inclusions U_{incl}, the total conductivity at saturation close to residual saturation has been chosen. The typical diffusion in coarse material at the residual saturation (D_{incl}) has been measured (see Figure 4.14) and estimated using the second central ($m_{\text{xx,c}}$) and zeroth moments (m_0) as presented in equation 4.1 [9]. The coarse glass beads presented in Figure 4.14 are at the residual saturation and during the measurement of diffusion they have been protected from evaporation.

$$\frac{\partial m_{\mathrm{xx,c}}}{\partial t} = 2D_{\mathrm{incl}} m_0, \tag{4.1}$$

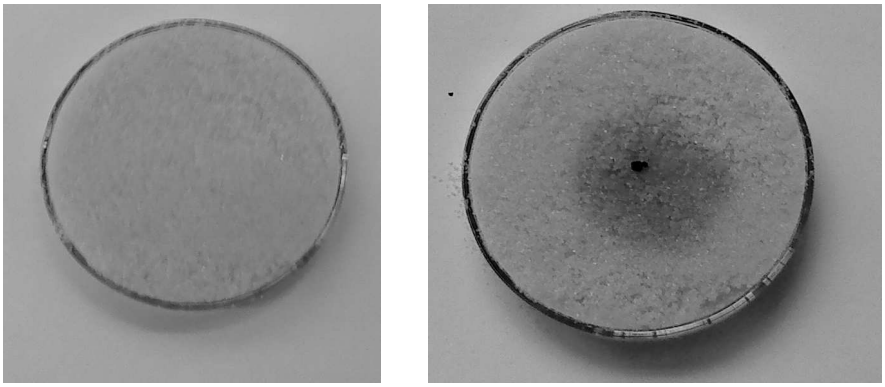

Figure 4.14 Measurement of the diffusion coefficient in the coarse glass beads at the residual saturation. Left: $t = 0$ h. Right: $t = 2.5$ h.

Using the values from Table 4.2, the typical time scales τ and T could be estimated. The estimate for the advective time scale on the large length scale was $T_{\mathrm{adv}} \approx 12000$ seconds. The advective time scale on smaller length scale τ_{adv} was estimated as $\tau_{\mathrm{adv}} \approx 1 \times 10^{26}$ seconds. Such a long time needed for advection appears due to the almost impermeable inclusions. The diffusive time scale on small length scale τ_{diff}, was estimated $\tau_{\mathrm{diff}} \approx 14000$ seconds. Time scales τ_{diff} and T_{adv} could be considered as a comparable. Therefore, one would expect in this case non-equilibrium transport in the domain as indicated in section 2.6.

Experiment: The structure created in the flume is presented in Figure 4.13. The inclusions were mostly located in the upper part of the flume since in that area coarse inclusions are almost dry and thus very impermeable. These dry inclusions created an obstacle for flow in the flume as previously explained. In the lower part of the flume one row of inclusions have been created, which were at saturated condition ($S = 1$). Those inclusions remained wet even though their entry pressure has been exceeded since water was trapped due to the same effect as explained for periodic structure in Experiment I (see section 3.1.3). The reason for creating the wet inclusions was to observe the difference between processes in inclusions dominated by advection (saturated inclusions) and diffusion (dry inclusions).

During the experiments, images were taken every 2 minutes. Several experimental images taken in Mode 1 and Mode 2 for different time steps are presented in Figure 4.15

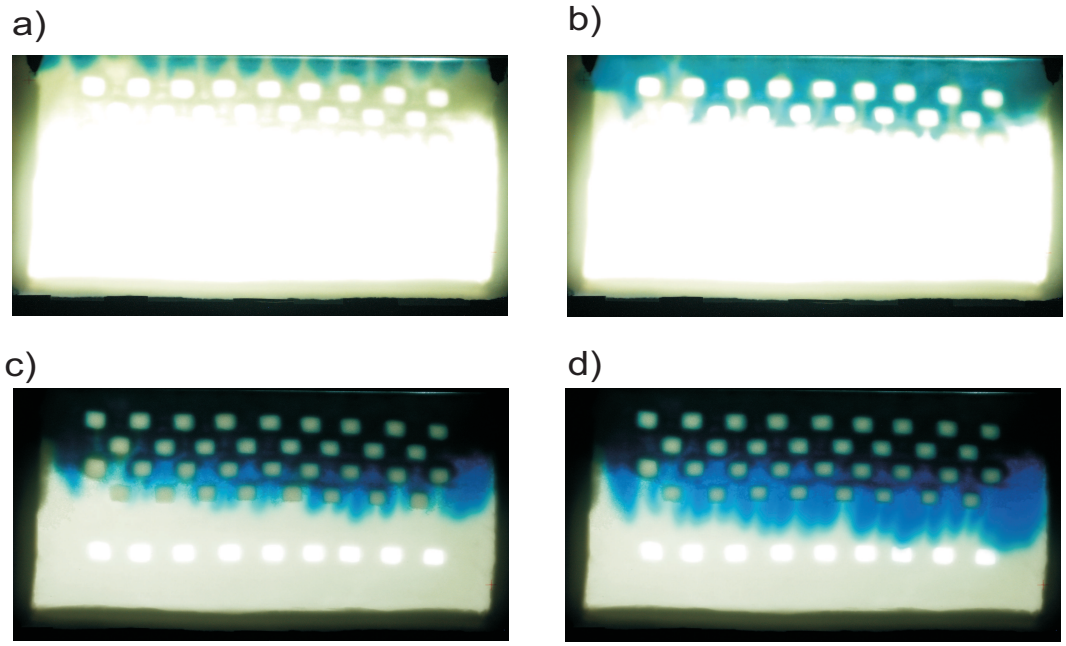

Figure 4.15 Tracer infiltration: a) $t = 14$ min and for camera Mode 1, b) $t = 48$ min and for camera Mode 1, c) $t = 108$ min and for camera Mode 2, d) $t = 154$ min and for camera Mode 2.

When the front reached the bottom of the flume, the inclusions were colored in blue due to diffusion of tracer. The concentration of tracer was higher in the boundary layer of inclusions than in their inner part. This can be seen in Figure 4.16, where images of the flume at the beginning and at the end of the tracer infiltration are compared for Mode 2. The infiltration of tracer was run until the background material in the flume was completely colored by blue tracer (tracer front reached the bottom of the flume). Afterwards, clear water has been again infiltrated from the top. Several images are presented in Figure 4.17.

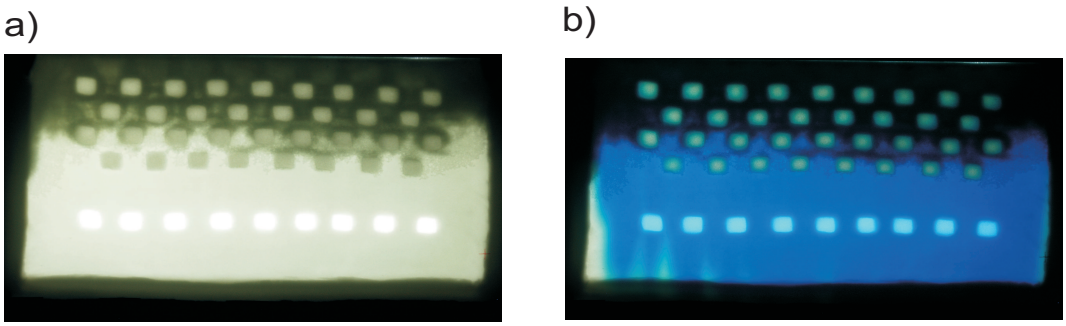

Figure 4.16 Tracer infiltration: a) $t = 0$ min and for camera Mode 2 and b) $t = 288$ min and for camera Mode 2 (end of the experiment).

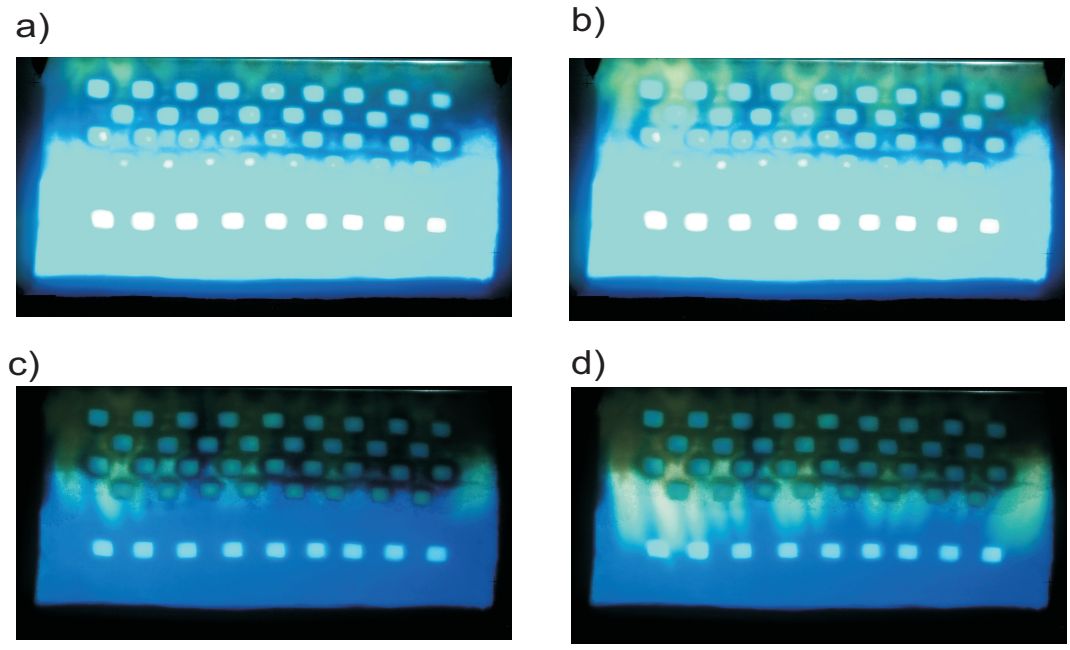

Figure 4.17 Clear water infiltration: a) $t = 14$ min and for camera Mode 1, b) $t = 48$ min and for camera Mode 1, c) $t = 108$ min and for camera Mode 2, d) $t = 154$ min and for camera Mode 2.

During the infiltration of the clear water, a tailing of the tracer was clearly observable due to the exchange with the stagnant zones in the flume. This effect is presented in Figure 4.18.

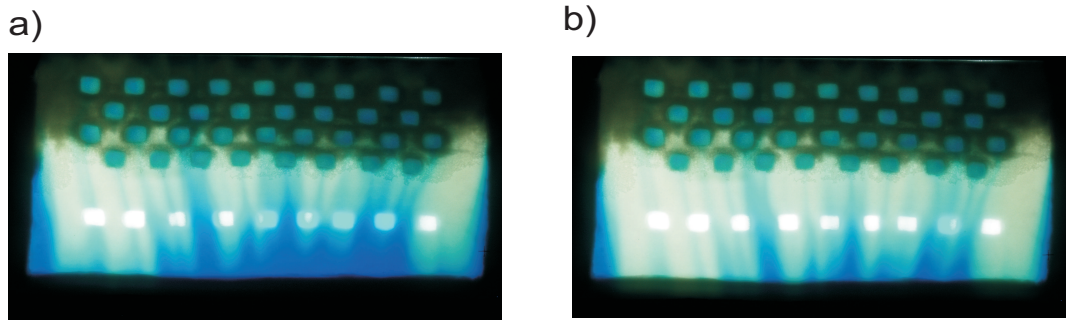

Figure 4.18 Clear water infiltration: a) $t = 342$ min and for camera Mode 2 and b) $t = 404$ min and for camera Mode 2 (end of the experiment A).

However, it was noticed that the processes in case of tracer and water injection were not equivalent. At the end of the tracer injection the inclusions were more colored in boundary area than in inner parts (higher and lower concentrations). However, during water injection it was observed that tracer has been redistributed, meaning that color in inclusion has been the same in each point

of inclusion (mean concentration in each point). Therefore, the concentration gradient between background and inclusions has been decreased in comparison to the tracer infiltration case, resulting in slower decoloring of inclusions.

4.4.2 Experiment B

Typical values and time scale analysis: During this experiment the same structure has been created in the flume as presented in Figure 4.13, but this time inclusions were created using very fine glass beads. It was expected that under the same boundary conditions as Experiment A they remain saturated and therefore conductive and advectively dominated. The typical time scales have been here also estimated. The typical values used in equation 2.35 are presented in Table 4.3.

Table 4.3 Typical values used in time scale analysis.

l (m)	**L (m)**	$\bar{\Theta}_{\text{back}}$ **(-)**	U_{back} **(m/s)**	$\bar{\Theta}_{\text{incl}}$(-)	U_{incl} **(m/s)**
0.02	0.40	0.30	1.02×10^{-5}	0.4	5.5×10^{-6}

The typical values for the background material are chosen as in the case of Experiment A (see section 4.4.1). In case of inclusion material, the typical water content $\bar{\Theta}_{\text{incl}}$ has been taken at saturated conditions. Typical velocity U_{incl} has been chosen as saturated conductivity of the inclusion material (see Table 4.1) as it has remained saturated during the experiment.

Using the values from Table 4.3, the typical time scales τ_{adv} and T_{adv} could be estimated. Final estimates for the time scales T_{adv} dominated by advection was as in the Experiment A ($T_{\text{adv}} \approx 12000$) seconds. Advective time scale on smaller length scale τ_{adv} was estimated to $\tau_{\text{adv}} \approx 1500$ seconds. The time scales τ_{adv} and T_{adv} could be assumed as not comparable. Therefore, this situation was expected to lead to equilibrium conditions as explained in section 2.6.

Experiment: After the achievement of quasi steady state in the flume with water infiltration, tracer with the same concentration of $c = 0.04$ g/l was infiltrated. Afterwards, clear water has been again infiltrated from the top. The boundary and initial conditions were the same as in the Experiment A. The goal of this experiment was to avoid stagnant zones (created due to parameter contrast) in the flume and to compare it with the Experiment A, where the influence of stagnant zones has been observed. Several images taken during tracer infiltrations at the same time as presented in Figure 4.15 are shown in Figure 4.19. It is observable that the stagnant zones are indeed avoided.

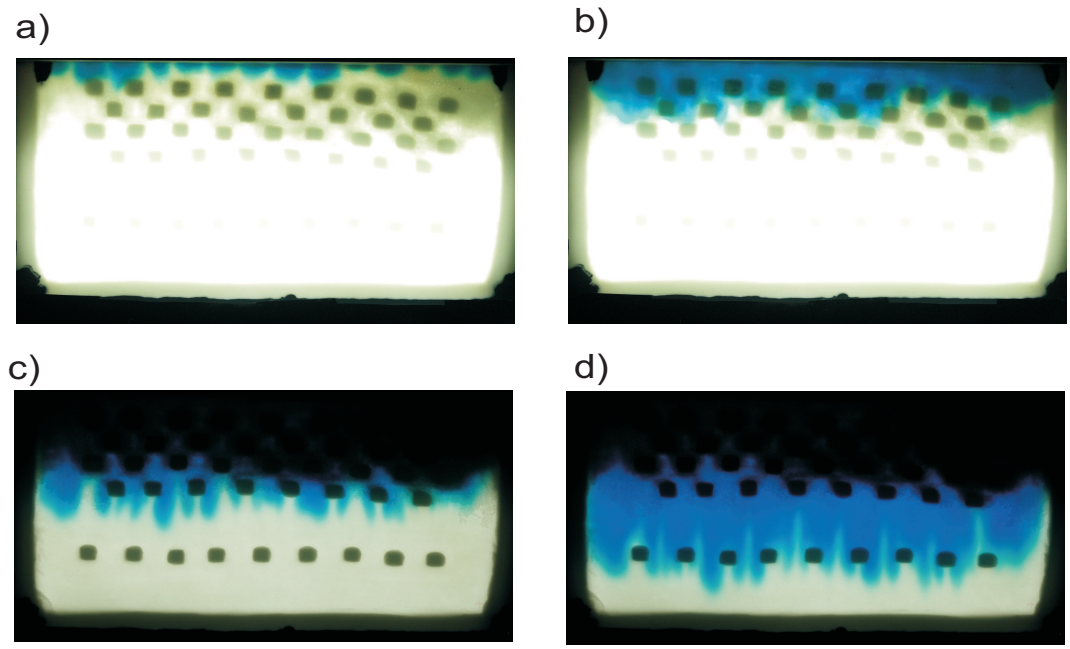

Figure 4.19 Tracer infiltration: a) $t = 14$ min and for camera Mode 1, b) $t = 48$ min and for camera Mode 1, c) $t = 108$ min and for camera Mode 2, d) $t = 154$ min and for camera Mode 2.

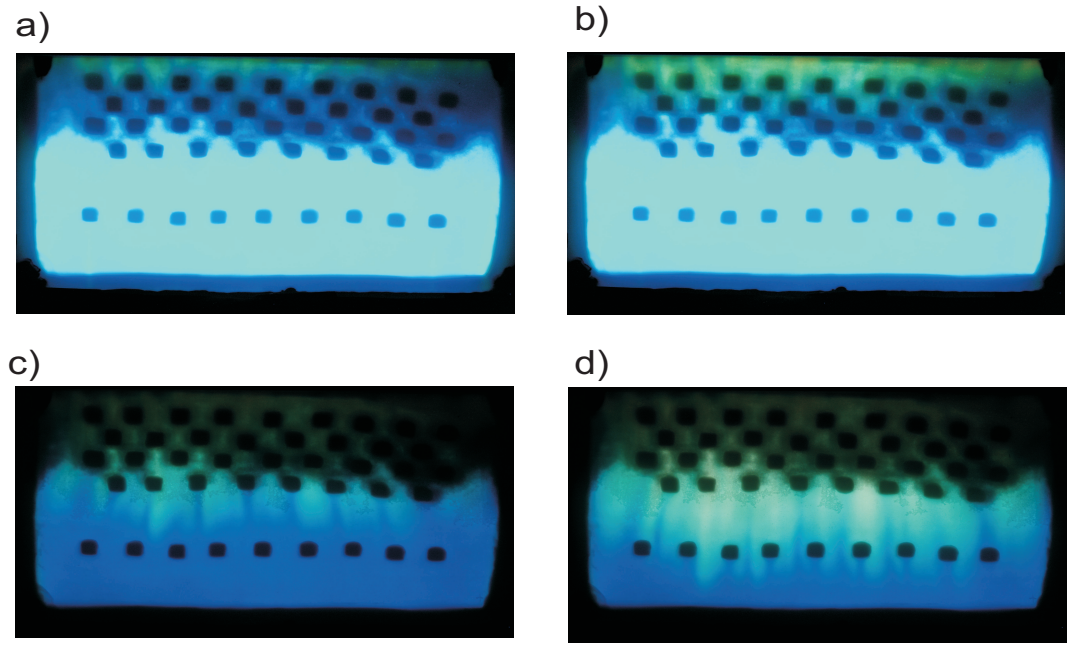

Figure 4.20 Clear water infiltration: a) $t = 14$ min and for camera Mode 1, b) $t = 48$ min and for camera Mode 1, c) $t = 108$ min and for camera Mode 2, d) $t = 154$ min and for camera Mode 2.

The images taken during clear water infiltration are presented in Figure 4.20. No tailing has been observed, during the experiment. Since there were no stagnant zones, tracer has not been trapped in inclusions.

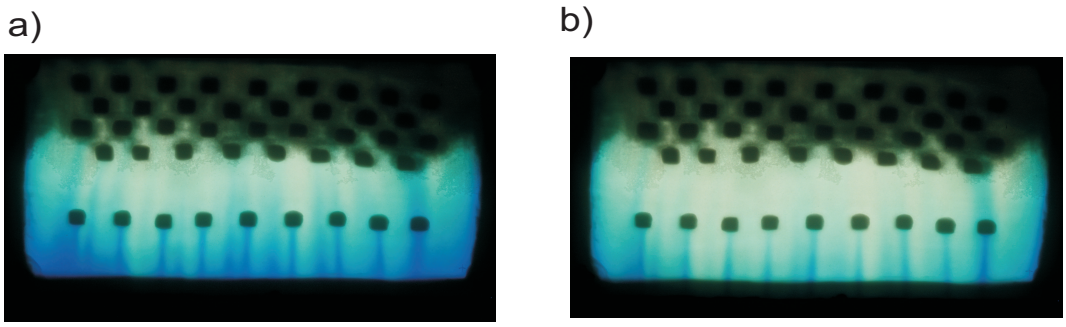

Figure 4.21 Clear water infiltration: a) $t = 342$ min and for camera Mode 2 and b) $t = 404$ min and for camera Mode 2 (end of the experiment B).

The results from the Experiment A and Experiment B are evaluated by means of comparison of breakthrough curves. In order to compare concentrations between two experiments, image analysis has been done.

4.5 Image analysis and comparison between Experiment A and Experiment B

By using the chosen calibration surfaces and values presented in Figures 4.11 and 4.12, concentrations have been calculated for all images during Experiment A and Experiment B. As an example, the resulting concentrations in case of images from Experiment A (Figures 4.15) are presented in Figure 4.22.

After calculation of the concentrations from the digital images, the concentrations at the bottom of the flume (1.5 cm) for both experiments were averaged over the width of the flume for each image and plotted over time. The resulting breakthrough curves in case of tracer infiltration during Experiments A and B are presented in Figure 4.23

It is observable from the comparison of breakthrough curves of the tracer and their slopes (Figure 4.23) that the front in Experiment A was retarded. However, it was not clear if this is due to non-uniformity of the tracer front (front on the left hand side is slightly slower during Experiment A - see Figure 4.22) since the concentrations on the bottom were averaged over the whole width of the flume. Therefore, the breakthrough curves have been analyzed by comparing separately the faster part (right hand side of the flume) and the slower part (left hand side of the flume) of the tracer front to the breakthrough curve obtained from the Experiment B. The comparison is presented in Figure 4.24, where it can be

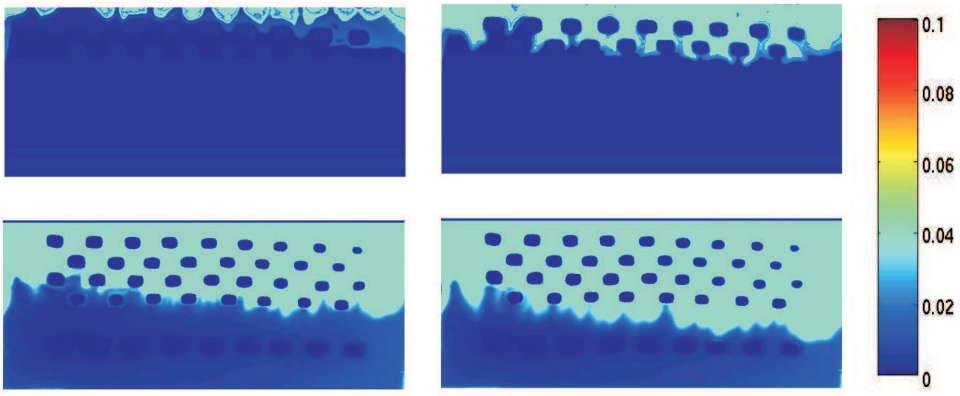

Figure 4.22 Concentration distribution in Experiment A: a) $t = 14$ and for camera Mode 1, b) $t = 48$ min and for camera Mode 1, c) $t = 108$ min and for camera Mode 2, d) $t = 154$ min and for camera Mode 2.

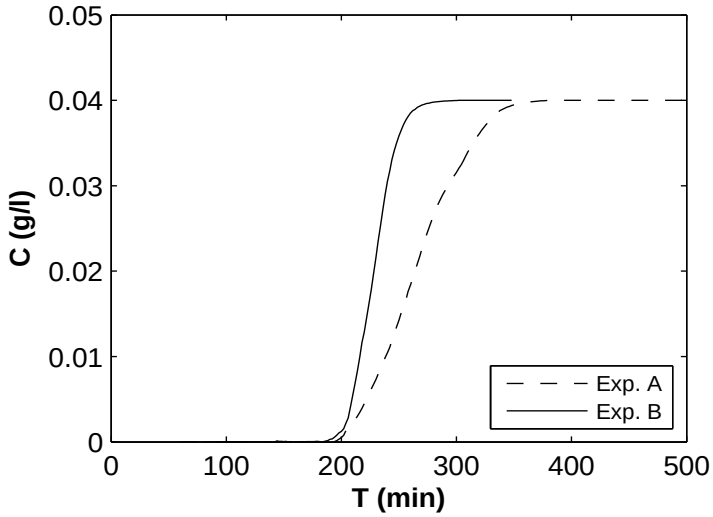

Figure 4.23 Comparison of breakthrough curves between Experiment A and Experiment B during tracer infiltration.

seen that retardation of tracer front occurred indeed. The difference between the slower and the faster tracer front part during tracer injection is given by the arriving time, but the slopes of the breakthrough curves were similar. Both of them were less steep than the slope of breakthrough curve from Experiment B.

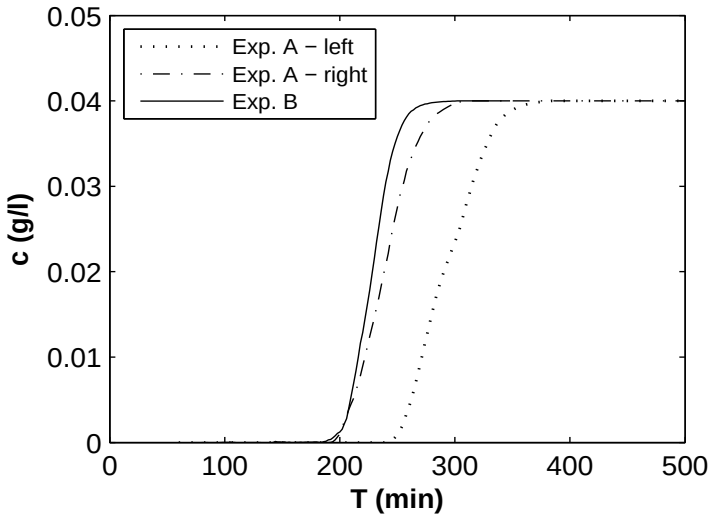

Figure 4.24 Comparison of breakthrough curves of slower and faster part of the tracer front in Experiment A with the breakthrough curve from Experiment B.

In the case of clear water infiltration, the breakthrough curves are also compared. The comparison is presented in Figure 4.25. It can be seen that stagnant zones caused long tailing below the inclusions.

4.5.1 Comparison with analytical solution

The breakthrough curves of Experiment A and Experiment B have been compared to the analytical solution for one-dimensional transport in a semi-infinite domain derived by Ogata and Banks [56] for constant concentration boundary condition (see equation 4.2):

$$c\left(x,t\right)=\frac{c_0}{2}exp\left(\frac{xv}{2D}\right)\left(exp\left(-\frac{xv}{2D}\right)erfc\left(\frac{x-vt}{4Dt}\right)+exp\left(\frac{xv}{2D}\right)erfc\left(\frac{x+vt}{4Dt}\right)\right), \tag{4.2}$$

where: D [$\mathrm{L^2\,T^{-1}}$] is the dispersion coefficient, v [$\mathrm{L\,T^{-1}}$] seepage velocity and t [T] time. The comparison of the breakthrough curves is presented in Figure 4.26. The dispersion coefficient has been fitted to the experimental results, resulting in value of $D = 7.0 \times 10^{-8}\,\mathrm{m^2/s}$.

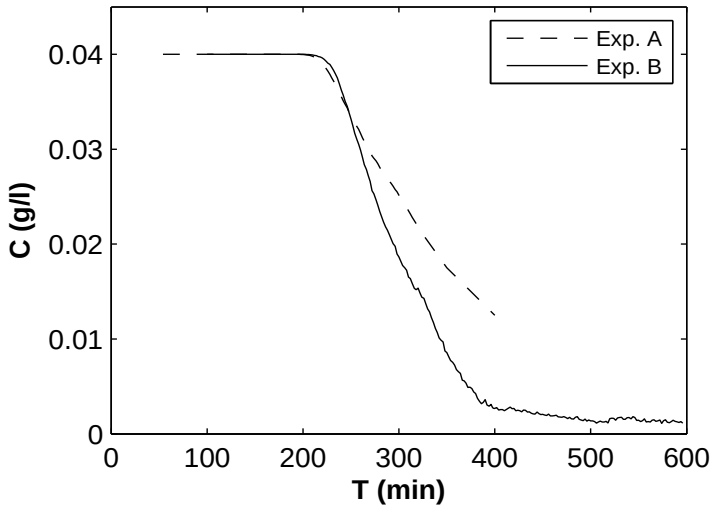

Figure 4.25 Comparison of breakthrough curves between Experiment A and Experiment B in case of water infiltration.

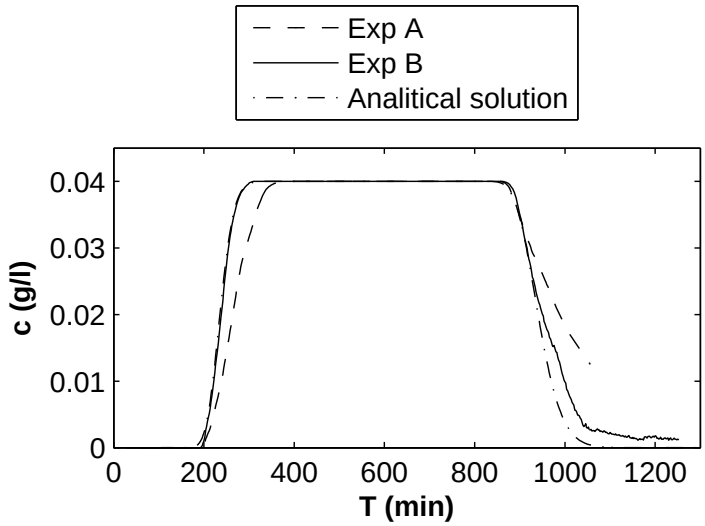

Figure 4.26 Comparison of breakthrough curves with analytical solution.

The breakthrough curve from the Experiment B (equilibrium conditions) fit very well to the analytical solution in case of tracer infiltration. However, in case of water infiltration fit is not perfect, but it is obvious from the comparison that during Experiment A both retardation and tailing of the front have occurred during the experiment.

Chapter 5

Summary and conclusions

In presented research, the intention has been made to investigate modeling of flow and transport in the unsaturated zone, when upscaled models are used. The complexity of processes occurring in this zone as well as highly heterogeneous structures, which are never known in detail are the main reasons why it is very challenging to make predictions in this zone. Instead of resolving the exact distribution of heterogeneities, which would cause enormous computational and field effort, upscaled models represent more elegant way in order to have good predictions of flow and transport.

In this study we focus on upscaled models for flow and transport in the unsaturated zone derived by means of homogenization theory. However, those derived models can not be used in general for all field cases and applications since they are derived under certain assumptions. Both upscaled models (flow and transport) used in this study are derived under assumption of domain periodicity, which is one of the main assumptions, when homogenization is used. In this case the effective parameters could be derived explicitly as the structure is known in detail. However, in nature the structure of domain is usually unknown and effective parameters have to be estimated. The derived upscaled models could be only considered as reliable and efficient when the effective parameters are estimated in an adequate and effective way, capturing the influence of heterogeneities on the smaller scale. This estimation is not straight forward task and it has to be done in such a way to include all additional information we might know about the soil structure (e.g. volume percentage of material). Additional to the periodicity and difficulty with estimation of effective parameters, the models could be derived either for equilibrium or non-equilibrium conditions, dependent from the parameter contrasts between materials (small or large). In order to be able to decide, which model (equilibrium or non-equilibrium) is more suitable for modeling of certain processes, typical time scales have to be estimated.

In this study three lab experiments have been performed in order to analyze upscaled models for flow and transport using different measurement techniques.

They were performed in order to investigate above mentioned problems (effective parameter estimation, assumption of upscaled models and time scale analysis). The experimental data have been either compared to numerical simulations or analytical solution. However, it is important to mention that the conclusions from this study can not be taken as general ones as the experiments done here have been performed in well controlled experimental conditions with artificially created heterogeneous structures. As there is still a huge gap between experimental efforts and theoretical work in field of upscaling, the aim of this work was to contribute to bridge a gap between them. Three main questions addressed in this study could be briefly summarized as:

- **Question 1:** How to characterize and quantify the influence of the soil structure on effective parameters used for upscaled models for flow in the unsaturated zone?
- **Question 2:** How applicable are the upscaled models to predict flow and transport processes in the unsaturated zone, when assumptions of upscaled models are not strictly met?
- **Question 3:** How reliable equilibrium and non-equilibrium conditions could be predicted based on the time analysis, meaning that the appropriate upscaled model could be used?

The first part of this study has been focused on flow in the unsaturated zone under equilibrium conditions. The flow upscaled model has been derived using small parameter contrast leading to equilibrium conditions in the domain. Different structures, with significantly different connectivity (periodic and random structure) have been investigated in order to gain a better knowledge of the structural influence on the estimation of effective parameters using only the information of volume percentage of used materials. It was also tried to assess applicability of mentioned upscaled flow model under ideal and non-ideal conditions, meaning that the modeled domain does not fulfil assumption of periodicity, but also of small parameter contrasts needed in case of equilibrium model.

The second part of the study has been focused on flow in the unsaturated zone under non-equilibrium. This implies that the parameter contrast between soil materials in this case was large. In order to be able to decide, which model (non-equilibrium or equilibrium) is more appropriate for modeling, typical time scales had to be estimated. Different options for estimation of typical time scales have been presented and discussed as they are decisive in order to chose, which upscaled model (equilibrium or non-equilibrium) is more appropriate to be used. The obtained time estimates have been further compared with the experimental and numerical findings.

During the third part of this research, solute transport under equilibrium and non-equilibrium has been investigated. The goal was to observe if equilibrium or

non-equilibrium of solute transport could be predicted by using time scale analysis. The estimated time scales have been compared with experimental results.

5.1 Influence of structure on estimation of effective parameters and assumptions assessment for flow under equilibrium (Questions 1 and 2)

In this research, the predictions of unsaturated flow made with upscaled models for experimental observations in heterogeneous media have been compared. For this purpose, experiments were carried out in artificially prepared sand columns. The two columns used for these experiments had the same spatial dimensions and were filled with the same volume percentages of the two sand materials. The crucial difference is that one had a regular, periodic structure and thus, a well-defined macroscopic elementary volume. Estimations of the hydraulic conductivity were based on the Maxwell approach since background material was clearly distinguished from inclusion. The other column can be considered the opposite. It had no macroscopic representative elementary volume and both coarse and fine sands had connected paths running through the entire column. In this case a self-consistent approach has been used in order to estimate the hydraulic conductivity.

During the drainage process in the periodic column, water was trapped in the inclusion material. The effective parameters have been estimated using calibrated parameters from Table 3.3. The upscaled 1D model with the estimated parameters made good predictions for the periodic column, both with respect to the steady states in the column and for the time behavior of the total outflow (see Figure 3.22). The comparison of the averaged saturations of the four horizontal layers of unit cells over time showed a good agreement (see Figure 3.25). On the left of Figure 3.25, the fourth pressure step (to -40 cm) is shown. In this case, the time behavior of the decreasing water content is predicted much too fast by the upscaled 1D model. This was to be expected due to the horizontal tangent of the effective retention curve (Figure 3.15), which was introduced to account for the trapping of water. This construction of the effective retention function can only account for the total mass of water in the column at the steady states, but not for the time behavior of the outflow as it is certainly artificial.

Although, the periodic structure was designed to fulfill the assumptions made in the upscaled model as much as possible, the criterion of separation of length scales is hardly met for the column as the ratio between the two length scales was $\varepsilon = \ell/L = 0.25$ (not much smaller compared to one). Despite of this discrepancy, the upscaled 1D model using the homogenized parameters did not deviate much

from the measurements. Furthermore, the outflow curves of the upscaled 1D model using the homogenized and estimated parameters did not significantly differ. This is an indication that the few pieces of information used in the Maxwell approach were sufficient to predict the drainage processes analyzed in the experiments.

In case of random structure, the experimental retention function and outflow curve are also compared with the prediction made with the 1D upscaled model as in the case of the periodic structure. The same upscaled 1D model was used as for the periodic structure and the predictions made with the upscaled 1D model were very good (see Figure 3.21). This statement is also true for the locally averaged water content in the column (see Figure 3.26). Since the random structure has no defined unit cell, spatial averages of the water content over the same subvolumes as for the periodic structure have been compared. Although, in the random structure, the assumption of scale separation made in the derivation of the upscaled model is clearly violated, the predictions with the upscaled 1D model were good. Apparently, for the experiments carried out here, the violated assumptions regarding the structure did not limit the applicability of the upscaled model.

The **retention behavior** of the columns was affected by their structure due to the trapping of water (periodic structure). Water was trapped in the coarse cells, as air could not reach them through the completely wet fine material. When the flow in the columns is modeled with the Richards equation, this trapping effect in the periodic column can not be captured directly. In this research, the trapping of water in the periodic column by assigning an apparent entry pressure to the coarse material (see section 3 and Figure 3.15) has been accounted. This model simplifies the accessibility for air with the horizontal line in the $h_c - S$ curve. In order to predict such apparent entry pressure effects in practical applications, the fact that coarse sand is embedded in fine sand has to be known. Without this information and the accordingly modifications, the upscaled 1D model used for the periodic structure would falsely be assumed to be applicable. An unmodified model would clearly make poor predictions (in this case it would, e.g., predict five outflow events instead of three for the periodic structure).

The main conclusions gained from the work on two columns with random and periodic structure could be summarized as:

- Even if some properties assumed in the upscaling procedure were clearly violated (as in the random column), the prediction of the averaged water content with the upscaled model was good. Here, reality turned out to be much more forgiving than one would expect.

- Inclusions of coarser material strongly affected the retention behavior of the columns. If their existence is known, this knowledge can be used to improve predictions of upscaled model parameters.

- Under the conditions investigated in this study, both estimated and homogenized parameters used in the upscaled 1D model performed well. Apparently, estimated parameters based on only rather limited information were sufficient to predict the drainage process surprisingly well. This conclusion, however, is not a general one.

- In case of drier regimes, where higher parameter contrasts occurred, the predictions did not match very well.

5.2 Time scale analysis for flow under non-equilibrium and the role of interfaces during the drainage (Question 3)

During the second part of the study, the flow in the unsaturated zone under non-equilibrium was investigated. High parameter contrast caused non-equilibrium conditions. Here a non-equilibrium configuration by the macroscopic trapping effect due to the reduced permeability of the surrounding material is analyzed with a drainage experiment (Experiment II). The outflow was measures and 3D spatial water distribution during the transient process in the sample (sand column) has been monitored by means of fast neutron tomography. In this column same sands were used as in the previous experiment (Experiment I). Prior to the experiment, which has been done in order to map above mentioned effect, based on the time analysis it was tried to estimate needed time for drainage of two sand inclusions. This is important when modeling water flow in the unsaturated zone on larger scales, where non-equilibrium models might be more appropriate then equilibrium models. The condition for the non-equilibrium models could be estimated by typical time scales for the flow.

In this work, time scales for trapping were estimated based on pre-determined parameter sets (Table 3.2) for the sands and on different approximations for the estimation of time scales. The estimated times scales in this case led to the conclusion that the water in inclusions is retarded due to the reduced permeability of the surrounding material.

The drainage of the column was done in two steps. The first step was from -12 cm to -32.5 cm and the second one from -32.5 cm to -45 cm from the bottom of the column. At the end of the first drainage step the surrounding coarse material was drained close to its residual saturation forming the barrier for drainage of the fine wet inclusions during the second step, when the entry pressure of fine material was exceeded.

It was observed in the drainage experiments that the inclusions remained wet during the whole observation time (for both pressure steps). This fitted to the time scale predictions made with the pre-determined parameter set. However,

during the second pressure step, the interfaces between the sand cubes made of fine sand showed clearly interface phenomena. The interfaces between the sand cubes in the columns drained on the time scale of an hour. In contrary, the drainage of inner part of the inclusions could not be observed for a long enough time span to conclude about the estimation of time scales due to the limited time in the PSI facility. However, it was obvious from the experiments that inclusions and interfaces have to be treated as different materials for the estimation of typical time scales for trapping.

The predicted drainage times of the upper and lower inclusions were compared to numerical simulations due to the long drainage times. The predicted and simulated drainage time scales made with the pre-determined parameters fit reasonably well (Table 3.4). It was, however, necessary to treat the interfaces as separate materials in order to capture the drainage of the column. It was also shown at the end of this part of the study that the interfaces would have to be considered in the time analysis as well, in order to predict correctly drainage times. They have slowed down the drainage of the upper inclusion due to reduced permeability creating a barrier within the upper inclusion.

The predictions made by the time analysis indicated that the crucial parameter in order to have a good prediction of drainage time scales for this system is the capacity. The conductivity of surrounding material did not vary much between end of the first and the second pressure step since before the second pressure decrease saturation was close to its residual value. Using pressure heads for capacities at the end of the second pressure step would lead to good prediction of the drainage time scales of the sample (lower/upper inclusions as well as the interfaces). The system reacted always with the fastest estimated time scale.

The main conclusions from this part of the study could be summarized as:

- High contrasts between conductivities of coarse and fine sand indeed have caused non-equilibrium as predicted by the time analysis. This has been confirmed by the drainage Experiment II, where the water in fine sand inclusions was trapped due to the reduced permeability of surrounding coarse sand.

- The capacity was the crucial parameter in order to make a good prediction in this example. The conductivity of the surrounding sand did not change significantly after the second drainage step has been applied.

- The system in this example has reacted with the fastest predicted time scale.

- Interfaces have also to be treated as a separate material and included in time analysis. They have slowed down the drainage of inclusions as dry interface barriers have been created.

5.3 Prediction of equilibrium and non-equilibrium conditions for solute transport (Question 3)

Since non-equilibrium condition caused by high parameter contrast is necessary to include when modeling flow in the unsaturated zone, a non-equilibrium conditions during solute transport in the unsaturated zone were also investigated in this study. As a criterion for non-equilibrium the time scale T for processes at the large length scale (background material) was compared to the time scale τ for processes at the small length scale dominated by the inclusions (see section 2.5.1). When those two time scales are comparable, non-equilibrium conditions can be expected.

2D experiments in a flume have been performed, where LTM has been used in order to observe saturation and solute concentrations with in the flume. The heterogeneous structure in the flume has been artificially created using fine, very fine and coarse glass beads since they are more transparent then sands.

The flume was under suction at the bottom (-26 cm) and at the top constant flow ($q = 3.0$ ml/min) has been infiltrated. After preparations and achievement of quasi steady state flow condition, tracer has been infiltrated from the top of the flume. Two experiments have been compared ("Experiment A" and "Experiment B"). In both experiments the same heterogeneous structure has been created as well as the same amount of the inclusion material has been used in order to compare the breakthrough curves. Furthermore, during both experiments, tracer with a concentration of $c = 0.04$ g/l was used. In Experiment A the inclusions were made out of coarse, whereas in Experiment B of very fine glass beads. In both cases the inclusions were less permeable than the background material. However, in Experiment A, where the inclusions were made out of coarse glass beads, the inclusions were less permeable than in Experiment B as they were drained close to residual saturation. Very fine glass beads remained saturated during whole experiment B and therefore, more permeable.

The time scale analysis carried out before the experiment predicted that during Experiment A stagnant zones will occur causing non-equilibrium conditions in investigated domain. The non-equilibrium occurred indeed. During this experiment the processes in the inclusions were dominated by diffusion. In contrary, in case of Experiment B inclusions were still saturated and the processes were dominated by advection leading to equilibrium in the system as predicted by the time scale analysis (see section 2.5.1).

The two experiments were compared by means of breakthrough curves. First, tracer fronts have been compared for the case of tracer infiltration. The results clearly indicated the retardation of the tracer front during the Experiment A. Slope of the breakthrough curve was less steep than in the case of the Experiment B. Secondly, the breakthrough curves were compared in the case of clear water infiltration. During this process, a long tailing in Experiment A has been

observed. The tracer was trapped in the inclusion and caused the tailing of the tracer.

Both cases have been compared to analytical solution. This comparison shows that solution for equilibrium case fits very well to the analytical one in case of tracer infiltration. In case of water injection the fit is not perfect, but it is obvious that both retardation and tailing of front during Experiment A (non-equilibrium) have occurred.

Additionally, it was noticed that the processes in case of tracer and water injection were not equivalent during the Experiment A. At the end of the tracer injection the inclusions were more colored in boundary area than in inner parts (higher and lower concentrations). However, during water injection it was observed that tracer has been redistributed, meaning that color within inclusion has been the same in each point of inclusion (mean concentration in each point). Therefore, the concentration gradient between background and inclusions has been decreased in comparison to the tracer infiltration case, resulting in slower decoloring of inclusions.

The main conclusions from this part of the study could be summarized as:

- The equilibrium and non-equilibrium solute transport in performed experiments could be predicted by time analysis.
- The experiment under equilibrium conditions (Experiment B) fits reasonably well to analytical solution, whereas results from experiment under non-equilibrium (Experiment A) show strong deviation from it.
- Tracer and water infiltration in the flume were not equivalent processes. The redistribution of tracer in inclusion affected the concentration gradient causing different initial conditions between two different injections.
- In case of larger domains, if the inclusions would be larger and moving front even slower, that could lead to very strong retardation and tailing effects in the subsurface. This means that in this case existing upscaled models, which assume equilibrium with in REV would give a bad predictions of solute transport as in the case of non-equilibrium during Experiment A.

Bibliography

[1] B. Ahrenholz, J. Tolke, and M. Krafczyk. Lattice-Boltzmann simulations in reconstructed parametrized porous media. *International Journal of Computational Fluid Dynamics*, 20(6):369–377, 2006.

[2] S. Attinger. Generalized coarse graining procedures in heterogeneous porous media. *Computational Geosciences*, 7(4):253–273, 2003.

[3] K. Bajracharya and D.A. Barry. Nonequilibrium solute transport parameters and their physical significance: numerical and experimental results. *Journal of Contaminated Hydrology*, 24:185–204, 1997.

[4] A. Bayer, H.J. Vogel, O. Ippisch, and K. Roth. Do effective properties for unsaturated weakly layered porous media exist? An experimental study. *Hydrology and Earth System Sciences*, 9:517–522, 2005.

[5] A. Bayer, H.J. Vogel, and K. Roth. Direct measurement of soil water retention curve using X-ray absorption. *Hydrology and Earth System Sciences*, 8:2–7, 2004.

[6] R. Brooks and A. Corey. Properties of porous media affecting fluid flow. *Journal of Irrigation and Drainage Engineering*, 92:61–88, 1966.

[7] M.L. Brusseau, R.E. Jessup, and P.S.C. Rao. Modeling the transport of solutes influenced by multiprocess non-equilibrium. *Water Resources Researc*, 25:1971–1988, 1989.

[8] D. Cioranescu and P. Donato. *An Introduction to Homogenization*. Oxford, 1999.

[9] O. Cirpka. *Environmental Fluid Mechanics II - Solute and Heat Transport in Natural Hydrosystems*. Institut of Hydraulic Engineering, Stuttgart, 2004.

[10] G. Dagan. *Flow and Transport in Porous Formations*. Springer, 1989.

[11] D.A. DiCarlo, T.W.J. Bauters, T.S. Steenhuis, J.Y. Parlange, and B.R. Bierck. High-speed measurements of three-phase flow using synchrotron X-rays. *Water Resources Research*, 33:569–576, 1997.

[12] L. J. Durlofsky. Representation of grid block hydraulic conductivity in coarse scale models of randomly heterogeneous porous media. *Water Resources Research*, 28(7):1791–1800, 1992.

[13] L. J. Durlofsky. Coarse scale models of two phase flow in heterogeneous reservoirs: volume averaged equations and their relationship to existing upscaling techniques. *Computational Geosciences*, 2:73–92, 1998.

[14] C. Feehley, C. Zheng, and F. Molz. A dual-domain mass transfer approach for modeling solute transport in heterogeneous aquifers: application to the macrodispersion experiment (made) site. *Water Resources Research*, 36:2501–2515, 2000.

[15] L.A. Ferrand, P.C.D. Milly, and G.F. Pinder. Dual-gamma attenuation for the determination of porous medium saturation with respect to three fluids. *Water Resources Research*, 22:1657–1663, 1986.

[16] C. Fesch, W. Simon, S. Haderlein, P. Reichert, and R. Schwarzenbach. Nonlinear sorption and nonequilibrium solute transport in aggregated porous media: experiments.process identification and modeling. *Journal of Contaminated Hydrology*, 31:373–407, 1998.

[17] P.A. Fokker. General anisotropic effective medium theory for the effective permeability of heterogeneous reservoirs. *Transport in Porous Media*, 44:205–218, 2001.

[18] W.R. Gardner. Calculation of capillary conductivity from pressure plate outflow data. *Soil Science Society of America Proceedings*, 20:317–320, 1956.

[19] J. Geertsma, G. Croes, and N. Schwarz. Theory of dimensionally scaled models of petroleum reservoirs. *Trans. AIME.*, 207:118, 1956.

[20] L.W. Gelhar. *Stochastic Subsurface Hydrology.* Prentice Hall, 1993.

[21] H.H. Gerke and M.T. van Genuchten. A dual-porosity model for simulating the preferential movement of water and solutes in structured porous media. *Water Resources Research*, 29(2):305–319, 1993.

[22] M.N. Goltz and P.V. Roberts. Interpreting organic solute transport data from a field experiment using physical non-equilibrium models. *Journal of Contaminated Hydrology*, 1:77–93, 1986.

[23] J.W. Griffioen, D.A. Barry, and J.Y. Parlange. Interpreting of two-region model parameters. *Water Resources Research*, 34(3):373–384, 1998.

[24] T. Harter and J.W. Hopmans. *Role of vadose zone flow processes in regional scale hydrology: Review, opportunities and challenges*. Kluwer, 2004.

[25] R. Hassanein, E. Lehmann, and P. Vontobel. Methods of scattering corrections for quantitative neutron radiography. *Nuclear Instruments and Methods in Physics Research*, A(542):353–360, 2005.

[26] S.M. Hassanizadeh, M.A. Celia, and H.K. Dahle. Dynamic effect in the capillary pressure-saturation relationship and its impact on unsaturated flow. *Vadose Zone Journal*, 1:38–57, 2002.

[27] V. Heiss, I. Neuweiler, A. Faerber, and S. Ochs. Immiscible displacement fronts in heterogeneous structures. *Water Resources Research*, page submitted, 2008.

[28] R. Helmig, H. Class, R. Huber, H. Sheta, R. Ewing, R. Hinkelmann, H. Jakobs, and P. Bastian. Architecture of the modular program system MUFTE-UG for simulating multiphase flow and transport processes in heterogeneous porous media. *Mathematische Geologie*, 2:123–131, 1998.

[29] R. Hilfer and P. E. Øren. Dimensional analysis of pore scale and field scale immiscible displacement. *Transport in Porous Media*, 22:53–72, 1996.

[30] U. Hornung. *Homogenization of miscible displacement in unsaturated aggregated soils.* In: Dynamic systems. St. Petersburg, 1991.

[31] U. Hornung. *Homogenization and Porous Media*. Springer, 1997.

[32] D. T. Hristopulos. Renormalization group methods in subsurface hydrology: overview and applications in hydraulic conductivity upscaling. *Advances in Water Resources*, 26:1279–1308, 2003.

[33] U. Jaekel, A. Georgescu, and H. Vereecken. symptotic analysis of nonlinear equilibrium solute transport in porous media. *Water Resources Research*, 32(10):3093–3098, 1996.

[34] N.J. Jarvis. The macro model (version 3.1). *Technical Description and Sample Simulations. Reports and Dissertations 19. Department of Soil Science, Swedish University of Agricultural Science, Uppsala, Sweden*, 1994.

[35] M.L. Johns and L.F. Gladden. MRI study of non-aqueous phase liquid extraction from porous media. *Magnetic Resonance Imaging*, 16(5):655–657, 1998.

[36] A.C. Kak and M. Slaney. *Principles of Computerized Tomographic Imaging*. New York:IEEE Press, 1988.

[37] P.R. King. The use of renormalization for calculating effective permeability. *Transport in Porous Media*, 4:37, 1989.

[38] P.R. King and I. Neuweiler. Probability upscaling. *Computational Geosciences*, 6:101–114, 2002.

[39] P.K. Kitanidis. *Introduction to Geostatistics*. Cambrige University Press, Cambridge, 1997.

[40] J. Kool, J.C. Parker, and M.T. van Genuchten. Determining soil hydraulic properties from one-step outflow experiments by parameter estimation I, theory and numerical studies. *Soil Science Society of America Journal*, 49:1348–1354, 1985.

[41] B.H. Kueper and D.B. McWorther. The use of macroscopic percolation theory to construct large-scale capillary pressure curves. *Water Resources Research*, 28(9):2425–2436, 1992.

[42] M. Larsson and N. Jarvis. Evaluation of a dual-porosity model to predict field-scale solute transport in a macroporous soil. *Journal of Hydrology*, 215:153–171, 1999.

[43] P. Lehmann, P. Wyss, A. Flisch, E. Lehmann, P. Vontobel, M. Krafczyk, A. Kaestner, F. Beckmann, A. Gygi, and H. Flühler. Tomographical imaging and mathematical description of porous media used for the prediction of fluid distribution. *Vadose Zone Journal*, 5(1):80–97, 2006.

[44] M. Leverett and M. True. Dimensional-model studies of oilfield behavior. *Trans. AIME.*, 146:175, 1942.

[45] Lewandowska and Laurent. Homogenization modeling and parametric study of moisture transfer in the unsaturated heterogeneous porous medium. *Transport in Porous Media*, 45:321–345, 2001.

[46] J. Lewandowska, A. Szymkiewicz, K. Burzynski, and M. Vauclin. Modeling of unsaturated water flow in double-porosity soils by the homogenization approach. *Advances in Water Resources*, 27(3):283–296, 2004.

[47] A. Bensoussan J.L. Lions and G. Papanicolaou. *Asymptotic Analysis for Periodic Structures*. North Holland, Amsterdam, 1978.

[48] B. Masschaele, M. Dierick, L. VanHoorebeeke, V. Cnudde, and P. Jacobs. The use of neutrons and monochromatic x-rays for non-destructive testing in geological materials. *Environmental Geologys*, 46:486–492, 2004.

[49] J.F. McBride and C.T. Miller. Nondestructive measurements of phase fractions in multiphase porous-media experiments by using x-ray attenuation. *Cent. Multiphase Res. News*, 1:10–13, 1994.

[50] V. McLane. Data formats and procedures for the evaluated nuclear data file. *Brookhaven National Laboratory*, pages 6–102, 2001.

[51] I. Neuweiler. *Scale Dependence of Flow and Transport Parameters in Porous Media*. Institute of Hydraulic Engineering Stuttgart, 2006.

[52] I. Neuweiler. *Upscaling methods for flow and transport problems in the subsurface*. Lecture Notes, IWS, Stuttgart, 2006.

[53] I. Neuweiler and O. Cirpka. Homogenization of the Richards equation in permeability fields with different connectivities. *Water Resources Research*, 41(2):WO2009, 2005.

[54] M.R. Niemet and J.S. Selker. A new method for quantification of liquid saturation in 2d translucent porous media systems using light transmission. *Advances in Water Resources*, 24(6):651–655, 2001.

[55] W. Nowak. *Geostatistical Methods for the Identification of Flow and Transport Parameters in the Subsurface*. PhD thesis, University of Stuttgart, Germany, 2004.

[56] A. Ogata and R.B. Banks. A solution of the differential equation of longitudinal dispersion in porous media. *US Geological Survey*, 411-A, 1962.

[57] M. Oostrom, J.H. Dane, B.C. Missildine, and R.J. Lenhard. Error analysis of dual-energy gamma radiation measurements. *Soil Science*, 160:28–42, 1995.

[58] F. Perkind and R. Collins. Scaling laws for laboratory flow models of oil reservoirs. *Trans. AIME.*, 219:69, 1960.

[59] G.E. Pickup and K.D. Stephen. An assessment of steady-state scale-up for small-scale geological models. *Petroleum Geoscience*, 6:203–210, 2000.

[60] S. Pozdniakov and C.F. Tsang. A self-consistent approach for calculating the effective hydraulic conductivity of a binary, heterogeneous medium. *Water Resources Research*, 40(5):W05105, 2004.

[61] W. Press, S. Teukolsky, B. Vetterling, and B. Flannery. *Numerical recipes in C*. Cambridge University Press, 2002.

[62] M. Quintard and S. Whitaker. Transport in chemically and mechanically heterogeneous porous media iv: large-scale mass equilibrium for solute transport with adsorption. *Advances in Water Resources*, 22:33–58, 1998.

[63] L. Rapaport. Scaling laws for use in design and operation of water-oil flow models. *Trans. AIME.*, 204:143, 1955.

[64] P. Renard and G. de Marsily. Calculating equivalent permeability: a review. *Advances in Water Resources*, 20(5-6):253–278, 1997.

[65] P. Ross and K. Smettem. A simple treatment of physical nonequilibrium water flows in soils. *Soil Science Society of America Journal*, 27(64):1926–1930, 2000.

[66] Y. Rubin. *Applied Stochastic Hydrogeology*. Oxford University Press, 2003.

[67] E. Sanchez-Palencia and A. Zaoui. *Homogenization Techniques for Composite Media*. Springer, 1987.

[68] H. Sang and S.E. Powers. Estimation unique soil hydraulic parameters for sandy media from multi-step outflow experiments. *Advances in Water Resources*, 26:445–456, 2003.

[69] B. Scanlon. Review of hydrus-1d. *Southwest Hydrology*, 3(4):37, 2004.

[70] J. Schaap, P. Lehmann, G. Frei, P. Vontobel, A. Kaestner, R. Hassanein, G. de Rooij, E. Lehmann, and H. Flühler. Measuring the effect of structure on water dynamics in heterogeneous porous media using fast neutron tomography. *submitted to Advances in Water Resources*, 2007.

[71] M.H. Schroth, S.J. Ahearn, J.S. Selker, and J.D. Istok. Characterization of miller-similar silica sands for laboratory hydrologic studies. *Soil Science Society of America Journal*, 60:1331–1339, 1996.

[72] J. Simunek, N. Jarvis, M.T. van Genuchten, , and A. Gardenas. Review and comparison of models for describing non-equilibrium and preferential flow and transport in the vadose zone. *Journal of Hydrology*, 272:14–35, 2003.

[73] P. Soille and H. Talbot. Image structure orientation using mathematical morphology. 14^{th} *International Conference on Pattern Recognition (ICPR'98)*, 2:1467, 1998.

[74] D. Stauffer. *Introduction to percolation theory*. Taylor and Francis, London, 124pp, 1985.

[75] V.C. Tidwell and R.J. Glass. X-ray and visible light transmission for laboratory measurement of two-dimensional saturation fields in thin-slab systems. *Water Resources Research*, 30:2873–2882, 1994.

[76] A.F. Toorman, P.J. Wierenga, and R.G. Hills. Parameter estimation of hydraulic properties from one-step outflow data. *Water Resources Research*, 28:3021–3028, 1992.

[77] S. Torquato. *Random Heterogeneous Materials*. Springer, New York, 2002.

[78] N. Ursino and T. Gimmi. Combined effect of heterogeneity, anisotropy and saturation on steady state flow and transport: Structure recognition and numerical simulation. *Water Resources Research*, 40:WO1415, 2004.

[79] N. Ursino, T. Gimmi, and H. Flühler. Combined effects of heterogeneity, anisotropy, and saturation on steady state flow and transport: A laboratory sand tank experiment. *Water Resources Research*, 37(2):201–208, 2001.

[80] M.T. van Genuchten. A closed-form equation for predicting the hydraulic conductivity of unsaturated soils. *Soil Science Society of America Journal*, 44:892–898, 1980.

[81] M. Vasin. *Comparison of different appraches to model transport on a very large scale with spetial regard to nitrogen in the upper Danube basin*. University of Stuttgart, Germany, 2005.

[82] M. Vasin, P. Lehmann, A. Kaestner, R. Hassanein, W. Nowak, R. Helmig, and I. Neuweiler. Drainage in heterogeneous sand columns with different geometric structures. *Advances in Water Resources*, page accepted for publication, 2008.

[83] J. V.Herwanger, C. C. Pain, A. Binley, C. R. E. de Oliveira, and M. H. Worthington. Anisotropic resistivity tomography. *Geophysical Journal International*, 158(2):409–425, 2004.

[84] N. Weisbrod, M.R. Niemet, and J.S. Selker. Light transmission technique for the evaluation of colloidal transport and dynamics in porous media. *Enviromental Science & Technology*, 37(16):3694–3700, 2003.

[85] S. Whitaker. Flow in porous media. A theoretical derivation of Darcy's law. *Transport in Porous Media*, 1:3–25, 1986.

[86] D. Wildenschild, J.W. Hopmans, M.L. Rivers, and A.J.R. Kent. Quantitative analysis of flow processes in a sand using synchrotron-based X-ray microtomography. *Vadose Zone Journal*, 4:112–126, 2005.

[87] D. Wildenschild and K.H. Jensen. Laboratory investigations of effective flow behavior in unsaturated heterogeneous sands. *Water Resources Research*, 35:17–27, 1999.

[88] R.R. Yarwood, M.L. Rockhold, M.R. Niemet, J.S. Selker, and P.J. Bottomley. Noninvasive quantitative measurement of bacterial growth in porous media under unsaturated-flow conditions. *Applied and Enviromental Microbiology*, 68(7):3597–3605, 2002.

[89] D.W. Zachmann, P.C. Duchateau, and A. Klute. The calibration of the richards flow equation for a drainage column by parameter identification. *Soil Science Society of America Journal*, 45:1012–1015, 1981.

[90] D.W. Zachmann, P.C. Duchateau, and A. Klute. Simultaneous approximation of water capacity and soil hydraulics conductivity by parameter identification. *Soil Science Society of America Journal*, 134:157–163, 1982.

[91] D. Zhang. *Stochastic Methods for Flow in Porous Media*. Academic Press, San Diego, 2002.

[92] R.W. Zimmerman. Effective conductivity of a two-dimensional medium containing elliptical inhomogeneities. *Proceedings of the royal society of London series A-mathematical physical and engineering sciences*, 1999.

[93] R.W. Zimmerman, D. Chen, and N. Cook. The effect of contact area on the permeability of fractures. *Journal of Hydrology*, 139:79–96, 1992.

[94] R.W. Zimmerman, T. Hadgu, and G. Bodvarsson. A new lumped-parameter model for flow in unsaturated dual-porosity media. *Advances in Water Resources*, 19:317–327, 1996.

Institut für Wasserbau
Universität Stuttgart

Pfaffenwaldring 61
70569 Stuttgart (Vaihingen)
Telefon (0711) 685 - 64717/64749/64752/64679
Telefax (0711) 685 - 67020 o. 64746 o. 64681
E-Mail: iws@iws.uni-stuttgart.de
http://www.iws.uni-stuttgart.de

Verzeichnis der Mitteilungshefte

5 Plate, Erich: *Beitrag zur Bestimmung der Windgeschwindigkeitsverteilung in der durch eine Wand gestörten bodennahen Luftschicht*,
und
Röhnisch, Arthur; Marotz, Günter: *Neue Baustoffe und Bauausführungen für den Schutz der Böschungen und der Sohle von Kanälen, Flüssen und Häfen; Gestehungskosten und jeweilige Vorteile*, sowie Unny, T.E.: *Schwingungsuntersuchungen am Kegelstrahlschieber*, 1967

6 Seiler, Erich: *Die Ermittlung des Anlagenwertes der bundeseigenen Binnenschiffahrtsstraßen und Talsperren und des Anteils der Binnenschiffahrt an diesem Wert*, 1967

7 *Sonderheft anläßlich des 65. Geburtstages von Prof. Arthur Röhnisch mit Beiträgen von* Benk, Dieter; Breitling, J.; Gurr, Siegfried; Haberhauer, Robert; Honekamp, Hermann; Kuz, Klaus Dieter; Marotz, Günter; Mayer-Vorfelder, Hans-Jörg; Miller, Rudolf; Plate, Erich J.; Radomski, Helge; Schwarz, Helmut; Vollmer, Ernst; Wildenhahn, Eberhard; 1967

8 Jumikis, Alfred: *Beitrag zur experimentellen Untersuchung des Wassernachschubs in einem gefrierenden Boden und die Beurteilung der Ergebnisse*, 1968

9 Marotz, Günter: *Technische Grundlagen einer Wasserspeicherung im natürlichen Untergrund*, 1968

10 Radomski, Helge: *Untersuchungen über den Einfluß der Querschnittsform wellenförmiger Spundwände auf die statischen und rammtechnischen Eigenschaften*, 1968

11 Schwarz, Helmut: *Die Grenztragfähigkeit des Baugrundes bei Einwirkung vertikal gezogener Ankerplatten als zweidimensionales Bruchproblem*, 1969

12 Erbel, Klaus: *Ein Beitrag zur Untersuchung der Metamorphose von Mittelgebirgsschneedecken unter besonderer Berücksichtigung eines Verfahrens zur Bestimmung der thermischen Schneequalität*, 1969

13 Westhaus, Karl-Heinz: *Der Strukturwandel in der Binnenschiffahrt und sein Einfluß auf den Ausbau der Binnenschiffskanäle*, 1969

14 Mayer-Vorfelder, Hans-Jörg: *Ein Beitrag zur Berechnung des Erdwiderstandes unter Ansatz der logarithmischen Spirale als Gleitflächenfunktion*, 1970

15 Schulz, Manfred: *Berechnung des räumlichen Erddruckes auf die Wandung kreiszylindrischer Körper*, 1970

16 Mobasseri, Manoutschehr: *Die Rippenstützmauer. Konstruktion und Grenzen ihrer Standsicherheit*, 1970

17 Benk, Dieter: *Ein Beitrag zum Betrieb und zur Bemessung von Hochwasserrückhaltebecken*, 1970

18 Gàl, Attila: *Bestimmung der mitschwingenden Wassermasse bei überströmten Fischbauchklappen mit kreiszylindrischem Staublech*, 1971, vergriffen

19 Kuz, Klaus Dieter: *Ein Beitrag zur Frage des Einsetzens von Kavitationserscheinungen in einer Düsenströmung bei Berücksichtigung der im Wasser gelösten Gase*, 1971, vergriffen

20 Schaak, Hartmut: *Verteilleitungen von Wasserkraftanlagen*, 1971

21 *Sonderheft zur Eröffnung der neuen Versuchsanstalt des Instituts für Wasserbau der Universität Stuttgart mit Beiträgen von* Brombach, Hansjörg; Dirksen, Wolfram; Gàl, Attila; Gerlach, Reinhard; Giesecke, Jürgen; Holthoff, Franz-Josef; Kuz, Klaus Dieter; Marotz, Günter; Minor, Hans-Erwin; Petrikat, Kurt; Röhnisch, Arthur; Rueff, Helge; Schwarz, Helmut; Vollmer, Ernst; Wildenhahn, Eberhard; 1972

22 Wang, Chung-su: *Ein Beitrag zur Berechnung der Schwingungen an Kegelstrahlschiebern*, 1972

23 Mayer-Vorfelder, Hans-Jörg: *Erdwiderstandsbeiwerte nach dem Ohde-Variationsverfahren*, 1972

24 Minor, Hans-Erwin: *Beitrag zur Bestimmung der Schwingungsanfachungsfunktionen überströmter Stauklappen*, 1972, vergriffen

25 Brombach, Hansjörg: *Untersuchung strömungsmechanischer Elemente (Fluidik) und die Möglichkeit der Anwendung von Wirbelkammerelementen im Wasserbau*, 1972, vergriffen

26 Wildenhahn, Eberhard: *Beitrag zur Berechnung von Horizontalfilterbrunnen*, 1972

27 Steinlein, Helmut: *Die Eliminierung der Schwebstoffe aus Flußwasser zum Zweck der unterirdischen Wasserspeicherung, gezeigt am Beispiel der Iller*, 1972

28 Holthoff, Franz Josef: *Die Überwindung großer Hubhöhen in der Binnenschiffahrt durch Schwimmerhebewerke*, 1973

29 Röder, Karl: *Einwirkungen aus Baugrundbewegungen auf trog- und kastenförmige Konstruktionen des Wasser- und Tunnelbaues*, 1973

30 Kretschmer, Heinz: *Die Bemessung von Bogenstaumauern in Abhängigkeit von der Talform*, 1973

31 Honekamp, Hermann: *Beitrag zur Berechnung der Montage von Unterwasserpipelines*, 1973

32 Giesecke, Jürgen: *Die Wirbelkammertriode als neuartiges Steuerorgan im Wasserbau*, und Brombach, Hansjörg: *Entwicklung, Bauformen, Wirkungsweise und Steuereigenschaften von Wirbelkammerverstärkern*, 1974

33 Rueff, Helge: *Untersuchung der schwingungserregenden Kräfte an zwei hintereinander angeordneten Tiefschützen unter besonderer Berücksichtigung von Kavitation*, 1974

34 Röhnisch, Arthur: *Einpreßversuche mit Zementmörtel für Spannbeton - Vergleich der Ergebnisse von Modellversuchen mit Ausführungen in Hüllwellrohren*, 1975

35 *Sonderheft anläßlich des 65. Geburtstages von Prof. Dr.-Ing. Kurt Petrikat mit Beiträgen von*: Brombach, Hansjörg; Erbel, Klaus; Flinspach, Dieter; Fischer jr., Richard; Gàl, Attila; Gerlach, Reinhard; Giesecke, Jürgen; Haberhauer, Robert; Hafner Edzard; Hausenblas, Bernhard; Horlacher, Hans-Burkhard; Hutarew, Andreas; Knoll, Manfred; Krummet, Ralph; Marotz, Günter; Merkle, Theodor; Miller, Christoph; Minor, Hans-Erwin; Neumayer, Hans; Rao, Syamala; Rath, Paul; Rueff, Helge; Ruppert, Jürgen; Schwarz, Wolfgang; Topal-Gökceli, Mehmet; Vollmer, Ernst; Wang, Chung-su; Weber, Hans-Georg; 1975

36 Berger, Jochum: *Beitrag zur Berechnung des Spannungszustandes in rotationssymmetrisch belasteten Kugelschalen veränderlicher Wandstärke unter Gas- und Flüssigkeitsdruck durch Integration schwach singulärer Differentialgleichungen*, 1975

37 Dirksen, Wolfram: *Berechnung instationärer Abflußvorgänge in gestauten Gerinnen mittels Differenzenverfahren und die Anwendung auf Hochwasserrückhaltebecken*, 1976

38 Horlacher, Hans-Burkhard: *Berechnung instationärer Temperatur- und Wärmespannungsfelder in langen mehrschichtigen Hohlzylindern*, 1976

39 Hafner, Edzard: *Untersuchung der hydrodynamischen Kräfte auf Baukörper im Tiefwasserbereich des Meeres*, 1977, ISBN 3-921694-39-6

40 Ruppert, Jürgen: *Über den Axialwirbelkammerverstärker für den Einsatz im Wasserbau*, 1977, ISBN 3-921694-40-X

41 Hutarew, Andreas: *Beitrag zur Beeinflußbarkeit des Sauerstoffgehalts in Fließgewässern an Abstürzen und Wehren*, 1977, ISBN 3-921694-41-8, vergriffen

42 Miller, Christoph: *Ein Beitrag zur Bestimmung der schwingungserregenden Kräfte an unterströmten Wehren*, 1977, ISBN 3-921694-42-6

43 Schwarz, Wolfgang: *Druckstoßberechnung unter Berücksichtigung der Radial- und Längsverschiebungen der Rohrwandung*, 1978, ISBN 3-921694-43-4

44 Kinzelbach, Wolfgang: *Numerische Untersuchungen über den optimalen Einsatz variabler Kühlsysteme einer Kraftwerkskette am Beispiel Oberrhein*, 1978, ISBN 3-921694-44-2

45 Barczewski, Baldur: *Neue Meßmethoden für Wasser-Luftgemische und deren Anwendung auf zweiphasige Auftriebsstrahlen*, 1979, ISBN 3-921694-45-0

46 Neumayer, Hans: *Untersuchung der Strömungsvorgänge in radialen Wirbelkammerverstärkern*, 1979, ISBN 3-921694-46-9

47 Elalfy, Youssef-Elhassan: *Untersuchung der Strömungsvorgänge in Wirbelkammerdioden und -drosseln*, 1979, ISBN 3-921694-47-7

48 Brombach, Hansjörg: *Automatisierung der Bewirtschaftung von Wasserspeichern*, 1981, ISBN 3-921694-48-5

49 Geldner, Peter: *Deterministische und stochastische Methoden zur Bestimmung der Selbstdichtung von Gewässern*, 1981, ISBN 3-921694-49-3, vergriffen

50 Mehlhorn, Hans: *Temperaturveränderungen im Grundwasser durch Brauchwassereinleitungen*, 1982, ISBN 3-921694-50-7, vergriffen

51 Hafner, Edzard: *Rohrleitungen und Behälter im Meer*, 1983, ISBN 3-921694-51-5

52 Rinnert, Bernd: *Hydrodynamische Dispersion in porösen Medien: Einfluß von Dichteunterschieden auf die Vertikalvermischung in horizontaler Strömung*, 1983, ISBN 3-921694-52-3, vergriffen

53 Lindner, Wulf: *Steuerung von Grundwasserentnahmen unter Einhaltung ökologischer Kriterien*, 1983, ISBN 3-921694-53-1, vergriffen

54 Herr, Michael; Herzer, Jörg; Kinzelbach, Wolfgang; Kobus, Helmut; Rinnert, Bernd: *Methoden zur rechnerischen Erfassung und hydraulischen Sanierung von Grundwasserkontaminationen*, 1983, ISBN 3-921694-54-X

55 Schmitt, Paul: *Wege zur Automatisierung der Niederschlagsermittlung*, 1984, ISBN 3-921694-55-8, vergriffen

56 Müller, Peter: *Transport und selektive Sedimentation von Schwebstoffen bei gestautem Abfluß*, 1985, ISBN 3-921694-56-6

57 El-Qawasmeh, Fuad: *Möglichkeiten und Grenzen der Tropfbewässerung unter besonderer Berücksichtigung der Verstopfungsanfälligkeit der Tropfelemente*, 1985, ISBN 3-921694-57-4, vergriffen

58 Kirchenbaur, Klaus: *Mikroprozessorgesteuerte Erfassung instationärer Druckfelder am Beispiel seegangsbelasteter Baukörper*, 1985, ISBN 3-921694-58-2

59 Kobus, Helmut (Hrsg.): *Modellierung des großräumigen Wärme- und Schadstofftransports im Grundwasser*, Tätigkeitsbericht 1984/85 (DFG-Forschergruppe an den Universitäten Hohenheim, Karlsruhe und Stuttgart), 1985, ISBN 3-921694-59-0, vergriffen

60 Spitz, Karlheinz: *Dispersion in porösen Medien: Einfluß von Inhomogenitäten und Dichteunterschieden*, 1985, ISBN 3-921694-60-4, vergriffen

61 Kobus, Helmut: *An Introduction to Air-Water Flows in Hydraulics*, 1985, ISBN 3-921694-61-2

62 Kaleris, Vassilios: *Erfassung des Austausches von Oberflächen- und Grundwasser in horizontalebenen Grundwassermodellen*, 1986, ISBN 3-921694-62-0

63 Herr, Michael: *Grundlagen der hydraulischen Sanierung verunreinigter Porengrundwasserleiter*, 1987, ISBN 3-921694-63-9

64 Marx, Walter: *Berechnung von Temperatur und Spannung in Massenbeton infolge Hydratation*, 1987, ISBN 3-921694-64-7

65 Koschitzky, Hans-Peter: *Dimensionierungskonzept für Sohlbelüfter in Schußrinnen zur Vermeidung von Kavitationsschäden*, 1987, ISBN 3-921694-65-5

66 Kobus, Helmut (Hrsg.): *Modellierung des großräumigen Wärme- und Schadstofftransports im Grundwasser*, Tätigkeitsbericht 1986/87 (DFG-Forschergruppe an den Universitäten Hohenheim, Karlsruhe und Stuttgart) 1987, ISBN 3-921694-66-3

67 Söll, Thomas: *Berechnungsverfahren zur Abschätzung anthropogener Temperaturanomalien im Grundwasser*, 1988, ISBN 3-921694-67-1

68 Dittrich, Andreas; Westrich, Bernd: *Bodenseeufererosion, Bestandsaufnahme und Bewertung*, 1988, ISBN 3-921694-68-X, vergriffen

69 Huwe, Bernd; van der Ploeg, Rienk R.: *Modelle zur Simulation des Stickstoffhaushaltes von Standorten mit unterschiedlicher landwirtschaftlicher Nutzung*, 1988, ISBN 3-921694-69-8, vergriffen

70 Stephan, Karl: *Integration elliptischer Funktionen*, 1988, ISBN 3-921694-70-1

71 Kobus, Helmut; Zilliox, Lothaire (Hrsg.): *Nitratbelastung des Grundwassers, Auswirkungen der Landwirtschaft auf die Grundwasser- und Rohwasserbeschaffenheit und Maßnahmen zum Schutz des Grundwassers*. Vorträge des deutsch-französischen Kolloquiums am 6. Oktober 1988, Universitäten Stuttgart und Louis Pasteur Strasbourg (Vorträge in deutsch oder französisch, Kurzfassungen zweisprachig), 1988, ISBN 3-921694-71-X

72 Soyeaux, Renald: *Unterströmung von Stauanlagen auf klüftigem Untergrund unter Berücksichtigung laminarer und turbulenter Fließzustände*,1991, ISBN 3-921694-72-8

73 Kohane, Roberto: *Berechnungsmethoden für Hochwasserabfluß in Fließgewässern mit überströmten Vorländern*, 1991, ISBN 3-921694-73-6

74 Hassinger, Reinhard: *Beitrag zur Hydraulik und Bemessung von Blocksteinrampen in flexibler Bauweise*, 1991, ISBN 3-921694-74-4, vergriffen

75 Schäfer, Gerhard: *Einfluß von Schichtenstrukturen und lokalen Einlagerungen auf die Längsdispersion in Porengrundwasserleitern*, 1991, ISBN 3-921694-75-2

76 Giesecke, Jürgen: *Vorträge, Wasserwirtschaft in stark besiedelten Regionen; Umweltforschung mit Schwerpunkt Wasserwirtschaft*, 1991, ISBN 3-921694-76-0

77 Huwe, Bernd: *Deterministische und stochastische Ansätze zur Modellierung des Stickstoffhaushalts landwirtschaftlich genutzter Flächen auf unterschiedlichem Skalenniveau*, 1992, ISBN 3-921694-77-9, vergriffen

78 Rommel, Michael: *Verwendung von Kluftdaten zur realitätsnahen Generierung von Kluftnetzen mit anschließender laminar-turbulenter Strömungsberechnung*, 1993, ISBN 3-92 1694-78-7

79 Marschall, Paul: *Die Ermittlung lokaler Stofffrachten im Grundwasser mit Hilfe von Einbohrloch-Meßverfahren*, 1993, ISBN 3-921694-79-5, vergriffen

80 Ptak, Thomas: *Stofftransport in heterogenen Porenaquiferen: Felduntersuchungen und stochastische Modellierung*, 1993, ISBN 3-921694-80-9, vergriffen

81 Haakh, Frieder: *Transientes Strömungsverhalten in Wirbelkammern,* 1993, ISBN 3-921694-81-7

82 Kobus, Helmut; Cirpka, Olaf; Barczewski, Baldur; Koschitzky, Hans-Peter: *Versucheinrichtung zur Grundwasser und Altlastensanierung VEGAS, Konzeption und Programmrahmen*, 1993, ISBN 3-921694-82-5

83 Zang, Weidong: *Optimaler Echtzeit-Betrieb eines Speichers mit aktueller Abflußregenerierung*, 1994, ISBN 3-921694-83-3, vergriffen

84 Franke, Hans-Jörg: *Stochastische Modellierung eines flächenhaften Stoffeintrages und Transports in Grundwasser am Beispiel der Pflanzenschutzmittelproblematik*, 1995, ISBN 3-921694-84-1

85 Lang, Ulrich: *Simulation regionaler Strömungs- und Transportvorgänge in Karstaquiferen mit Hilfe des Doppelkontinuum-Ansatzes: Methodenentwicklung und Parameteridentifikation*, 1995, ISBN 3-921694-85-X, vergriffen

86 Helmig, Rainer: *Einführung in die Numerischen Methoden der Hydromechanik*, 1996, ISBN 3-921694-86-8, vergriffen

87 Cirpka, Olaf: *CONTRACT: A Numerical Tool for Contaminant Transport and Chemical Transformations - Theory and Program Documentation* -, 1996, ISBN 3-921694-87-6

88 Haberlandt, Uwe: *Stochastische Synthese und Regionalisierung des Niederschlages für Schmutzfrachtberechnungen*, 1996, ISBN 3-921694-88-4

89 Croisé, Jean: *Extraktion von flüchtigen Chemikalien aus natürlichen Lockergesteinen mittels erzwungener Luftströmung*, 1996, ISBN 3-921694-89-2, vergriffen

90 Jorde, Klaus: *Ökologisch begründete, dynamische Mindestwasserregelungen bei Ausleitungskraftwerken*, 1997, ISBN 3-921694-90-6, vergriffen

91 Helmig, Rainer: *Gekoppelte Strömungs- und Transportprozesse im Untergrund - Ein Beitrag zur Hydrosystemmodellierung*-, 1998, ISBN 3-921694-91-4, vergriffen

92 Emmert, Martin: *Numerische Modellierung nichtisothermer Gas-Wasser Systeme in porösen Medien,* 1997, ISBN 3-921694-92-2

93 Kern, Ulrich: *Transport von Schweb- und Schadstoffen in staugeregelten Fließgewässern am Beispiel des Neckars*, 1997, ISBN 3-921694-93-0, vergriffen

94 Förster, Georg: *Druckstoßdämpfung durch große Luftblasen in Hochpunkten von Rohrleitungen 1997*, ISBN 3-921694-94-9

95 Cirpka, Olaf: *Numerische Methoden zur Simulation des reaktiven Mehrkomponententransports im Grundwasser*, 1997, ISBN 3-921694-95-7, vergriffen

96 Färber, Arne: *Wärmetransport in der ungesättigten Bodenzone: Entwicklung einer thermischen In-situ-Sanierungstechnologie*, 1997, ISBN 3-921694-96-5

97 Betz, Christoph: *Wasserdampfdestillation von Schadstoffen im porösen Medium: Entwicklung einer thermischen In-situ-Sanierungstechnologie*, 1998, ISBN 3-921694-97-3

98 Xu, Yichun: *Numerical Modeling of Suspended Sediment Transport in Rivers*, 1998, ISBN 3-921694-98-1, vergriffen

99 Wüst, Wolfgang: *Geochemische Untersuchungen zur Sanierung CKW-kontaminierter Aquifere mit Fe(0)-Reaktionswänden,* 2000, ISBN 3-933761-02-2

100 Sheta, Hussam: *Simulation von Mehrphasenvorgängen in porösen Medien unter Einbeziehung von Hysterese-Effekten*, 2000, ISBN 3-933761-03-4

101 Ayros, Edwin: *Regionalisierung extremer Abflüsse auf der Grundlage statistischer Verfahren*, 2000, ISBN 3-933761-04-2, vergriffen

102 Huber, Ralf: *Compositional Multiphase Flow and Transport in Heterogeneous Porous Media*, 2000, ISBN 3-933761-05-0

103 Braun, Christopherus: *Ein Upscaling-Verfahren für Mehrphasenströmungen in porösen Medien*, 2000, ISBN 3-933761-06-9

104 Hofmann, Bernd: *Entwicklung eines rechnergestützten Managementsystems zur Beurteilung von Grundwasserschadensfällen*, 2000, ISBN 3-933761-07-7

105 Class, Holger: *Theorie und numerische Modellierung nichtisothermer Mehrphasenprozesse in NAPL-kontaminierten porösen Medien,* 2001, ISBN 3-933761-08-5

106 Schmidt, Reinhard: *Wasserdampf- und Heißluftinjektion zur thermischen Sanierung kontaminierter Standorte*, 2001, ISBN 3-933761-09-3

107 Josef, Reinhold:, *Schadstoffextraktion mit hydraulischen Sanierungsverfahren unter Anwendung von grenzflächenaktiven Stoffen*, 2001, ISBN 3-933761-10-7

108 Schneider, Matthias: *Habitat- und Abflussmodellierung für Fließgewässer mit unscharfen Berechnungsansätzen*, 2001, ISBN 3-933761-11-5

109 Rathgeb, Andreas: *Hydrodynamische Bemessungsgrundlagen für Lockerdeckwerke an überströmbaren Erddämmen*, 2001, ISBN 3-933761-12-3

110 Lang, Stefan: *Parallele numerische Simulation instätionärer Probleme mit adaptiven Methoden auf unstrukturierten Gittern*, 2001, ISBN 3-933761-13-1

111 Appt, Jochen; Stumpp Simone: *Die Bodensee-Messkampagne 2001, IWS/CWR Lake Constance Measurement Program 2001*, 2002, ISBN 3-933761-14-X

112 Heimerl, Stephan: *Systematische Beurteilung von Wasserkraftprojekten,* 2002, ISBN 3-933761-15-8

113 Iqbal, Amin: *On the Management and Salinity Control of Drip Irrigation,* 2002, ISBN 3-933761-16-6

114 Silberhorn-Hemminger, Annette: *Modellierung von Kluftaquifersystemen: Geostatistische Analyse und deterministisch-stochastische Kluftgenerierung,* 2002, ISBN 3-933761-17-4

115 Winkler, Angela: *Prozesse des Wärme- und Stofftransports bei der In-situ-Sanierung mit festen Wärmequellen,* 2003, ISBN 3-933761-18-2

116 Marx, Walter: *Wasserkraft, Bewässerung, Umwelt - Planungs- und Bewertungsschwerpunkte der Wasserbewirtschaftung,* 2003, ISBN 3-933761-19-0

117 Hinkelmann, Reinhard: *Efficient Numerical Methods and Information-Processing Techniques in Environment Water,* 2003, ISBN 3-933761-20-4

118 Samaniego-Eguiguren, Luis Eduardo: *Hydrological Consequences of Land Use / Land Cover and Climatic Changes in Mesoscale Catchments*, 2003, ISBN 3-933761-21-2

119 Neunhäuserer, Lina: *Diskretisierungsansätze zur Modellierung von Strömungs- und Transportprozessen in geklüftet-porösen Medien*, 2003, ISBN 3-933761-22-0

120 Paul, Maren: *Simulation of Two-Phase Flow in Heterogeneous Poros Media with Adaptive Methods*, 2003, ISBN 3-933761-23-9

121 Ehret, Uwe: *Rainfall and Flood Nowcasting in Small Catchments using Weather Radar*, 2003, ISBN 3-933761-24-7

122 Haag, Ingo: *Der Sauerstoffhaushalt staugeregelter Flüsse am Beispiel des Neckars - Analysen, Experimente, Simulationen -,* 2003, ISBN 3-933761-25-5

123 Appt, Jochen: *Analysis of Basin-Scale Internal Waves in Upper Lake Constance,* 2003, ISBN 3-933761-26-3

124 Hrsg.: Schrenk, Volker; Batereau, Katrin; Barczewski, Baldur; Weber, Karolin und Koschitzky, Hans-Peter: *Symposium Ressource Fläche und VEGAS - Statuskolloquium 2003, 30. September und 1. Oktober 2003,* 2003, ISBN 3-933761-27-1

125 Omar Khalil Ouda: *Optimisation of Agricultural Water Use: A Decision Support System for the Gaza Strip,* 2003, ISBN 3-933761-28-0

126 Batereau, Katrin: *Sensorbasierte Bodenluftmessung zur Vor-Ort-Erkundung von Schadensherden im Untergrund*, 2004, ISBN 3-933761-29-8

127 Witt, Oliver: *Erosionsstabilität von Gewässersedimenten mit Auswirkung auf den Stofftransport bei Hochwasser am Beispiel ausgewählter Stauhaltungen des Oberrheins*, 2004, ISBN 3-933761-30-1

128 Jakobs, Hartmut: *Simulation nicht-isothermer Gas-Wasser-Prozesse in komplexen Kluft-Matrix-Systemen*, 2004, ISBN 3-933761-31-X

129 Li, Chen-Chien: *Deterministisch-stochastisches Berechnungskonzept zur Beurteilung der Auswirkungen erosiver Hochwasserereignisse in Flussstauhaltungen,* 2004, ISBN 3-933761-32-8

130 Reichenberger, Volker; Helmig, Rainer; Jakobs, Hartmut; Bastian, Peter; Niessner, Jennifer: *Complex Gas-Water Processes in Discrete Fracture-Matrix Systems: Upscaling, Mass-Conservative Discretization and Efficient Multilevel Solution,* 2004, ISBN 3-933761-33-6

131 Hrsg.: Barczewski, Baldur; Koschitzky, Hans-Peter; Weber, Karolin; Wege, Ralf: *VEGAS - Statuskolloquium 2004,* Tagungsband zur Veranstaltung am 05. Oktober 2004 an der Universität Stuttgart, Campus Stuttgart-Vaihingen, 2004, ISBN 3-933761-34-4

132 Asie, Kemal Jabir: *Finite Volume Models for Multiphase Multicomponent Flow through Porous Media*. 2005, ISBN 3-933761-35-2

133 Jacoub, George: *Development of a 2-D Numerical Module for Particulate Contaminant Transport in Flood Retention Reservoirs and Impounded Rivers,* 2004, ISBN 3-933761-36-0

134 Nowak, Wolfgang: *Geostatistical Methods for the Identification of Flow and Transport Parameters in the Subsurface,* 2005, ISBN 3-933761-37-9

135 Süß, Mia: *Analysis of the influence of structures and boundaries on flow and transport processes in fractured porous media*, 2005, ISBN 3-933761-38-7

136 Jose, Surabhin Chackiath: *Experimental Investigations on Longitudinal Dispersive Mixing in Heterogeneous Aquifers,* 2005, ISBN: 3-933761-39-5

137 Filiz, Fulya: *Linking Large-Scale Meteorological Conditions to Floods in Mesoscale Catchments,* 2005, ISBN 3-933761-40-9

138 Qin, Minghao: *Wirklichkeitsnahe und recheneffiziente Ermittlung von Temperatur und Spannungen bei großen RCC-Staumauern*, 2005, ISBN 3-933761-41-7

139 Kobayashi, Kenichiro: *Optimization Methods for Multiphase Systems in the Subsurface - Application to Methane Migration in Coal Mining Areas*, 2005, ISBN 3-933761-42-5

140 Rahman, Md. Arifur: *Experimental Investigations on Transverse Dispersive Mixing in Heterogeneous Porous Media,* 2005, ISBN 3-933761-43-3

141 Schrenk, Volker: *Ökobilanzen zur Bewertung von Altlastensanierungsmaßnahmen,* 2005, ISBN 3-933761-44-1

142 Hundecha, Hirpa Yeshewatesfa: *Regionalization of Parameters of a Conceptual Rainfall-Runoff Model*, 2005, ISBN: 3-933761-45-X

143 Wege, Ralf: *Untersuchungs- und Überwachungsmethoden für die Beurteilung natürlicher Selbstreinigungsprozesse im Grundwasser,* 2005, ISBN 3-933761-46-8

144 Breiting, Thomas: *Techniken und Methoden der Hydroinformatik - Modellierung von komplexen Hydrosystemen im Untergrund*, 2006, 3-933761-47-6

145 Hrsg.: Braun, Jürgen; Koschitzky, Hans-Peter; Müller, Martin: *Ressource Untergrund: 10 Jahre VEGAS: Forschung und Technologieentwicklung zum Schutz von Grundwasser und Boden,* Tagungsband zur Veranstaltung am 28. und 29. September 2005 an der Universität Stuttgart, Campus Stuttgart-Vaihingen, 2005, ISBN 3-933761-48-4

146 Rojanschi, Vlad: *Abflusskonzentration in mesoskaligen Einzugsgebieten unter Berücksichtigung des Sickerraumes,* 2006, ISBN 3-933761-49-2

147 Winkler, Nina Simone: *Optimierung der Steuerung von Hochwasserrückhaltebecken-systemen,* 2006, ISBN 3-933761-50-6

148 Wolf, Jens: *Räumlich differenzierte Modellierung der Grundwasserströmung alluvialer Aquifere für mesoskalige Einzugsgebiete*, 2006, ISBN: 3-933761-51-4

149 Kohler, Beate: *Externe Effekte der Laufwasserkraftnutzung*, 2006, ISBN 3-933761-52-2

150 Hrsg.: Braun, Jürgen; Koschitzky, Hans-Peter; Stuhrmann, Matthias: *VEGAS-Statuskolloquium 2006,* Tagungsband zur Veranstaltung am 28. September 2006 an der Universität Stuttgart, Campus Stuttgart-Vaihingen, 2006, ISBN 3-933761-53-0

151 Niessner, Jennifer: *Multi-Scale Modeling of Multi-Phase - Multi-Component Processes in Heterogeneous Porous Media*, 2006, ISBN 3-933761-54-9

152 Fischer, Markus: *Beanspruchung eingeerdeter Rohrleitungen infolge Austrocknung bindiger Böden,* 2006, ISBN 3-933761-55-7

153 Schneck, Alexander: *Optimierung der Grundwasserbewirtschaftung unter Berücksichtigung der Belange der Wasserversorgung, der Landwirtschaft und des Naturschutzes*, 2006, ISBN 3-933761-56-5

154 Das, Tapash: *The Impact of Spatial Variability of Precipitation on the Predictive Uncertainty of Hydrological Models,* 2006, ISBN 3-933761-57-3

155 Bielinski, Andreas: *Numerical Simulation of CO_2 sequestration in geological formations*, 2007, ISBN 3-933761-58-1

156 Mödinger, Jens: *Entwicklung eines Bewertungs- und Entscheidungsunterstützungssystems für eine nachhaltige regionale Grundwasserbewirtschaftung*, 2006, ISBN 3-933761-60-3

157 Manthey, Sabine: *Two-phase flow processes with dynamic effects in porous media - parameter estimation and simulation,* 2007, ISBN 3-933761-61-1

158 Pozos Estrada, Oscar: *Investigation on the Effects of Entrained Air in Pipelines,* 2007, ISBN 3-933761-62-X

159 Ochs, Steffen Oliver: *Steam injection into saturated porous media – process analysis including experimental and numerical investigations*, 2007, ISBN 3-933761-63-8

160 Marx, Andreas: *Einsatz gekoppelter Modelle und Wetterradar zur Abschätzung von Niederschlagsintensitäten und zur Abflussvorhersage, 2007,* ISBN 3-933761-64-6

161 Hartmann, Gabriele Maria: *Investigation of Evapotranspiration Concepts in Hydrological Modelling for Climate Change Impact Assessment*, 2007, ISBN 3-933761-65-4

162 Kebede Gurmessa, Tesfaye: *Numerical Investigation on Flow and Transport Characteristics to Improve Long-Term Simulation of Reservoir Sedimentation*, 2007, ISBN 3-933761-66-2

163 Trifković, Aleksandar: *Multi-objective and Risk-based Modelling Methodology for Planning, Design and Operation of Water Supply Systems*, 2007, ISBN 3-933761-67-0

164 Götzinger, Jens: *Distributed Conceptual Hydrological Modelling - Simulation of Climate, Land Use Change Impact and Uncertainty Analysis*, 2007, ISBN 3-933761-68-9

165 Hrsg.: Braun, Jürgen; Koschitzky, Hans-Peter; Stuhrmann, Matthias: *VEGAS – Kolloquium 2007,* Tagungsband zur Veranstaltung am 26. September 2007 an der Universität Stuttgart, Campus Stuttgart-Vaihingen, 2007, ISBN 3-933761-69-7

166 Freeman, Beau: *Modernization Criteria Assessment for Water Resources Planning; Klamath Irrigation Project, U.S.*, 2008, ISBN 3-933761-70-0

167 Dreher, Thomas: *Selektive Sedimentation von Feinstschwebstoffen in Wechselwirkung mit wandnahen turbulenten Strömungsbedingungen*, 2008, ISBN 3-933761-71-9

168 Yang, Wei: *Discrete-Continuous Downscaling Model for Generating Daily Precipitation Time Series*, 2008, ISBN 3-933761-72-7

169 Kopecki, Ianina: *Calculational Approach to FST-Hemispheres for Multiparametrical Benthos Habitat Modelling,* 2008*,* ISBN 3-933761-73-5

170 Brommundt, Jürgen: *Stochastische Generierung räumlich zusammenhängender Niederschlagszeitreihen*, 2008, ISBN 3-933761-74-3

171 Papafotiou, *Alexandros: Numerical Investigations of the Role of Hysteresis in Heterogeneous Two-Phase Flow Systems*, 2008, ISBN 3-933761-75-1

172 He, Yi: *Application of a Non-Parametric Classification Scheme to Catchment Hydrology*, 2008, ISBN 978-3-933761-76-7

173 Wagner, Sven: *Water Balance in a Poorly Gauged Basin in West Africa Using Atmospheric Modelling and Remote Sensing Information*, 2008, ISBN 978-3-933761-77-4

174 Hrsg.: Braun, Jürgen; Koschitzky, Hans-Peter; Stuhrmann, Matthias; Schrenk, Volker: *VEGAS-Kolloquium 2008 Ressource Fläche III*, Tagungsband zur Veranstaltung am 01. Oktober 2008 an der Universität Stuttgart, Campus Stuttgart-Vaihingen, 2008, ISBN 978-3-933761-78-1

175 Patil, Sachin: *Regionalization of an Event Based Nash Cascade Model for Flood Predictions in Ungauged Basins*, 2008, ISBN 978-3-933761-79-8

176 Assteerawatt, Anongnart: *Flow and Transport Modelling of Fractured Aquifers based on a Geostatistical Approach,* 2008, ISBN 978-3-933761-80-4

177 Karnahl, Joachim Alexander: *2D numerische Modellierung von multifraktionalem Schwebstoff- und Schadstofftransport in Flüssen*, 2008, ISBN 978-3-933761-81-1

178 Hiester, Uwe: *Technologieentwicklung zur In-situ-Sanierung der ungesättigten Bodenzone mit festen Wärmequellen,* 2009, ISBN 978-3-933761-82-8

179 Laux, Patrick: *Statistical Modeling of Precipitation for Agricultural Planning in the Volta Basin of West Africa,* 2009, ISBN 978-3-933761-83-5

180 Ehsan, Saqib: *Evaluation of Life Safety Risks Related to Severe Flooding,* 2009, ISBN 978-3-933761-84-2

181 Prohaska, Sandra: *Development and Application of a 1D Multi-Strip Fine Sediment Transport Model for Regulated Rivers,* 2009, ISBN 978-3-933761-85-9

182 Kopp, Andreas: *Evaluation of CO_2 Injection Processes in Geological Formations for Site Screening,* 2009, ISBN 978-3-933761-86-6

183 Ebigbo, Anozie: *Modelling of biofilm growth and its influence on CO_2 and water (two-phase) flow in porous media,* 2009, ISBN 978-3-933761-87-3

184 Freiboth, Sandra: *A phenomenological model for the numerical simulation of multiphase multicomponent processes considering structural alterations of porous media*, 2009, ISBN 978-3-933761-88-0

185 Zöllner, Frank: *Implementierung und Anwendung netzfreier Methoden im Konstruktiven Wasserbau und in der Hydromechanik*, 2009, ISBN 978-3-933761-89-7

186 Vasin, Milos: *Influence of the soil structure and property contrast on flow and transport in the unsaturated zone*, 2010, ISBN 978-3-933761-90-3

Die Mitteilungshefte ab der Nr. 134 (Jg. 2005) stehen als pdf-Datei über die Homepage des Instituts: www.iws.uni-stuttgart.de zur Verfügung.